Addendum to the

Progress Report and Renewal Request for R&D on

Central and Forward Tracking

W.S. Anderson (graduate student), J.C. Armitage,[1] P. Chevreau (undergraduate student), J.G. Heinrich, C. Lu, I. McDonald (graduate student), K.T. McDonald,[2] B. Miller (graduate student), D. Secrest (graduate student), and J. Weckel (graduate student)

Joseph Henry Laboratories, Princeton University, Princeton, NJ 08544

(September 4, 1990)

Abstract

We present a detailed summary of work accomplished at Princeton U. in FY90 towards a straw-tube tracking subsystem with precision spatial resolution at the SSC.

[1] on sabbatical from Carleton U.

[2] Contactperson

Contents

List of Figures

List of Tables

1 Introduction

The physics motivation for our work on straw-tube tracking has been described in the Bottom Collider Detector Expression of Interest (EOI0008, May 25, 1990). Preliminary reports of our work have been presented at the Workshop on Major SSC Detectors (Tucson, Feb. 19-23, 1990),[1] at the IISSC Industrial Symposium (Miami, Mar. 14-16, 1990),[2] and at the International Conference on Advanced Technology and Particle Physics (Como, Italy, June 11-15, 1990).[3]

Work accomplished in FY90:

1. Purchase of 3000 sets of Ultem feedthroughs, brass taper pins, and aluminum collars for 7-mm-diameter straws, according to designs from an Ohio State U. group.[4]

2. Winding of 4 sets of straw tubes ($\sim$ 1500 total) by Stone Industrial for prototype tests.

3. Purchase of Makrofol conducting polycarbonate foil, 0.5-mil thick. An attempt to copperize this failed. It can be aluminized to about 1 ohm per square by Sheldahl – this is the standard cathode material in use.

4. Purchase of conducting Kapton foil, 0.85-mil thick. Kapton can be copperized. 0.5-mil thickness is available, but with a $\sim$ \$200k minimum order.

5. Purchase of a spiral winding machine for the manufacture of straw tubes. However, no straws have yet been wound by us.

6. Construction of a clean 'shack' for assembly of straw tubes. This $10' \times 16'$ workspace achieves Class 1000 with no people present.

7. Purchase of a 2-m-long granite straight edge for precision alignment of straws during assembly.

8. Purchase of a set of 25 mandrels that can be inserted into straws during glueing.

9. Purchase of a N_2-driven glueing apparatus.

10. Assembly of a 21-tube prototype (along with M. Convery and D. Marlow of Princeton U.), using the mandrels and glueing apparatus of items 9 and 10.

11. Purchase of LeCroy electronics for this prototype (as the electronics expected to emerge from the Front-End Electronics Subsystem R&D are not yet available in sufficient quantity).

12. Construction of two kinds of wire-tension monitors. Results from these have pointed towards an improvement in the OSU scheme for tensioning the wire in the straws.

13. Pressure tests of straws, showing that the straws can hold 10 atmospheres.

14. Creep tests of straws, showing that a 2-m-long straw subject to a 1-lb weight stretches about 10 mils over a 2-month period. The straws also show expansion and contracting of about 10 mils during temperature shifts of 10°F (as expected from the known thermal-expansion coefficient).

15. Demonstration that straws could be pressurized during assembly, as an alternative to the use of mandrel inserts.

16. Design of an assembly fixture for 8-layer superlayers using grooved vacuum pads.

17. Design of a coaxial straw end-plug that incorporates gas and high voltage distribution, signal transmission, and wire tensioning. Custom high-voltage capacitors have been obtained for this.

18. Study of the wire instability in long straws, showing the effect of a wire offset, and of deformations in the straw.

19. Construction of several prototype straws for studies of gas gain and drift timing. Some modules can be pressurized.

20. Development of a technique using a 0.3-ns N_2 laser pulse to eject single electrons from the cathode wall of a straw.

21. Characterization of gas gain as a function of temperature, pressure, and applied voltage for several gas mixtures. Comparisons are made using both a Fe^{55} source and the N_2 laser; differences allow quantitative deductions about electron attachment. The gain spectra for single-electron avalanches are measured.

22. Measurements of timing (and hence spatial) resolution for single electrons, using the N_2-laser technique. The best performance observed (at 1 atmosphere) is 50-μm resolution in Ar/CO_2 (50/50) and CF_4/Isobutane (85/15) mixtures.

23. Comparison of amplifier performance between the LeCroy TR402 amplifier and the U. Penn straw-tube amplifier. The latter is measured to have about 1300-electron equivalent noise (15 times better than LeCroy), while contributing less than 0.5 ns to the timing uncertainty.

24. Development of a model of straw-tube response including characterization of the avalanche, electrical performance of the tube, and of the amplifier (with M. Lundin of Fermilab). This permits extrapolations of measurements with the N_2 laser to wider regimes.

25. Construction of a precision gas-mixing system, with control of both flow and pressure.

26. Initial development of a gas-analysis capability based on gas chromatography.

27. Simulation of overall system performance in the SSC environment (with L. Stutte of Fermilab).

We now present details on the topics just listed.

2 Straw-End Fittings

To begin work rapidly on various aspects of a straw-tube system we decided to adopt the set of straw-end fitting designed by an Ohio State U. group.[4] This saved over $10k in setup charges, but requires us to use 7-mm diameter straw-tubes until we implement our own designs. The choice of the O.S.U. design was based on a review various fittings now in use, with the judgement that their design is closest to what will be eventually desired.

In the future we shall seek lower mass fittings, and ones of smaller diameter. The aluminum collars would be advantageously replaced by plastic ones, but the latter must be gold-plated to provide electrical continuity. In the next year we will explore this with various vendors.

3 Winding of Sample Straws

When we first became involved in the study of straw tubes, almost all those in use were wound by Precision Paper Tube, who lately have been charging up to $10 a foot. We had small samples of straws made by two other vendors, Electrolock, and Stone Industrial, and both were satisfactory – indeed better looking to the eye than those from Precision Paper. Stone Industrial in particular has been very cooperative, and their price is only about $0.05 per foot.

4 Conducting Polycarbonate Foil

The straws wound for the O.S.U. group used a conducting polycarbonate foil for the cathodes. The foil has a resistance of about 1 ohm per square, which is not sufficient for use as an electrode by itself, so the foil is metallized before use. However, the conductivity of the cathode renders the straw relatively immune to scratches during assembly. Also, the carbon loading of the foil makes it opaque, which reduces noise current from photoemission at the cathode via room light.

The supply of the 0.5-mil-thick polycarbonate foil was, apparently, erratic until recently. Now the foil may be purchased in any quantity from Mobay Co., a U.S. subsidiary of Bayer in Germany. The cost is only about $0.10 per square foot, which is about the amount of material needed for a 2-m-long straw.

The polycarbonate foil is unfortunate in one respect, namely that it cannot be metallized with very thick layers before the material blisters. Sheldahl has succeeded in applying about 1000 Å of aluminum, resulting in the resistivity of 1 ohm/square stated above. But for a 2-m-long straw this implies a total cathode resistance of about 100 ohms, which approaches the transmission-line impedance of the tube.

We attempted to have the polycarbonate foil copperized, but the blistering was too severe. Discussion with many metallizing firms suggests that the performance achieved by Sheldahl is as good as possible with this material.

5 Conducting Kapton Foil

Repeatedly in discussion with metallizing firms it was mentioned that DuPont Kapton foil has superior thermal properties and should be able to support metallization thick enough to achieve the desired 0.1 ohm per square.

Transparent (and nonconducting) Kapton is readily available in 0.5-mil thickness, and the Indiana group has had samples aluminzied to 0.1 ohm per square by Sheldahl. DuPont also manufactures conducting Kapton, but the thinest readily available is 0.85 mil. We have purchased some of this material (at \$3 per square foot), and will have it metallized and wound into straws.

DuPont can make 0.5-mil thick conducting Kapton foil, but does so only on special order and has no current stock. Apparently the minimum order is about \$200k, beyond the range of prototyping budgets (unless an outside order comes in that we can attach ourselves to). Nonetheless, this 0.5-mil conducting Kapton foil would, we believe, be the material of choice for future straw construction.

6 Spiral Winding Machine

Alarmed by the high straw-tube prices of Precision Paper Tube, we located manufacturers of the spiral winding machines used to make the straws. We have purchased a small machine from Dodge Resources for \$10k. However, this machine is quite intricate to operate and we have not yet produced our own straws. Because of the low prices offered by Stone Industrial the urgency of manufacturing our own straws is much less than originally thought.

When long straws are delivered to us, some fraction of them have buckled during handling. Any small crease greatly reduces the straw's rigidity, and damaged straws will have to be rejected when constructing straw modules. Consequently, the yield of long defect-free straws may prove to be very low if they are provided by the commercial vendors. It may yet prove vital to have the straws manufactured in the same room that contains the module assembly. In this case we must master the technology of winding straws ourselves.

7 Clean 'Shack'

When commissioning any gas-filled detector, the dust particles left from the assembly procedures lead to large leakage currents and occasionaly catastrophic arcing. The remedy is assembly in a cleanroom. This is the only way to insure the reliability required for long-term running in a collider environment with limited access to the completed detector.

To gain experience in the use of cleanrooms, we purchased 6 HEPA filter units and mounted them in the ceiling of an inexpensive structure with $10' \times 16'$ useful floor area. The exhaust air blows out into the surrounding room, which also is the source of the input air. There is not temperature or humidity control other than that in the surrounding room. Nonetheless, this is a step in the right direction, and has been useful for the assembly of several small straw-tube chambers.

We continue to seek funding for a larger cleanroom, with a self-contained air-flow system including temperature and humidity control. Princeton University will provide matching

funds up to \$50k for this, and \$100k would permit us to establish a high-quality $16' \times 20'$ clean workspace plus the needed anteroom.

8 Granite Straight Edge

As discussed below, the straws must be extremely straight during use to avoid the electrostatic instability. Assembly of the straw modules must be done with fixtures that intrinsically have the desired straightness. This can be achieved by mounting the assemble fixture on a granite surface plate, which is flat to better than 4 μm over 2 m.

For our initial prototype modules we have purchased a granite straight edge whose flat surface is 20 cm wide and 2 m long. We have built a stand for this that permits the straight edge to be used either vertically or horizontally. For the assembly of larger straw modules in the next year we seek to purchase a wider surface plate as well.

9 Mandrels

In the assembly procedure devised by the O.S.U. group, polished steel mandrels are inserted into the straws as they are glued together into modules. While the 1-mil-thick straws cannot support transverse stresses, the steel mandrels permit the straws to be squeezed together during the gluing, and can be held in precision alignment during this time.

We have purchased a set of 25 mandrels for a small prototype module, but the mandrels cost \$200 each. Serious consideration must be given as to whether the use of such mandrels is required, due to their cost.

10 Glueing Apparatus

The technique for gluing straws into modules is the subject of some debate. Earlier efforts by other groups have often used rather massive amounts of glue, which is undesirable due to multiple Coulomb scattering. We have purchased a glue gun that operates under N_2 pressure to deliver a uniform bead. Very small amounts of glue can be controllably dispensed with this device.

11 21-Tube Prototype

Our first multitube straw-module contains 21 tubes in two layers, as shown in Fig. 1. It was assembled using steel mandels that held the tube during gluing the the N_2 glue gun. The gluing procedure was very satisfactory and should be applicable to much larger scale.

This prototype was built in collaboration with Mark Convery and Dan Marlow of Princeton U., who are interested in using a straw-tube detector in an upgrade to the ongoing BNL experiment 787.

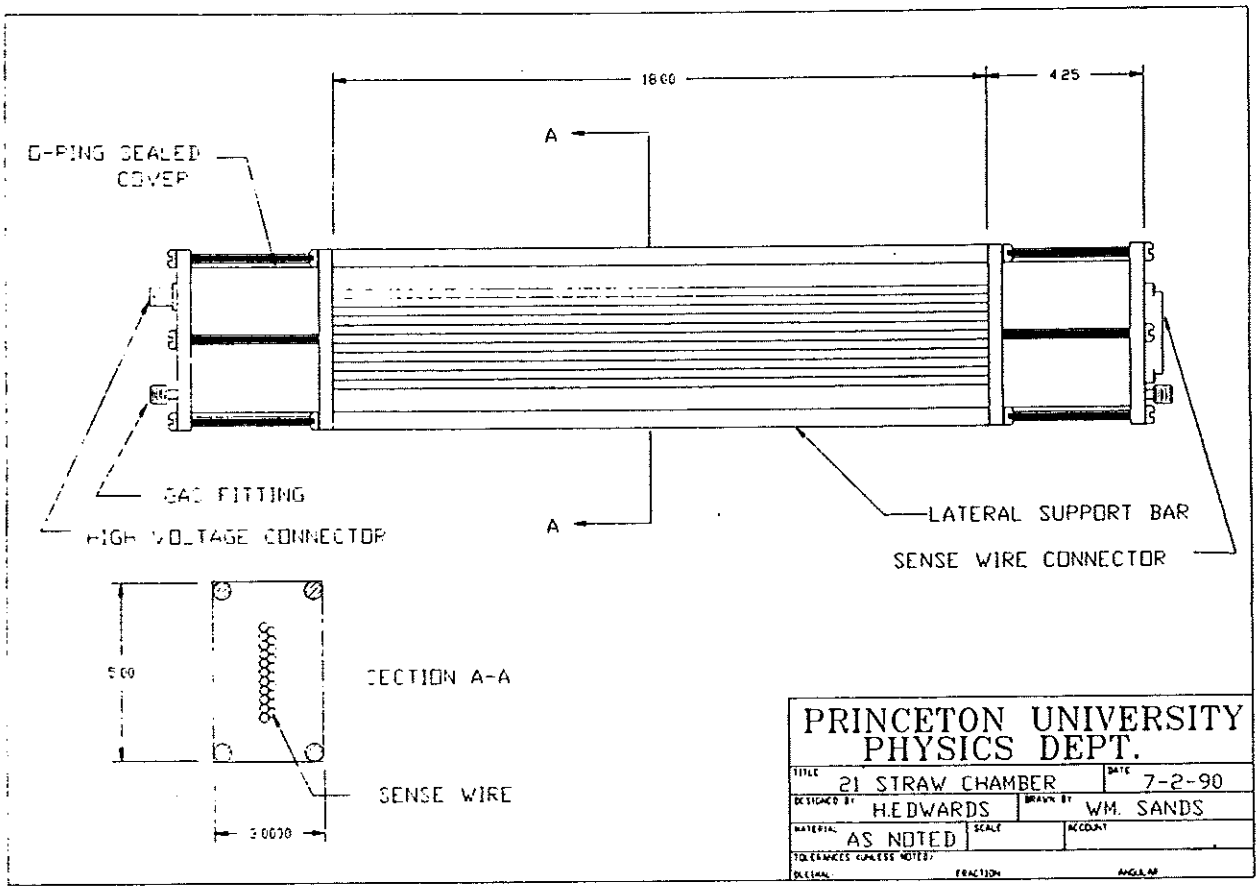

Figure 1: The 21-tube prototype module.

12 LeCroy Electronics

Front-end electronics optimized for use on straw tubes are not yet available in quantity, although an excellent design is in prototype phase at U. Penn. We have purchased 64 channels of LeCroy 2735DC amplfiers for use in tests in the next few months of prototype modules such as the one just described. The needed TDC modules have been obtained on loan from equipment pools of Fermilab and BNL.

We eagerly await even modest quantities of the Penn amplfiers. Tests of modules of more than 100 or so straws will otherwise require significant investment in obsolescent electronics.

13 Wire-Tension Monitors

Once a straw-tube detector is assembled its anode wire is inaccessible. Therefore a means to verifying the wire tension via external measurements is required.

We are exploring two methods of monitoring the wire tension, with the goal of a procedure that can be implemented by technicians rather than physicists. In the first method an ac current is sent down the anode wire of a straw module that has been placed in a magnetic field. At the natural frequency of the wire, $\nu = (4/L)\sqrt{T/\rho}$, the oscillation of the wire induces a voltage in the circuit via Faraday's law.[5] This small effect is detected as a phase

shift, as shown in Fig. 2.

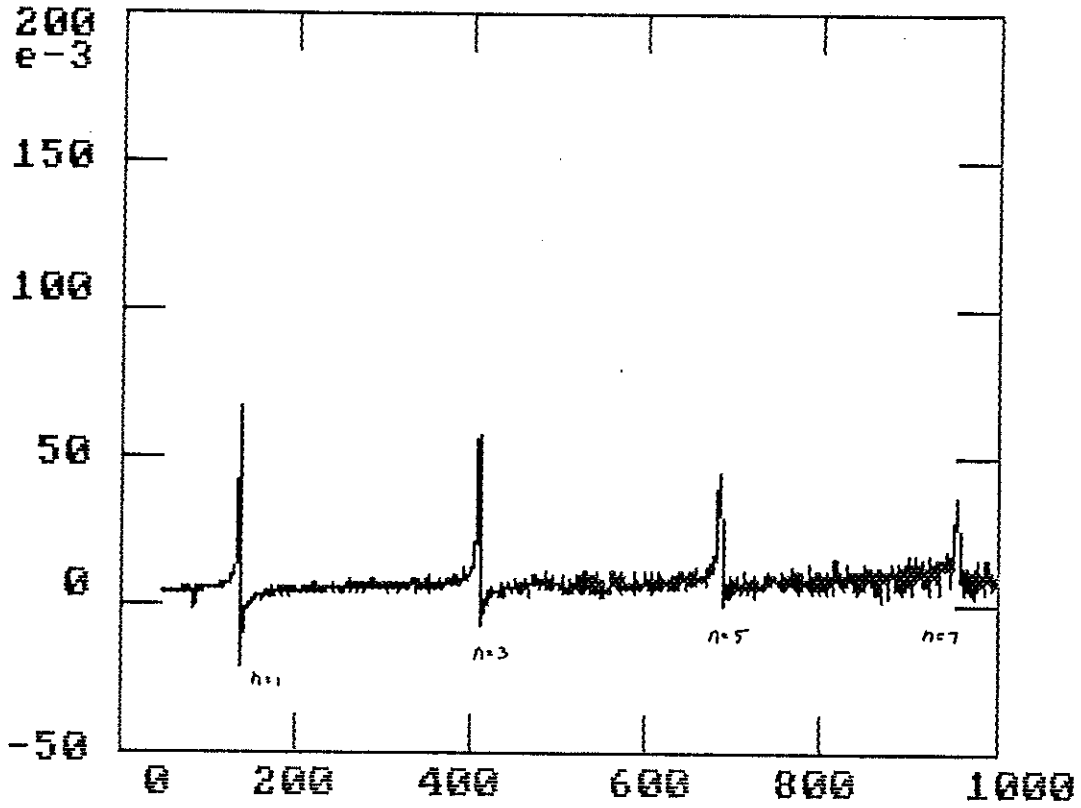

Figure 2: The phase shift induced as a function of applied frequency in a circuit to test the wire tension in an assembled straw. The straw is placed in a magnetic field, which results in a change in the complex impedance of the circuit when the wire oscillates at a mechanical resonance.

This technique has been useful in revealing a much-too-large incidence of loose wires in our assembly procedure. This has been largely remedied by a modification to the O.S.U. feedthrough (that will require a new mold for large-scale implementation). However, the technique has not been fully automated, due to a tendency for the computer to get badly lost if the wire is far from its nominal value.

We are bringing up a second technique for wire tension measurements, following work at Fermilab.[6] This is a more robust technique for detecting the resonance in which a voltage-controlled oscillator is used to sweep across the expected resonance region, and the voltage generated by the oscillation of the wire in the magetic field is measured using a sensitive bridge circuit to null out the driving frequency.

We may wish to consider a third alternative. When struck by a sharp blow or a fast pulse, electromechanical systems will respond at the resonant fequency and undergo an exponentially damped series of oscillations. This technique is exploited by the meter produced by KFKI, Central Research Institute for Physics, P.O.Box 49, H-1525 Budapest Hungary. It is exported by Metrimpex The Hugarian Trading Company for Instruments, Munnich Forenc utca 21, 1051 Budapest V. The price in 1982 for this machine was $3,500.

This device offers a quicker measurement than the previous two as a scan over several frequencies does not have to be made. Also the actual measurement is done when the impulse or driving force, has been removed. The other two methods have to locate a small signal in the presence of a much larger one.

All the wire tension methods rely on there being a strong magnetic field around the center of the straw. In some of the larger arrays this will be difficult to achieve with the existing permanent magnets that have a small jaw which limits how far into the array the magnetic field can be moved. Horseshoe magnets and electromagnets are being experimented with.

14 Pressure Tests

The straws manufactured by Electrolock and Stone Industrial both held pressure up to 10 atmospheres before bursting a somewhat larger pressures. Operation of straw tubes somewhat above atmospheric pressure would be advantageous due to the increased mechanical rigidity, and the improved spatial resolution.

15 Creep Tests

A 7-mm-diameter, 2-m-long straw wound by Stone Industrial from one ply each of 0.5-mil Mylar and 0.5-mil conducting polycarbonate was suspended with a 1 pound weight. The vertical force is equivalent to operation of this straw at 1 atmosphere overpressure. Figure 3 shows the resulting longitudinal extension as a function of time, along with the temperture in the (unairconditioned) room.

16 Buckling

A tube of length L will buckle under a load force F if the load exceeds the Euler condition:

$$F = \frac{\pi^2 EI}{L^2},$$

where E is the Young's modulus of the material of the tube, and $I = \int x^2 dxdy$ is the bending moment of the tube. For a hollow tube of radius R and thickness T (such as a single straw) we have $I = \pi R^3 T$, while for an $N \times N$ bundle of straws we have $I = \pi(N^2+1)R^3T/2$ as the average moment per straw.

The force per straw for buckling is then

$$F = \frac{\pi^3 ER^3T}{L^2}$$

for a single straw, and

$$F = \frac{\pi^3(N^2+1)ER^3T}{2L^2}$$

as the buckling force per straw for an $N \times N$ bundle. The buckling force can be quite low for long thin straws!

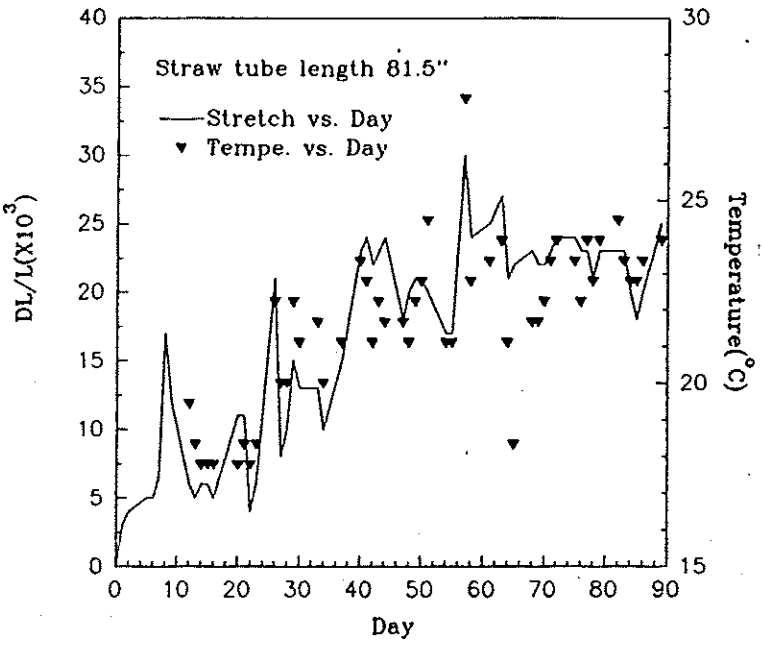

Figure 3: Creep of a 2-m-long straw subject to a 1 pound weight as a function of time and temperature. The largest effect is correlated with the ambient temperature, and matches the expected thermal expansion of the straw.

For Mylar, Kapton, and the Makrofol polycarbonate film, the Young's modulus E is about 500,000 PSI $\approx 3.5 \times 10^7$ gm/cm^2. (For convenience we will measure force in 'grams,' meaning the weight of the given number of grams.) Then for $R = 3.5$ mm and $T = 25$ μm we have

$$F[\mathrm{gm}] = \frac{12}{L^2[\mathrm{m}^2]}$$

for a single straw, and

$$F[\mathrm{gm}] = \frac{6(N^2+1)}{L^2[\mathrm{m}^2]}$$

per straw for an $N \times N$ bundle of straws.

For example, the 7-mm-diameter straws we are now using are expected to buckle under the typical 50-gm tension on the anode wire if $L > 0.5$ m. Indeed, we have made several 1-m-long straws with 50-gm tension, and if left unsupported they buckle slightly until the tension drops. (This buckling is not a catastrophic mechanical failure, but just a bowing of the tube; however, this renders the tube useless as a particle detector.)

Our interest has been in straws of lengths up to 2 meters. The buckling expression suggests that an 8×8 bundle of 2-m-long straws of 7-mm-diameter could sustain wire tensions of up to 98 grams. If the tube diameter were reduced to 5 mm, the maximum wire tension would be only 36 grams.

We will empirically explore the validity of the Euler expression for bundles of 2-m-long straws in the near future.

It is unlikely that bundles of straws 4-6-m long and 4-mm diameter (as proposed for the SDC detector) can be self supporting against buckling due the anode wire tension.

Other members of the Straw-Tube Subsystem collaboration are considering the use of various external supports for the straws. We will continue to pursue the option of self-supporting straw bundles, whose necessarily shorter length is still relevant to the requirements of a B-physics detector.

17 Assembly of Pressurized Straws

One idea that is being persued is to locate the tubes using their outer surface instead of the inner. This avoids the problem of inserting steel rods (mandrels) the tubes to support and align them, which can result in damage to the internal surface. The mandrels are also rather expensive ($\sim$ \$200 each). However, the tubes are so fragile that if the are not internally supported, any external pressure used to align the tube results in their being distorted. We have therefore experimented with pressurized tubes to get round this problem. For the 7-mm-diameter tubes that are being used at present, it was found that a standard tire valve fitting could be inserted easily into the ends. This facilitates the pressurization of the tubes to 14 p.s.i. at which pressure they are firm and rigid. To use this method requires a small modification to the aluminum inserts shown in Fig. 5 below. The new insert will have an internal thread and conical shoulder to permit sealing of the tire valve. After use the valve would be unscrewed and used again.

Our prototype procedure for assembling the pressurized straws into modules is described in the next section.

18 Eight-Layer Assembly Fixtures

A fixture is now being made to hold the pressurized Straws together for the glueing process. This consists of a set of clamps spaced every 10 cm or so down the length of the straws. The glue is applied to the exposed lengths of Straw in between the clamps. The clamps are accurately machined using an NC device and are shown in Fig. 4. With this jig a complete array or "superlayer" of 64 tubes can be glued and assembled.

19 Straw End-Plug Design

At the ends of each module are structures that serve to maintain the tension and alignment of the anode wires, direct the flow of gas in and out of the straw tubes, and carry the electrical signal of the detectors to the preamplifiers, which are also to be mounted on these endcaps. A design to satisfy all these functions is quite intricate and will lead to a structure of at least 2% of a radiation length. Fig. 5 shows a preliminary design for the endcaps.

As mentioned earlier, after testing several straws assembled with the O.S.U. end fittings we found that the wire tension had relaxed during assembly. We have made a modification to the Ultem plastic feedthrough, as shown in Fig. 6, to rectify this. The feedthrough is slotted on the end that receives the brass taper pin, and a new plastic collar is added to clamp the feedthrough to the taper pin.

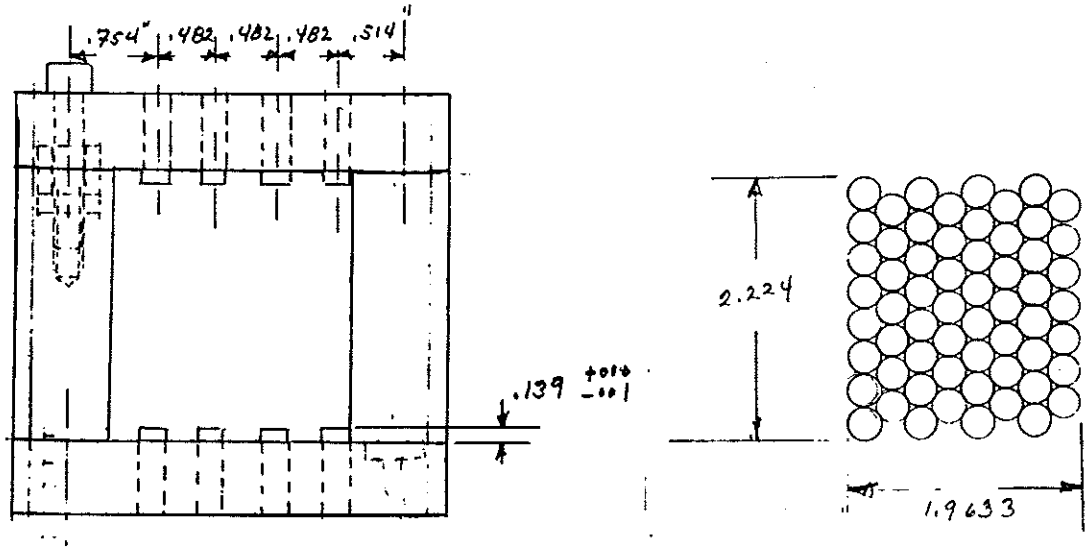

Figure 4: Preliminary sketch of the assembly fixture for eight-layer straw modules. The figure on the right shows the completed straw bundle in the orientation as it is built in the fixture on the left.

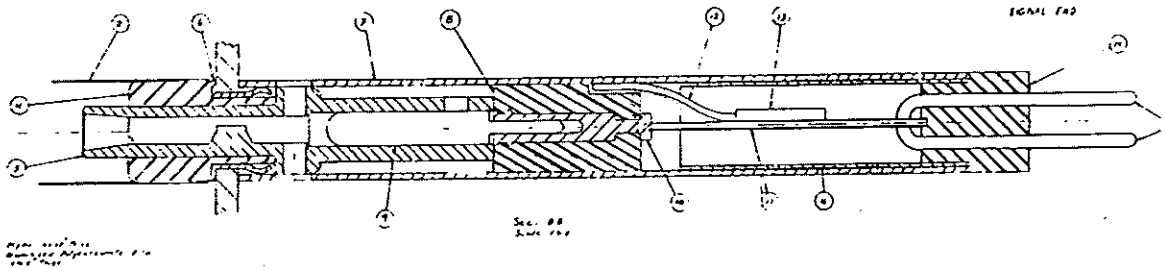

Figure 5: Possible scenario for a straw-tube end plug: **2**: the straw tube; **4**: aluminum insert; **5**: Ultem feedthrough; **6**: collar spring; **7**: metallic sleeve; **8**: plastic socket; **9**: taper pin; **10**: pin socket; **11**: G-10 board with anode lead on bottom; **12**: cathode lead; **13**: blocking capacitor; **14**: plastic collar; **16**: Mylar sleeve. The anode- and cathode-signal pins at the right end plug into the front-end electronics board. The vertical plate at the left is made of Macor.

It should be possible to make this modification in the molds for the plastic feedthroughs without the full expense ($\sim$ \$10k) of retooling. We are exploring this with the manufacturer of the plastic feedthroughs.

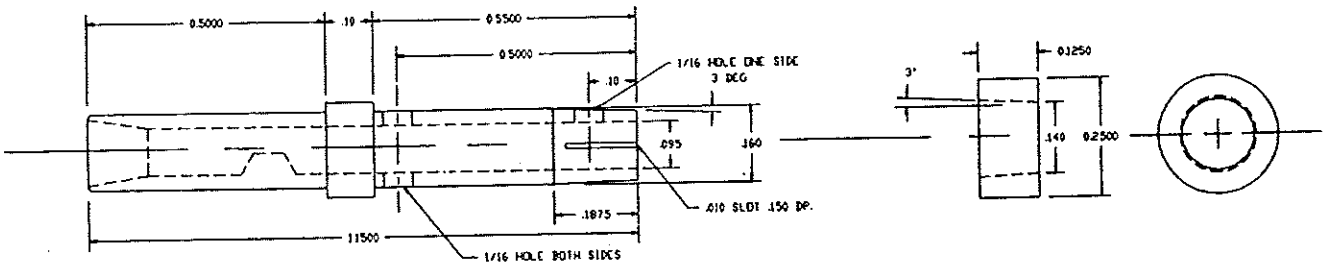

Figure 6: Modification to the plastic feedthrough.

20 Gas-gain study

In designing a gas wire chamber, the gas gain always is one of the most important and most basic considerations. Many experimental studies have been carried out to determine the gas gain of various counters under differing gas conditions, and several gas-gain formulae to fit the experimental data have been proposed.[7, 8, 9, 10, 11, 12, 13] It will be useful to identify the theoretical formula which best fits our straw-tube data.

A prototype module of straw tubes has been used for this study. It consists of seven short straw-tube counters, each 7 cm in length and 0.7 cm in diameter. The straw tube itself is made of a two-ply laminate of an inner polycarbonate film about 14 μm thick surrounded by a layer of 12.5-μm Mylar. The polycarbonate film is aluminized on its inner surface to about 1000 Å thickness. The tubes and end plugs were obtained from Ohio State U.[4] The seven tubes have five different anode wire sizes: 0.0203, 0.0254, 0.051, 0.076, and 0.127 mm diameter.

This summary is based on four kinds of gas mixtures, P-10 [= Ar/CH_4 (90/10)], Ar/C_2H_6 (50/50), Ar/CO_2(50/50) and Ar/CO_2(20/80); subsequently many others have been studied. We used an Fe^{55} source and measured the charge out of the test chamber with an Ortec model 142PC preamplifier, followed by an Ortec model 570 spectroscopy amplifier, whose output was digitized by an Ortec model 916 multichannel analyzer. A calibration of the charge out of the chamber per count in the 916 analyzer was obtained with an Ortec model 419 precision pulser (by charging a 2 pf capacitor). The primary ionization caused by the Fe^{55} is taken to be 220, 223, 192, and 179 electrons in P-10, Ar/C_2H_6 (50/50), Ar/CO_2 (50/50), and Ar/CO_2 (20/80), respectively. This is based on an average energy loss per ion pair created of 26.8, 26.5, 30.8, and 33.0 eV in these four gas mixtures,[14] noting that the x-ray energy is 5.9 keV. (This amount of ionization from Fe^{55} has been experimentally validated by us as discussed in sec. 28 below).

The data on gas gain *vs.* high voltage for Ar/CO_2 (50/50) and Ar/Ethane (50/50) are shown in Fig. 7. For gas gains larger than 2.5×10^4, the signal charge due to the 5.9-keV x-rays will exceed 1 pC and the chamber will no longer be in the proportional mode. Therefore we have restricted our studies to gains below this value.

Among various gas-gain formulae, we used three to fit our experimental data, namely those of Diethorn,[8] Aoyama,[12] and Kowalski.[13]

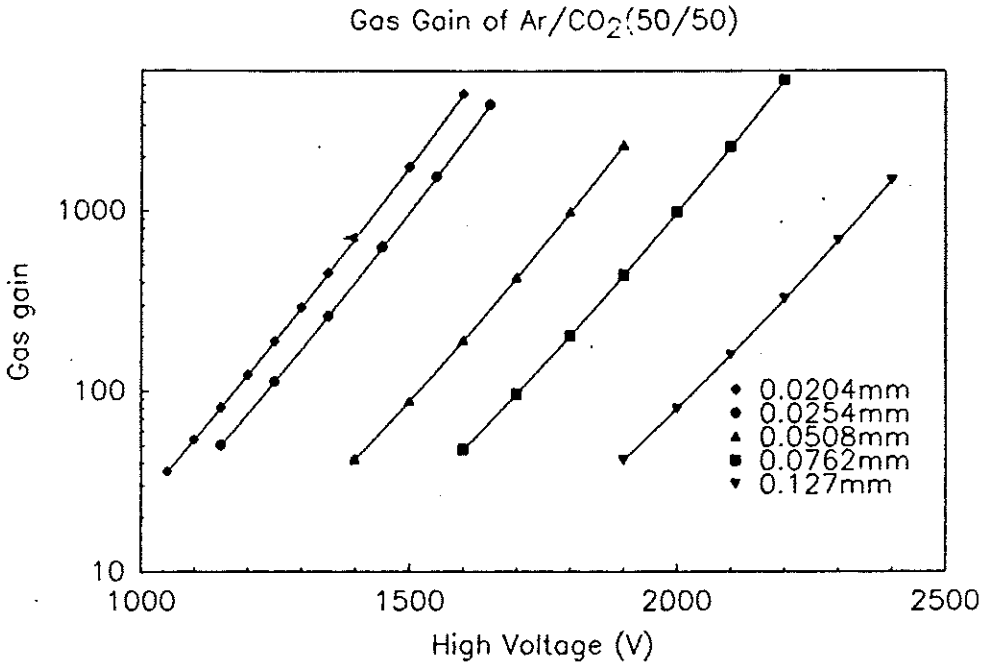

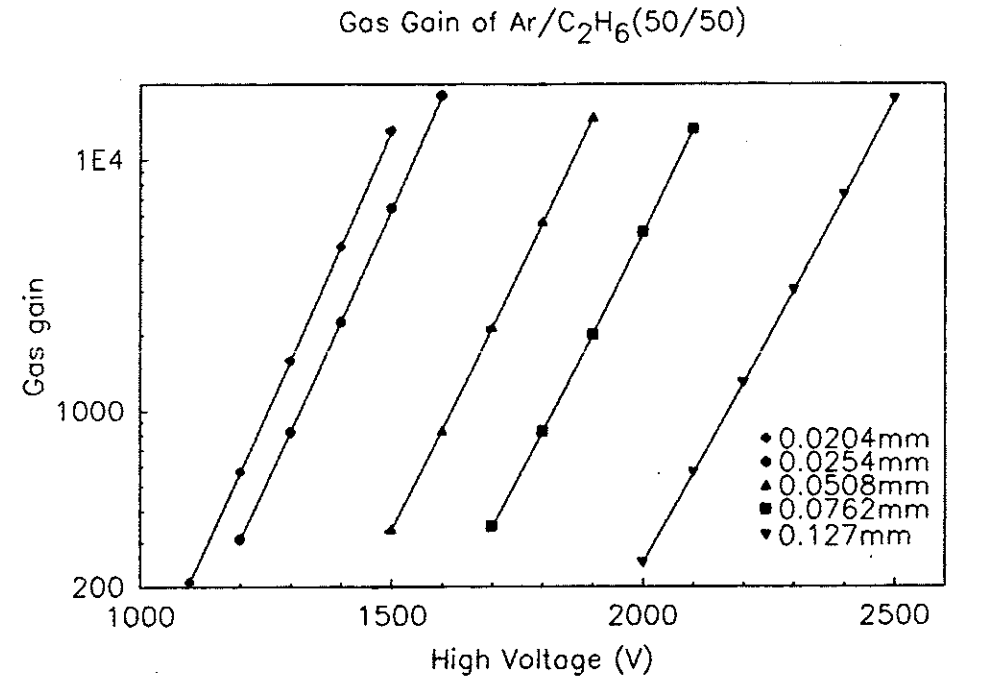

Figure 7: (a). Gas gain *vs.* voltage for straw-tube chambers with five different anode-wire diameters, filled with Ar/CO_2 (50/50) gas. 1(b). Gas gain *vs.* voltage for straw-tube chambers with five different anode-wire diameters, filled with Ar/Ethane (50/50) gas.

Diethorn's formula is

$$\frac{\ln G}{V/\ln(R_c/R_a)} = \frac{\ln 2}{\Delta V}\left(\ln \frac{V}{PR_a \ln(R_c/R_a)} - \ln K\right). \quad (1)$$

Here ΔV corresponds to the potential difference through which an electron moves between successive ionizing collisions, and K is the minimum value of E/P below which multiplication cannot occur. Throughout this paper, G is the gas gain, V is the voltage applied to the tube, E is the (position dependent) electric field strength, P is the pressure, R_a is the radius of the anode wire, and R_c is the radius of the cathode surface of the straw tube.

Aoyama's formula is

$$\frac{\ln G}{V/\ln(R_c/R_a)} = \exp\left\{-A\left(\frac{V}{NR_a \ln(R_c/R_a)}\right)^{m-1} - \ln[(1-m)V_I]\right\}, \quad (2)$$

where V_I is the effective ionization potential, and A and m are constants characteristic of the gas.

Table 1: Variances and parameters of the fitting.

Gas mix	Fit type	Variance	Fitted parameter
Ar/CO_2 (50/50)	Diethorn	7.584×10^{-7}	$\Delta V = 41.3$ eV; $K = 4.736 \times 10^4$ V/cm·atm
	Aoyama	6.298×10^{-7}	$A = 1.376 \times 10^{-7}$; $m = 0.5$, $V_i = 16.8$ V
	Kowalski	6.276×10^{-7}	$A_1 = 0.543 \times 10^{-2}$ (m·Pa)$^{d-1}$V^{-d}; $d = 1.228$, $B_1 = -0.05536$/V
Ar/Ethane (50/50)	Diethorn	2.014×10^{-7}	$\Delta V = 31.58$ eV; $K = 4.84 \times 10^4$ V/cm·atm
	Aoyama	1.141×10^{-7}	$A = 0.1141 \times 10^{-6}$; $m = 0.4942$, $V_i = 12.86$ V
	Kowalski	1.031×10^{-7}	$A_1 = 0.5578 \times 10^{-2}$(m·Pa)$^{d-1}$V^{-d}; $d = 1.277$, $B_1 = -0.05594$/V

Kowalski's formula is

$$\frac{\ln G}{V/\ln(R_c/R_a)} = \frac{A_1}{d-1}\left(\frac{V}{PR_a \ln(R_c/R_a)}\right)^{d-1} + B_1, \quad (3)$$

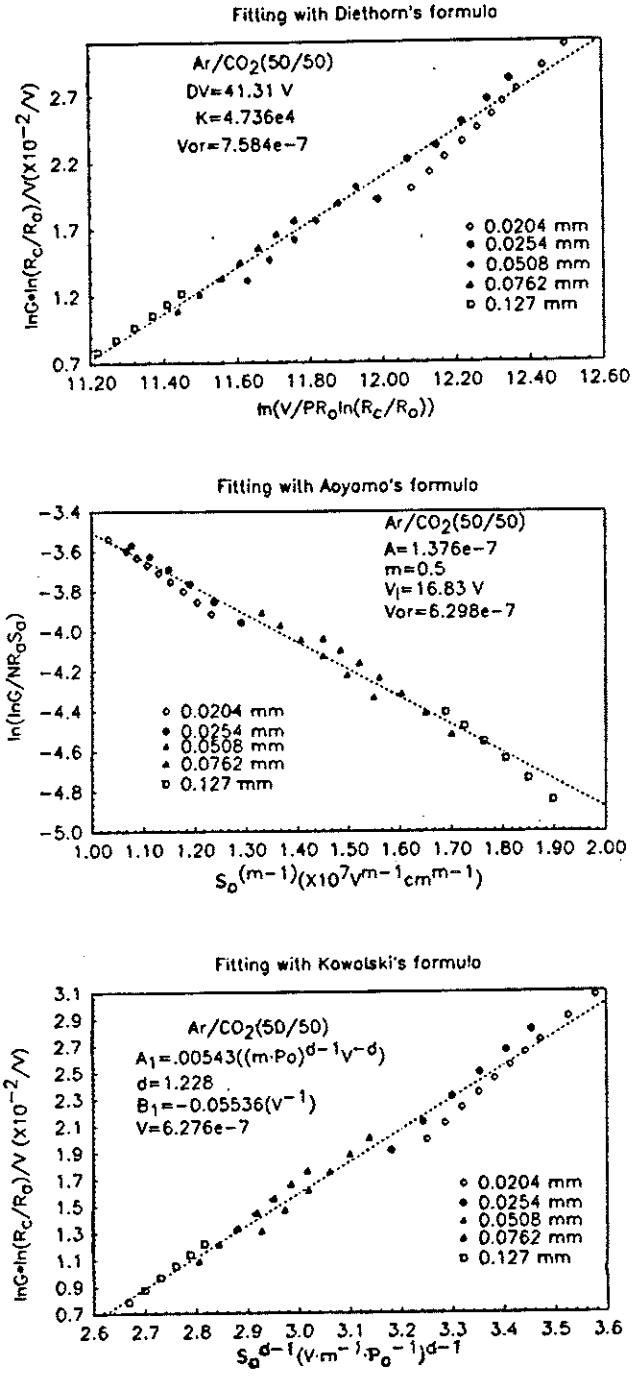

Figure 8: Model fits to the gas gain in gas.

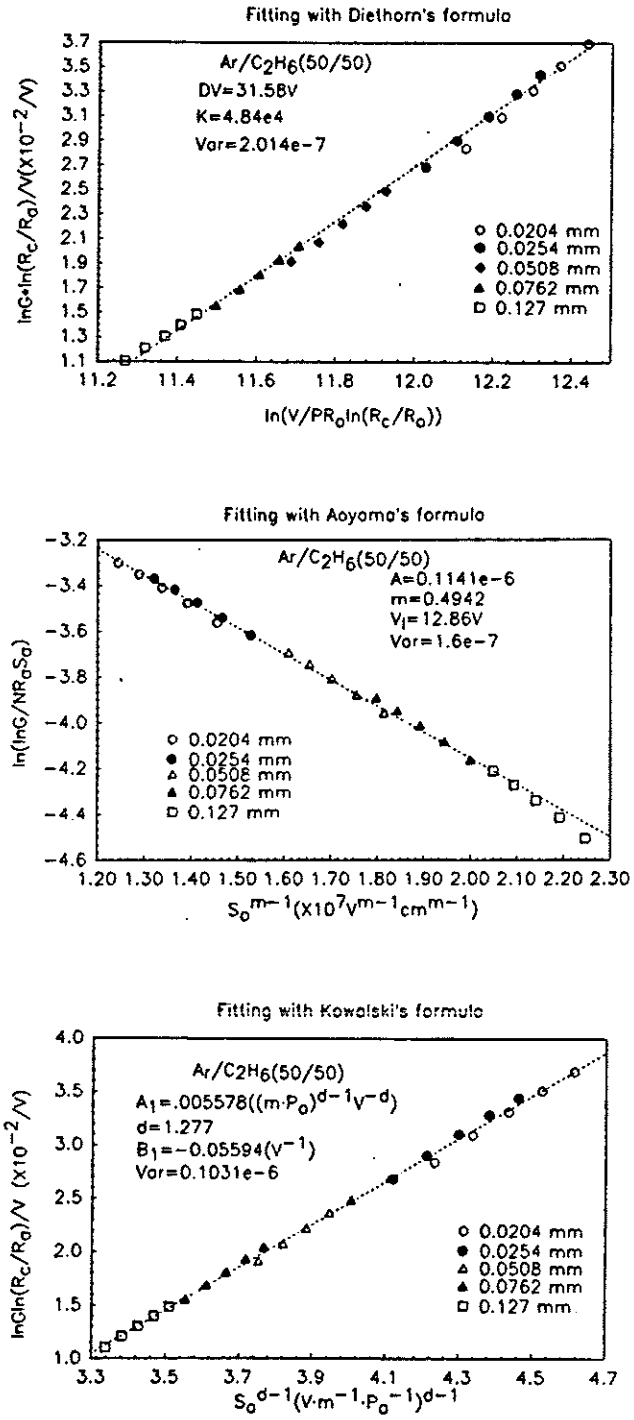

Figure 9: Model fits to the gas gain in Ar/Ethane (50/50) gas.

where A_1, B_1, and d are constants of the gas.

The data points and fitted lines are shown in Fig. 8 and Fig. 9 for AR/CO_2 (50/50), and Ar/Ethane, respectively. The variance used in the fitting for all of three formula is defined in the same way as

$$\text{Variance} = \sum_{i=1}^{n} \left(\frac{\ln(G_{\text{data}})_i}{V_i/\ln(R_c/R_{a,i})} - \frac{\ln(G_{\text{fit}})_i}{V_i/\ln(R_c/R_{a,i})} \right)^2 \Big/ n, \tag{4}$$

so we can directly compare their goodness of fit. The results are summarized in Table 1. For the other two gas mixtures the goodness of fit is similar.

Only slight differences exist among the fits using the three models, so any could be used for the range of conditions we are studying.

21 Temperature Dependence of the Gas Gain

The heat dissipation due to the electron/ion currents in a straw tube that comes within 10 cm of the beams at 10^{32} luminosity at SSC is 1/3 mWatt.[15] This will heat up the gas and consequently the gas gain will be changed. In order to keep the gas gain within a desired range, the gas flow rate must be adequate to cool the heat load. But a large flow rate is difficult to accommodate in a compact straw-tube design, so it is important to know how strong is the temperature dependence of the gas gain.

21.1 Experimental Results

Because of an apparent lack of relevant data in the literature, we have placed the test chamber in an oven to make direct measurements of the temperature dependence. We are able to maintain a constant temperature inside of the oven to $\pm 0.5°C$, as monitored by a a thermocouple and microvoltmeter. The gas-flow rate was reduced to a very low level to insure that the gas temperature inside the chamber was that of the surrounding oven.

Figure 10 shows the experimental results for the P-10 gas mixture and the 0.0204-mm anode-wire chamber. Those for Ar/Ethane with 0.0204- and 0.127-mm anode-wire chambers are shown in Fig. 11. From these figures we draw the following qualitative conclusions:

1. The gas gain increases with temperature.
2. Different gas mixtures shows different temperature dependences; Ar/Ethane (50/50) is about 2.5 times as sensitive to temperature changes as P-10.
3. The temperature dependence of a 5-mil-diameter anode wire is about twice that of a 0.8-mil one;
4. The temperature dependence is stronger at larger gas gain.
5. A characteristic value of $(dG/G)/(dT/T)$ is 5, as for Ar/Ethane (50/50) with an 0.8-mil-diameter anode wire and a gas gain of 10^4. But see Fig. 12 for variations with gas type, gain, and anode-wire diameter.

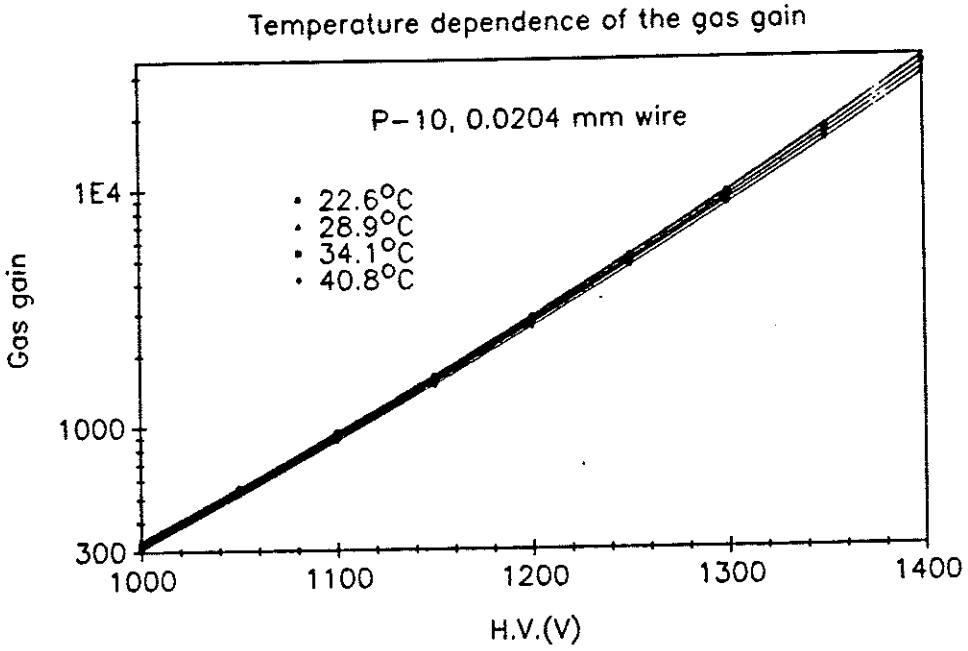

Figure 10: Temperature dependence of the gas gain in Ar/CO_2 (50/50) gas with an 0.8-mil-diameter anode wire.

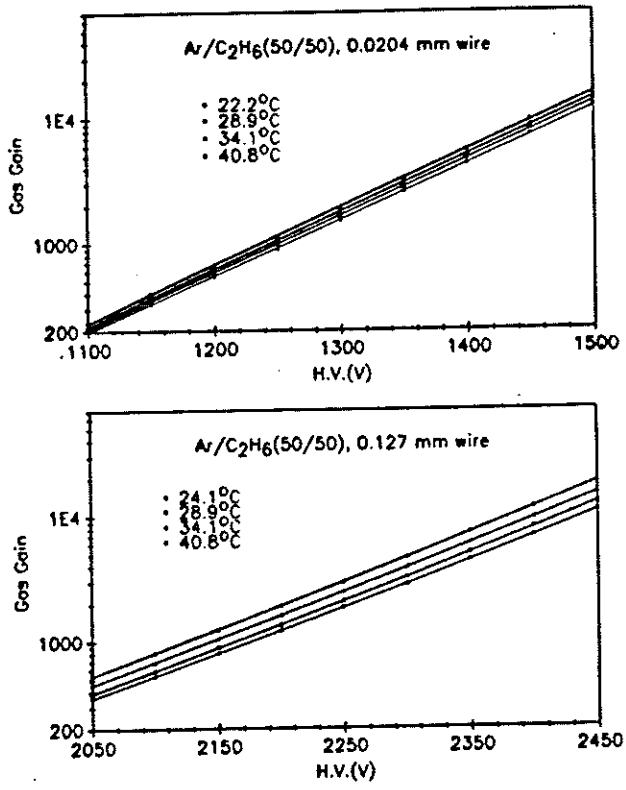

Figure 11: Temperature dependence of the gas gain in Ar/Ethane (50/50) with 0.8-mil and 5-mil-diameter anode wires.

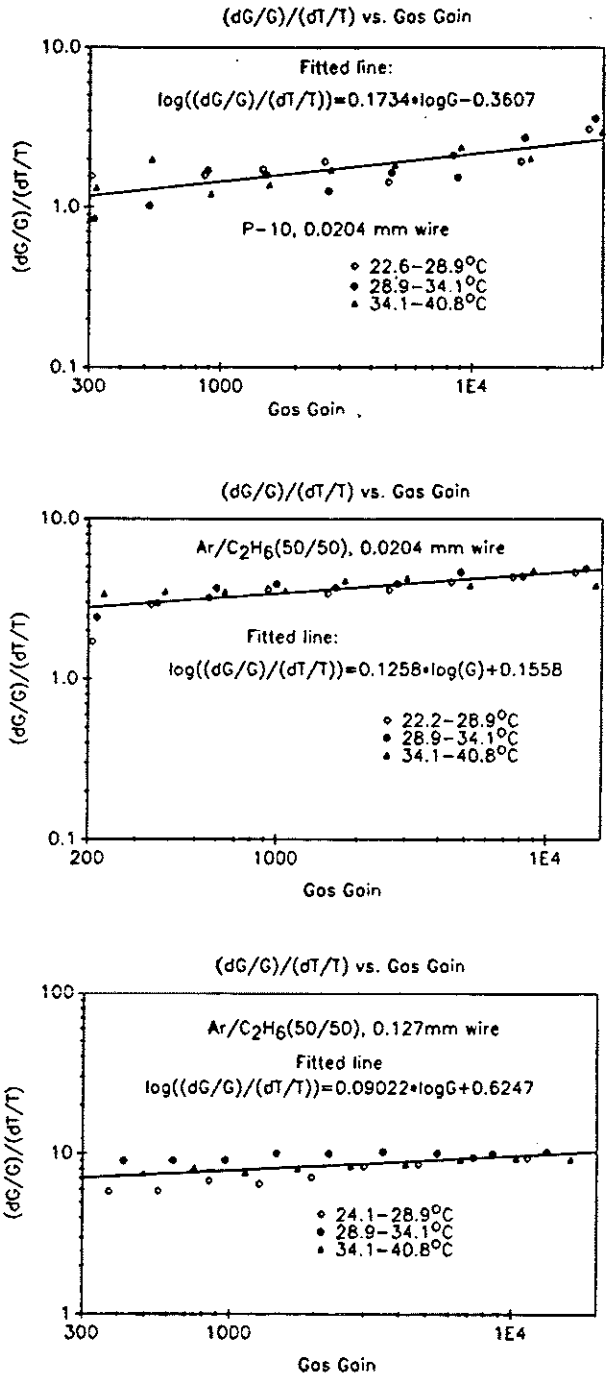

Figure 12: The ratio of relative gain change (dG/G) to the relative temperature change (dT/T) as a function of the gas gain in P-10 and Ar/Ethane (50/50) for 0.8-mil and 5-mil diameter anode wires.

21.2 Model Interpretation

Among the early works on gas amplification the well-known model proposed by Rose and Korff[7] has been cited by many authors. But this model is inadequate to reproduce the temperature dependence observed by us. The gas-gain formula derived from their model can be written as

$$\ln G = 2\sqrt{\frac{KNR_aV}{\ln(R_c/R_a)}}\left(\sqrt{\frac{V}{V_t}}-1\right), \tag{5}$$

where N denotes the gas density, V_t is the threshold voltage at which amplification starts to take place, and K is a constant.

The basic assumption of Rose and Korff was that

$$\alpha(r) = \langle N\sigma(U)\rangle,$$

where $\alpha(r)$ denotes the Townsend coefficient (defined by $dn/n = -\alpha(r)dr$ where n is the number of ionization electrons), and $\sigma(U)$ is the ionization cross section as a function of the electron energy U. The dependence of α on the electric field E is through the latter's effect on the spectrum of energies U.

Assuming the gas pressure of the counter remains constant while the temperature is changing, it follows that

$$\frac{dN}{N} = -\frac{dT}{T}. \tag{6}$$

The gas density decreases with increasing temperature; therefore α decreases too, according to the model of Rose and Korff, and as a consequence the gas gain decreases. This contrasts with our observation that the gas gain increases with increasing temperature.

Aoyama's model[12] is based on different assumptions. He expressed α as $1/\lambda_r$ – the number of mean free paths per unit length in the field direction – multiplied by the chance of a free path length longer than λ_I – the mean path length for an electron to travel in the field direction to ionize a gas molecule, *i.e.*,

$$\alpha = \frac{1}{\lambda_r}e^{-\lambda_I/\lambda_r}, \tag{7}$$

where $\lambda_I = V_I/E$, and V_I is the effective ionization potential.

We can write

$$\frac{1}{\lambda_r} \approx \frac{1}{\lambda} = N\sigma,$$

since the mean free path along the field direction is approximately the same as the overall mean free path. Then the Townsend coefficient α is approximately given as

$$\alpha = N\sigma\exp(-N\sigma V_I/E). \tag{8}$$

It follows that

$$\frac{d\alpha}{dN} = \sigma(1-\lambda_I/\lambda_r)\exp(-N\sigma V_I/E). \tag{9}$$

The sign of $d\alpha/dN$ will depend on the ratio of λ_I to λ_r. On differentiating both sides of eq. (2) and taking eq. (6) into consideration we obtain

$$\frac{dG/G}{dT/T} = A(1-m)\ln G\left(\frac{E_a}{N}\right)^{m-1} = A(1-m)\ln G \cdot S_a^{m-1}, \tag{10}$$

where we have introduced $S_a \equiv E_a/P$ as the ratio of the electric field strength at the anode wire to the gas pressure. Similarly from eq. (1) and eq. (3) we get the following predictions according to Diethorn and Kowalski, respectively:

Diethorn's prediction:

$$\frac{dG/G}{dT/T} = \frac{\ln 2}{\Delta V \cdot \ln(R_c/R_a)}V. \tag{11}$$

Kowalski's prediction:

$$\frac{dG/G}{dT/T} = \frac{A_1}{\ln(R_c/R_a)}(S_a^{d-1} \cdot V). \tag{12}$$

Figure 13 shows the comparison between our experimental data and these model predictions. The general trends are rather well predicted, but none of the models is able to make perfect predictions. The numerical disparities are within a factor of 2, and the experimental data are always below the model predictions, in which the model parameters were fitted using data taken at a constant temperature.

In summary:

- The gas-gain formulae proposed by Diethorn, Aoyama, and by Kowalski are able to describe the general behaviour of temperature dependence, and the predicted values could be safely used as upper limits.
- The most favorable (*i.e.*, smallest) empirical values for $(dG/G)/(dT/T)$ are about half of the predicted values.

22 Electrostatic Instability of the Straw-Tube Chamber

Our goal is to build a large straw-tube tracking system. The length of each straw tube will be up to 2 m. It will greatly simplify the construction process and reduce the inefficient zone of the straw tube chamber if an extra support in the middle of the anode wire can be avoided.

Cylindrical wire chambers are prone to an electrostatic instability in which the anode wire is pulled toward the cathode if the fields are strong enough. A general formula for the maximum high voltage of stable operation of a straw tube chamber has been derived:[16]

$$V < \sqrt{\frac{T}{2\pi\epsilon_0}}\frac{\pi R_c}{L}\ln\left(\frac{R_c}{R_a}\right) \equiv V_0, \tag{13}$$

where T is the tension of anode wire (Newtons), L is the length of wire (m), and $\epsilon_0 = 8.85 \times 10^{-12}$ F/m. We will generalize this below.

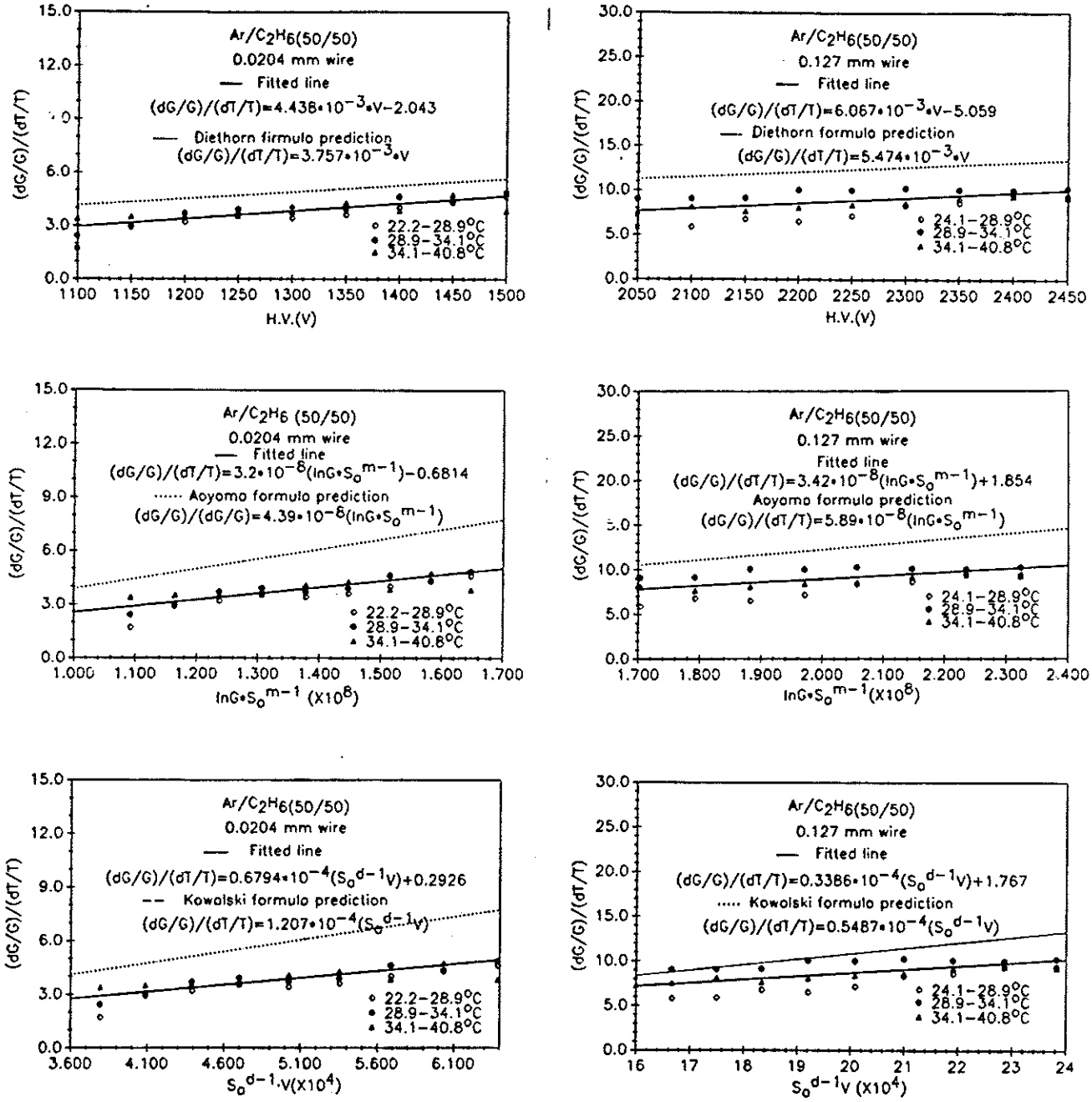

Figure 13: Comparison of experimental data on the temperature dependence of the gas gain with several models whose parameter were determined at a fixed temperature.

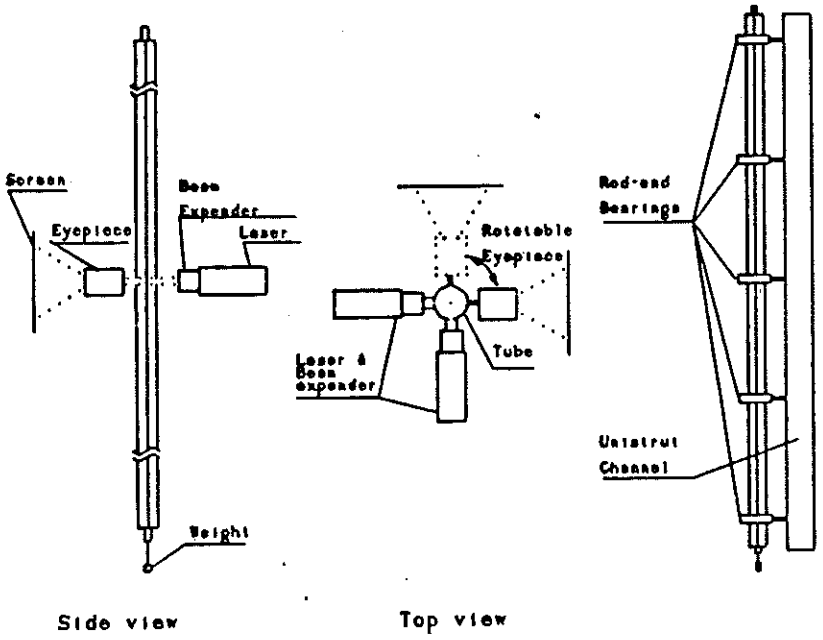

Figure 14: Sketch of the setup to study the electrostatic instability of the anode wire. The left view shows the optical system to observe the deflection of the anode wire. The right view shows the mechanical alignment of the tube.

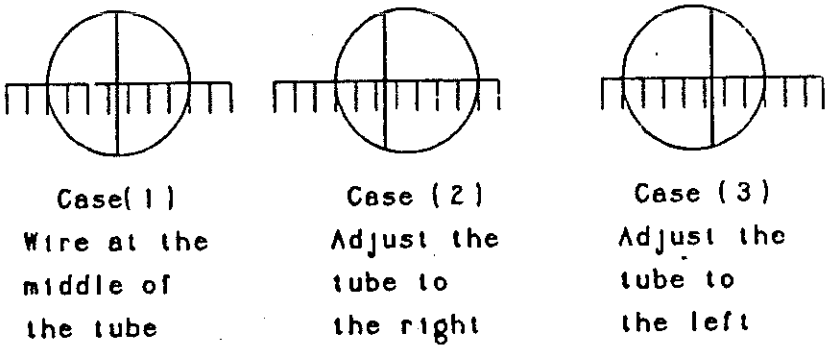

Figure 15: Illustration of the effect of an anode-wire offset as observed on the viewing screen.

We have studied the accuracy of eq. (13) with a 2-m-long tube, as sketched in Fig. 14. A 6.35-mm inner-diameter, 2-m-long stainless steel tube was fixed on a vertical unistrut channel by five adjustable rod-end bearings. By carefully adjusting the positions of these bearings we were able to secure the straightness of the tube to high accuracy. In the middle of the tube four 2.38-mm-diameter holes were drilled, equally spaced in 90° intervals. Two He-Ne green laser beams and a microscope eyepiece were employed to project the image of the hole and anode wire onto a screen from two orthogonal directions as shown on the left of Fig. 14.

The image of a 2.38-mm hole set the scale that was used to estimate the deviation of anode wire from its central location. The image of the hole and anode wire on the screen is sketched in Fig. 15. Actually the image of anode wire is a diffraction pattern, so it appears wider than its geometrical image.

A sample set of these measurements is given in Table 2. The scan was made of the anode-wire displacement as a function of voltage.

Observation shows that as the voltage is raised the anode wire experiences small but stable displacements, which go over into a large vibration at higher voltage. For practical purposes that latter conditions are unstable, and their onset defines the maximum operating voltage of the chamber.

The instability is aggravated if the anode wire is not concentric with the cathode tube. Here we extend that model of the instability to include this effect.

The capacitance per unit length of the straw-tube chamber as two cylinders not necessarily concentric is[17]

$$C = 2\pi\epsilon_0 \left[\cosh^{-1}\left(\frac{R_c^2 + R_a^2 - D^2}{2R_cR_a}\right)\right]^{-1}.$$

The definitions of R_a, R_c, and the anode-wire displacement D are illustrated in Fig. 16.

When voltage V is applied between the cylinders the potential energy is

$$W = \frac{1}{2}CV^2.$$

The electric force F_E between anode wire and cathode can be derived by differentiating W with respect to D:

$$F_E = \frac{2\pi\epsilon_0 V^2}{R_c^2(\ln(R_c/R_a))^2} D \equiv KD = K(D_{\text{tube}} - D_{\text{wire}}), \tag{14}$$

where D denotes the total deviation of the anode wire and tube from perfectly symmetrical geometry; in more detail, D_{wire} is the deviation of the wire from straightness, and D_{tube} is the displacement of the center of the tube from the ideal straight-line of the anode wire.

On the other hand, the restoring force F_T at the midpoint of the anode wire of length L is

$$F_T = T\frac{d^2 D_{wire}}{dx^2},$$

where x is the coordinate along wire. For static equilibrium the transverse electrostatic force is balanced by that due to the wire tension:

$$F_T + F_E = 0,$$

Table 2: A sample of wire instability measurements.

T (gm)	D_t (mm)	V (V)	Measured displacement of anode wire D_w (in D_t unit)	V_0 (V)	V/V_0
10	0.045	779	0.5	1156	0.674
		918	1.0		0.794
		974	1.5		0.843
		1013	2.0		0.876
		1030	2.5		0.891
		1048	3.0		0.907
		1058	3.5		0.915
		1065	4.0		0.921
		1070	4.5		0.926
		1074	5.0		0.929
		1076	5.5		0.931
		1078	6.0		0.933
			unstable		
30	0.045	1349	0.5	2002	0.674
		1589	1.0		0.794
		1692	1.5		0.845
		1747	2.0		0.873
		1781	2.5		0.890
		1813	3.0		0.906
		1829	3.5		0.914
		1842	4.0		0.920
		1850	4.5		0.924
		1856	5.0		0.927
		1861	5.5		0.930
		1863	6.0		0.936
			unstable		

All data in Table 2 were taken with $R_a = 0.0127$ mm.

$$T\frac{d^2 D_{wire}}{dx^2} + K D_{wire} = K D_{tube}. \tag{15}$$

The coordinate system used in eq. (15) is shown in Fig. 17. The solution of this equation depends on the knowledge of D_{tube}. With either of the two simple assumptions: (1) $D_{tube} = D_t = \text{const}$, or (2) $D_{tube} = D_t \sin(\pi x/L)$, one can readily solve the equation yielding:

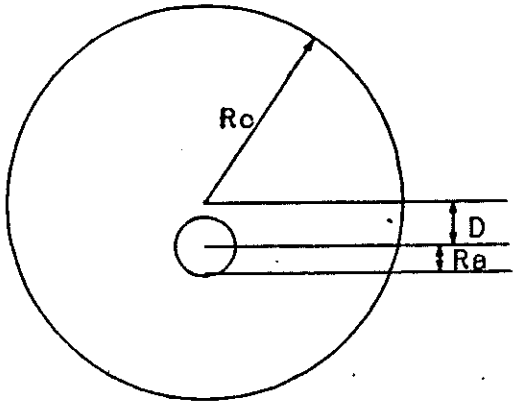

Figure 16: Geometry of an anode wire offset by distance D from the center of the cathode cylinder of a straw-tube chamber.

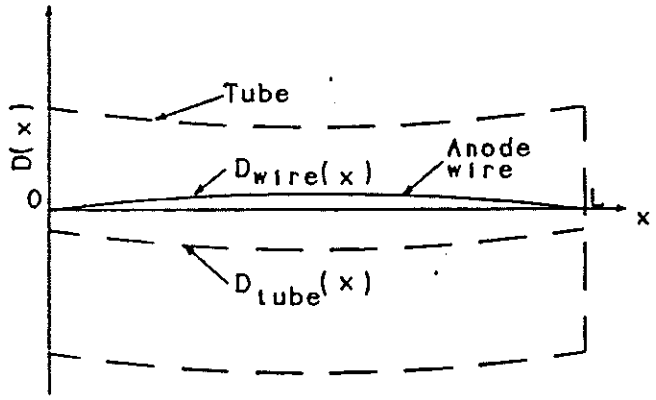

Figure 17: Coordinate system used in eq. (15).

with assumption (1):

$$D_{wire} = D_t \left\{ 1 - \frac{1-\cos(\alpha\pi)}{\sin(\alpha\pi)} \sin(\alpha\theta) - \cos(\alpha\theta) \right\}, \tag{16}$$

with assumption (2):

$$D_{wire} = D_t \frac{\alpha^2}{\alpha^2 - 1} \sin(\theta), \tag{17}$$

where $\alpha = \sqrt{K/T}L/\pi$, and $\theta = \pi x/L$. Recalling the definitions of V_0 from eq. (13) and of K from eq. (14), it follows that

$$\alpha = V/V_0.$$

The general behavier of these solutions and of our measured data points are shown in Fig. 18. In the figure $D_w = D_{wire}(x = L/2)$. The measurements were performed for five

different cases: $R_a = 0.0102$ mm with $T = 10$, 20, and 30 g, and $R_a = 0.0127$ mm with $T = 10$, and 30 g. At the highest value of V/V_0 in each data set the anode wire was starting to vibrate.

By adjusting the position of the middle rod-end bearing we established different offsets $D_t$between the tube and ideal path of the wire, which are indicated in Fig. 18. All of the data points lie between theoretical curve (3) on Fig. 18,

$$D_w/D_t = \alpha^2/(\alpha^2 - 1)\sin(\pi/2),$$

and the half value of this theoretical curve. We attribute this discrepancy to the simplified theoretical assumption of D_{wire}.

Given that a small lack of straightness, D_{tube}, is inevitable we expect that the anode wire will be deflected from its initial position as the voltage rises. After carefully adjusting the rod-end bearings, we have achieved 98% of theoretical maximum voltage V_0, confirming eq. (13).

In Fig. 19 we plot V/V_0 *vs.* $D_{total} = D_w - D_t$ for those data points which had reached highest V before the anode wire started vibrating (denoted as V_c). A linear line fits these data rather well. Since the starting points of vibration are close to curve (2) of Fig. 18, we may use eq. (17) to relate D_w/D_t and α for these data points. Combining the fitted line of Fig. 19 with eq. (17) at $\theta = \pi/2$, we obtain D_t *vs.* V_c/V_0 as

$$D_t = \left(\frac{V_c}{V_0} + 1\right)\left(\frac{V_c}{V_0} - 1\right)^2 \Big/ 0.1248. \tag{18}$$

Fig. 20 shows this function as well as our data points. The data follows the curve very well.

We anticipate that the general expression for maximum distortion of a tube, D_t as a functinon of $\alpha_c(\equiv V_c/V_0)$, will include a linear dependence on the tube radius R_c. Then we may use the form of (18) to infer that

$$\frac{D_t}{R_c} = \left(\frac{V_c}{V_0} + 1\right)\left(\frac{V_c}{V_0} - 1\right)^2 \Big/ 0.3962. \tag{19}$$

The correctness of eq. (19) remains to be checked with different size of tubes, since it is deduced from our data with only one size of the tube. It remains that the physical mechanism underlying the onset of the vibration of the anode wire is still not clear.

Equation (17) also explains the experimental observations recently reported by Blockus *et al.*[18]

Conclusions:

1. V_0 is an upper-limit high voltage for operating a straw tube chamber. We have achieved 98% of this upper-limit value.

2. For designing a straw-tube system, eq. (18), (19), and the curves (2) and (3) in Fig. 18 may be used as the basic guideline to insure the electrostatic stability of the system.

3. Any defect of roundness and straightness (including gravitational bending) of the straw tube itself will greatly affect the stability, as indicated by Fig. 20.

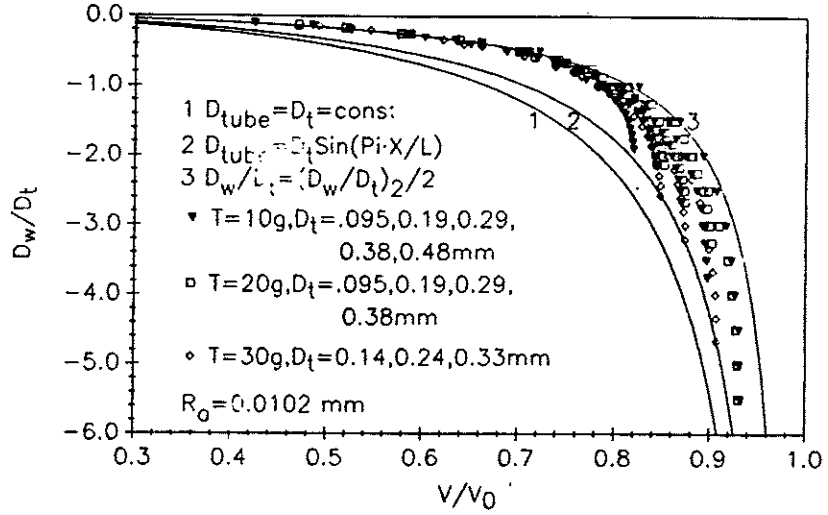

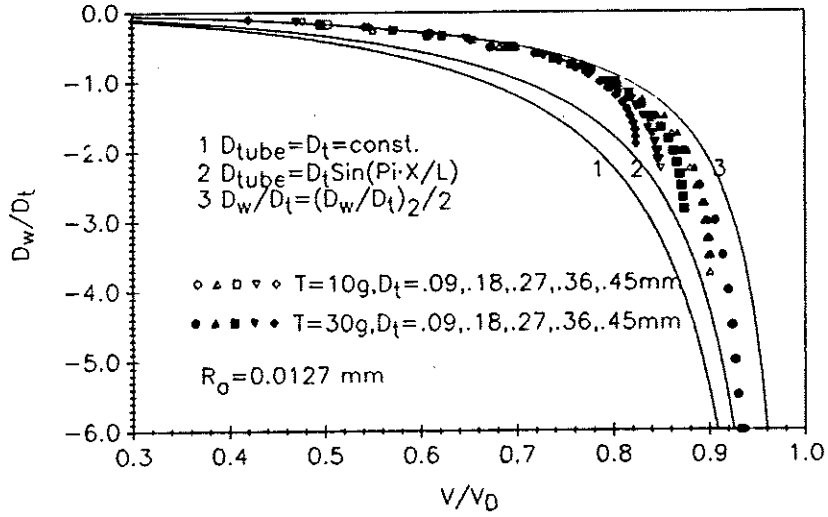

Figure 18: (a). D_w/D_t *vs.* V/V_0 for $R_a = 0.0102$ mm. (b). D_w/D_t *vs.* V/V_0 for $R_a = 0.0127$ mm.

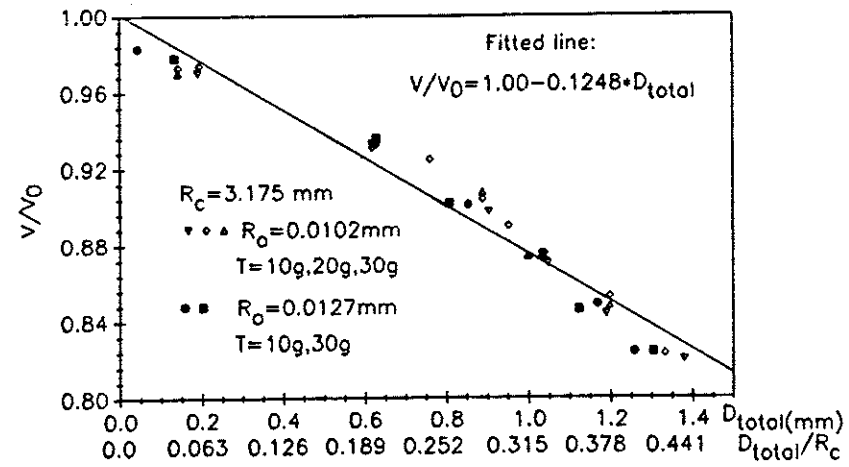

Figure 19: V_c/V_0 *vs.* D_{total} for five different cases.

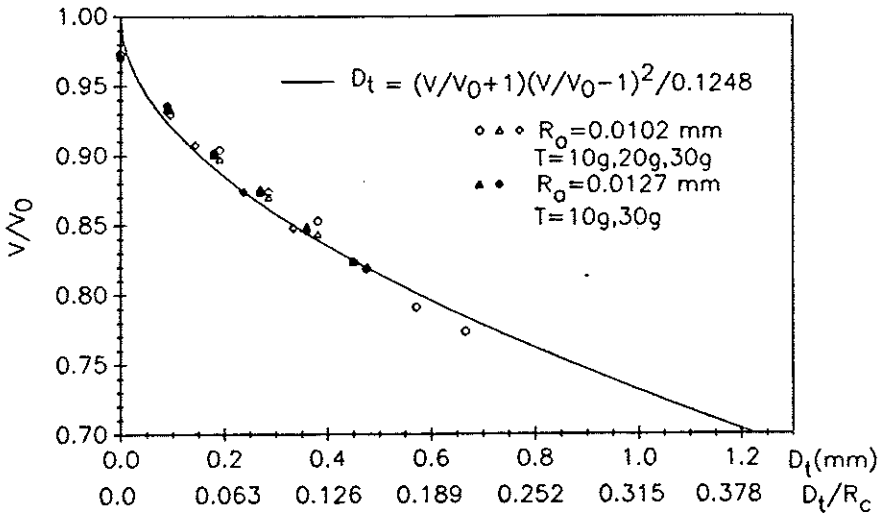

Figure 20: V_c/V_0 *vs.* D_t for five different cases.

23 Effect of Mechanical Deviation on the Gas Gain

In a realistic straw-tube chamber there is always certain amount of mechanical deviation from the ideal symmetrical geometry. Therefore a gas-gain model, for example Diethorn's formula refeq1), should be modified as follows:

$$\ln G = \frac{V}{\cosh^{-1}(y)} \frac{\ln 2}{\Delta V} \left(\ln \frac{V}{P R_a \cosh^{-1}(y)} - \ln K \right),$$

where $y = (R_a^2 + R_c^2 - D^2)/2R_aR_c$, and D is the total displacement of the wire from the tube axis.

Figure 21 shows the calculated curves of $\ln G$ *vs.* D for three different sizes of anode wire. It is evident that the thicker wire is more sensitive to mechanical deviation. In the case of $D = 0.5$ mm, the gas gain increases will be 5.6%, 8.3% and 11% for $R_a = 0.01$ mm, 0.02 mm and 0.03 mm, respectively.

24 Choice of the Wire Size — Thick or Thin?

The choice of the wire size is a compromise among various considerations. We summarize some of them in Table 3.

Some supporting remarks:

- Gravitational sagitta – For a tungsten anode wire of L (cm) in length, R_a (cm) in radius, under tension T (gm) and mounted horizontally, the sagitta is

  $$s = 7.58 L^2 R_a^2 / T,$$

  while the maximum practical tension varies at $T \propto R_a^2$ due the the breaking strength of the wire.

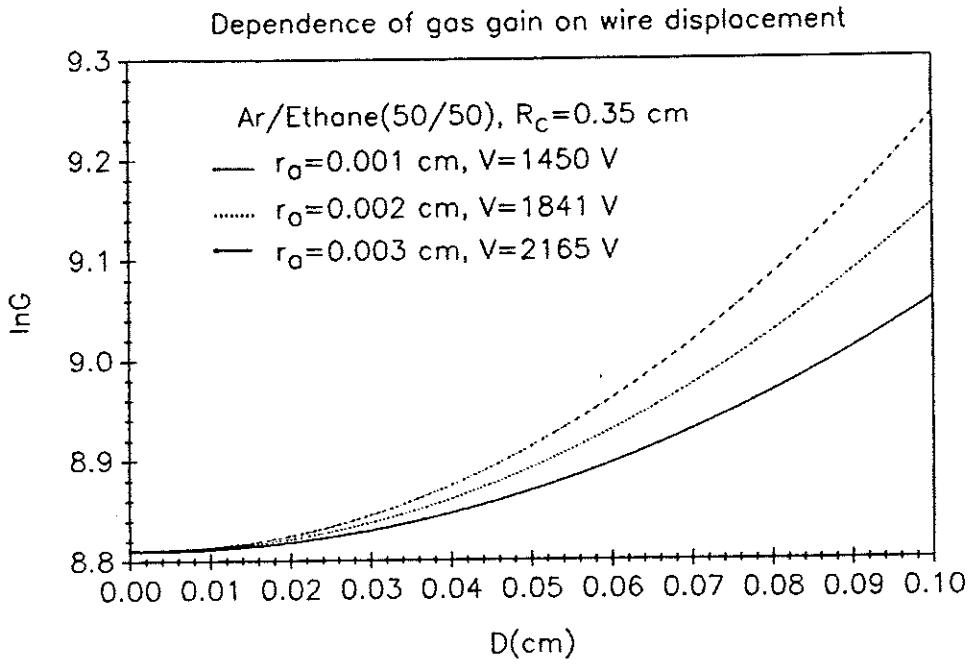

Figure 21: Calculated effect of a displacement D of the anode wire on the gas gain.

- Mechanical deviation – see Fig. 16.
- Temperature dependence – see Figs. 11, 12, and 13.
- Electrostatic stability – Eq. (13) indicates that $V_0 \propto \sqrt{T}\ln(R_C/R_A)$, while $T \propto R_a^2$, so $V_0 \propto R_a \ln(R_c/R_a)$. On the other hand, the dependence of the gas gain on the wire radius is much slower than this, as shown by Diethorn's formula (1).
- Buckling – The higher tension in a thicker anode wire aggravates the buckling problem.

25 An Example Parameter List of a Straw-Tube System

Since an Ar/Ethane (50/50) mixture has been used in the AMY vertex and inner-tracking chambers, and also was tested by MAC vertex-detector group, it is one of the best-understood gas mixtures for straw-tube chambers. We use the gas parameters of this mixture as found above to make a sample design of a straw-tube system.

We set the geometry of straw-tube chamber as

$$R_a = 0.00102 \text{ cm}, \qquad R_c = 0.35 \text{ cm}, \qquad L = 200 \text{ cm}.$$

In this example, the straw is mounted horizontally.

Table 3: Pros and cons of thick and thin wires.

Effect	Thick wire	Thin wire
Gravitational sagitta	same	same
Effect of mechanical deviation on gain	worse	better
Temperature dependence	worse	better
Electrostatic stability	better	worse
Buckling	worse	better

We use Aoyama's formula (2) for gas-gain calculations, with the parameters $A = 0.1141 \times 10^{-6}$, $m = 0.4942$, $V_I = 12.86$ V; see Fig. 9.

If we want to operate our chamber at $G \approx 2.5 \times 10^4$, the high voltage should be set at $V = 1550$ V.

From Fig. 13(c) we find $(dG/G)/(dT/T) \approx 4.9$ under the present circumstances.

If we set tension $T = 40$ gm, the gravitational sagitta will be 75 μm, and the critical high voltage is $V_0 = 2696$ V, yielding $V/V_0 = 57.5\%$.

According to eq. (17) the wire displacement D_w caused by electric field will be

$$D_w = \left[\left(\frac{V_0}{V}\right)^2 - 1\right]^{-1} \times 75\ \mu\text{m} = 37\ \mu\text{m}.$$

Therefore the total displacement of the anode wire from the tube center is

$$D_{total} = 75 + 37 = 112\ \mu\text{m}.$$

This displacement will cause negligible variation of the gas gain, but will require a large correction to the position measurement.

Now we switch to a fat wire, $R_a = 0.0254$ mm. If we still desire $G = 2.5 \times 10^4$, the high voltage should be set at $V \approx 1960$ V.

A tension of 40 gm for $R_a = 0.0102$-mm wire scales up to $T = 250$ gm at $R_a = 0.0254$ mm. It follows that

$$V_0 = 5684\ \text{V},$$

$$V/V_0 = 34.4\%,$$

$$D_w = \left[\left(\frac{V_0}{V}\right)^2 - 1\right]^{-1} \times 75\ \mu\text{m} = 10\ \mu\text{m}.$$

Using Aoyama's formula (2) we can predict

$$\frac{dG/G}{dT/T} \approx 0.7 \times 9.5 = 6.6.$$

The spatial resolution attainable with Ar/Ethane (50/50) at 1 atm. is only about 120 μm according to the measurements of MAC group[14] and AMY group[8,15]. In order to improve the spatial resolution high gas pressure could be used. If we run our chamber at 3 atm, the calculated results are summarized in Table 4. Note that a thin anode wire is not indicated at high pressure because the higher voltage required there renders the tube susceptible to the electrostatic instability.

Table 4: Summary of the design exercise.

R_a (mm)	0.0102	0.0254	0.0102	0.0254
Gas pressure (atm)	1	1	3	3
Tension T (gm)	40	250	40	250
Gain G ($\times 10^4$)	2.5	2.5	2.5	2.5
V (V)	1550	1960	2550	3450
V_0 (V)	2696	5684	2696	5684
V/V_0 (%)	58	34	95	60
$D_w^{\rm grav}$ (μm)	75	75	75	75
D_w^E (μm)	37	10	694	42
$D^{\rm Total}$ (μm)	112	85	769	117
$(dG/G)/(dT/T)$	4.9	6.6	6.8	9.2

26 Remarks on the Studies of Gas Gain and Wire Stability

1. The gas-gain models of Diethorn, Aoyama, and of Kowalski fit our experimental data (at a fixed temperature) rather well.

2. Experimental measurements have been made of the temperature dependence of the gas gain. The gas-gain formulae indicate the general behaviour of this dependence, but there is a substantial numerical disparity between data and the models, and the model values should be used only as an upper-limit estimate of temperature effects.

3. The critical voltage V_0 of eq. (17) is a theoretical upper-limit value for stable operation of a straw-tube chamber: 98% of this value could be reached, but for a large straw-tube system, operation at 75% of V_0 may be a more realistic number. Equations (17) and (18) indicate the requirements on straightness of the tube.

27 Timing Studies with Single Electrons

27.1 Experimental Set-up

UV light sources have been used to generate photoelectrons from photosensitive plates for time-of-flight measurement of electrons in different gases.[21, 22] Also, several papers report on the use of laser-induced ionization in drift chambers to mimic the track of a minimum-ionizing particle.[23, 24, 25, 26] We have developed a technique to study single photoelectrons ejected from the wall of a straw-tube chamber by a N_2 laser. Measurements of the drift time and of avalanche size have been made. In this section we concentrate on timing measurements.

A sketch of the experimental set-up is shown in Fig. 22. Figure 23 gives details of the test chamber that permits both a laser beam and an Fe^{55} source to be used to generate the primary electrons

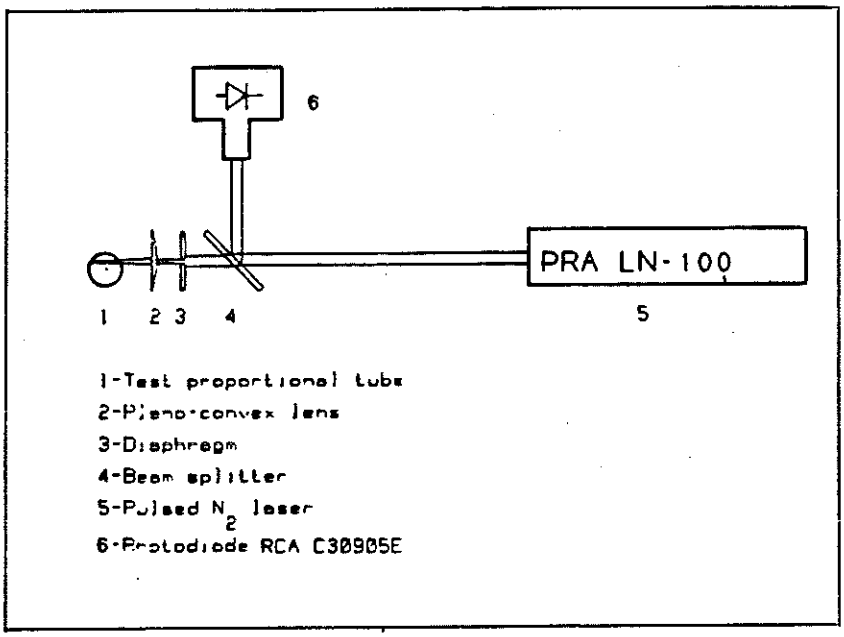

Figure 22: Sketch of the experimental set-up.

The N_2 laser generates pulsed 337-nm (3.67-eV) UV photons, with a pulse length of about 350 ps. The pulse energy is about 50 μJ, corresponding to about 10^{14} photons. The test drift tube was made of 7.67-mm-diameter aluminum tubing.

The photoelectric work function of aluminum is 4.08 eV, which is larger than laser-beam energy; therefore the quantum efficiency for producing the photoelectron from the wall is expected to be very small. But due to the large number of photons per pulse we still can get enough photoelectrons. We are most interested in single-photoelectron events, so we use an iris diaphragm to reduce the beam intensity.

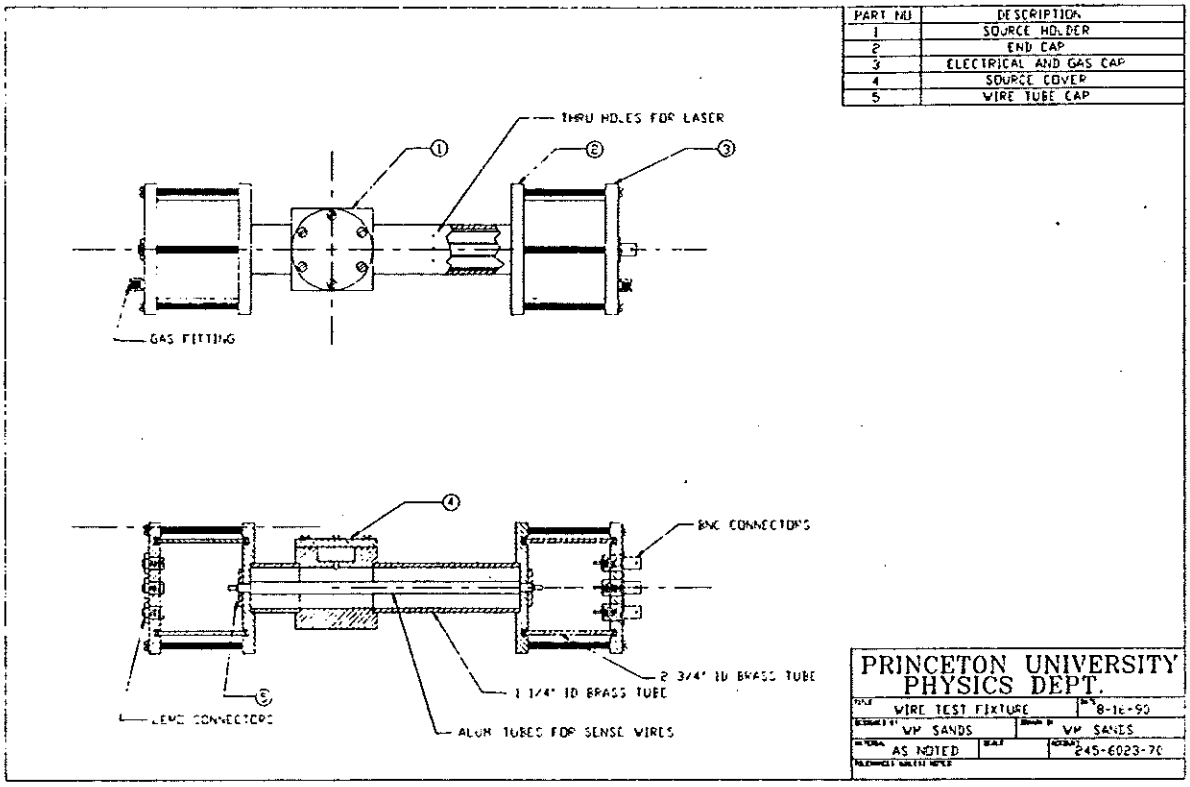

Figure 23: Details of the test chamber.

The laser beam was focused onto the inner wall of aluminum tube after passing through a 1-mm-diameter hole in the wall. The hole is offset by 1 mm from the center line of the tube. Because the beam spot on the inner surface of the tube is quite small, we can neglect mechanical imperfections and consider that the drift distance of the photoelectrons was just the radius of the tube. A beam splitter was used to reflect part of the laser beam to a photodiode (RCA C30905E), which generates a fast, large electric pulse as a start signal for TDC system. A preamplifier was directly connected to the test drift tube through a high-voltage capacitor. The drift-tube signal was used as a stop signal. The electronic block diagram is shown in Fig. 24.

Two different preamplifiers have been used in our measurements: a LeCroy TRA402 and U. Penn/AT&T preamplifier. The U. Penn preamplifier was used for studying the performance of CF_4/Ar and CF_4/isobutane mixtures with different mixing ratios. The other gas mixtures were measured by LeCroy preamplifier.

The sensitivity and noise performance of these two preamplifiers have been measured, as shown in Fig. 25. The sensitivity measurement was carried out by charging a small capacitor with an EG&G ORTEC 419 precision pulser. After this known charge was amplified by the preamplifier, we measured the amplitude of the output signal on a HP 54502A digital oscilloscope. The noise *vs.* input capacitance was measured by attaching various BNC connectors (regarded here as capacitors) to the input of preamplifier and reading the $V_{\rm rms}$ value on the digital scope. The capacitances of these BNC connectors were then measured with a HP 4815A RF vector impedance meter at 100-MHz frequency.

Under our experimental conditions the U. Penn preamplifier appears to be 5 times more sensitive than the LeCroy TRA402. The typical E.N.C. (equivalent noise charge) at 10-pF

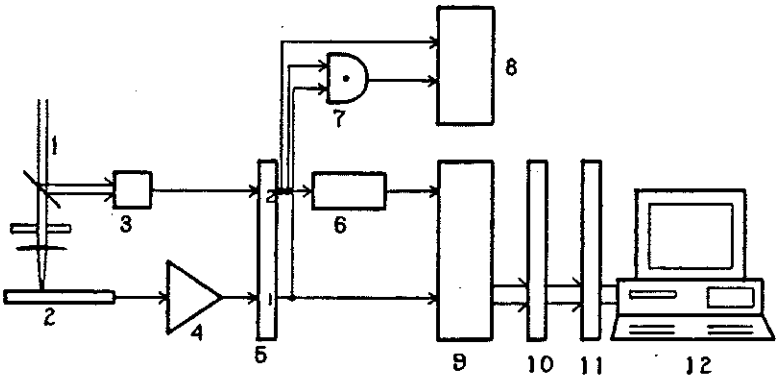

1 - Laser beam
2 - Test tube
3 - Photodiode.RCA C30905E
4 - LeCroy TRA-402 preamp or AT&T preamp.
5 - Discriminator.ORTEC934
6 - Delay box
7 - Logic unit LeCroy 365AL
8 - Scaler.LeCroy 4604
9 - LeCroy QVT 3001
10- QVT-CAMAC interface 2301
11- Crate controller 6002
12- PC computer

Figure 24: Block diagram of the electronics.

input capacitance is about 1600 electrons for the U. Penn preamplifier, and 17000 electrons for the LeCroy TRA402. When a 2-meter-long, well-shielded straw tube (7 mm in diameter, 25-μm anode wire) was attached to the U. Penn preamplifier, the E.N.C. was about 2000 electrons.

The threshold of the discriminator following the preamplifier was set at 30 mV (into 50 ohms), so the gas gain of a single-electron avalanche had to be greater than 5×10^4 (U. Penn) and 2.6×10^5 (LeCroy TRA402), respectively.

27.2 Gas Control System

To blend different gas mixtures and to adjust the gas pressure with high precision, a bench-top gas system was installed, as shown in Fig. 26.

The accuracy of the mass-flow controllers is 2% of reading and the accuracy of pressure transducer is 0.15% of reading (according to the manufacturers' specifications, Vacuum General, and Edwards High Vacuum, respectively). The fluctuation of the pressure under control has been within ± 1 Torr around the set point.

The piping of whole system was made of copper tubing. An oxygen filter and a moisture filter were installed directly in front of the test prototype. According to the manufacturer's specification (Chrompak) the Gas-Clean oxygen filter removes oxygen, traces of sulphur and chlorine compounds from the gas, and concentration of oxygen is brought down to less than 1 ppm. The moisture filter removes water, oil, and other foreign material. A short branch in parallel with these filters allows gas flush path.

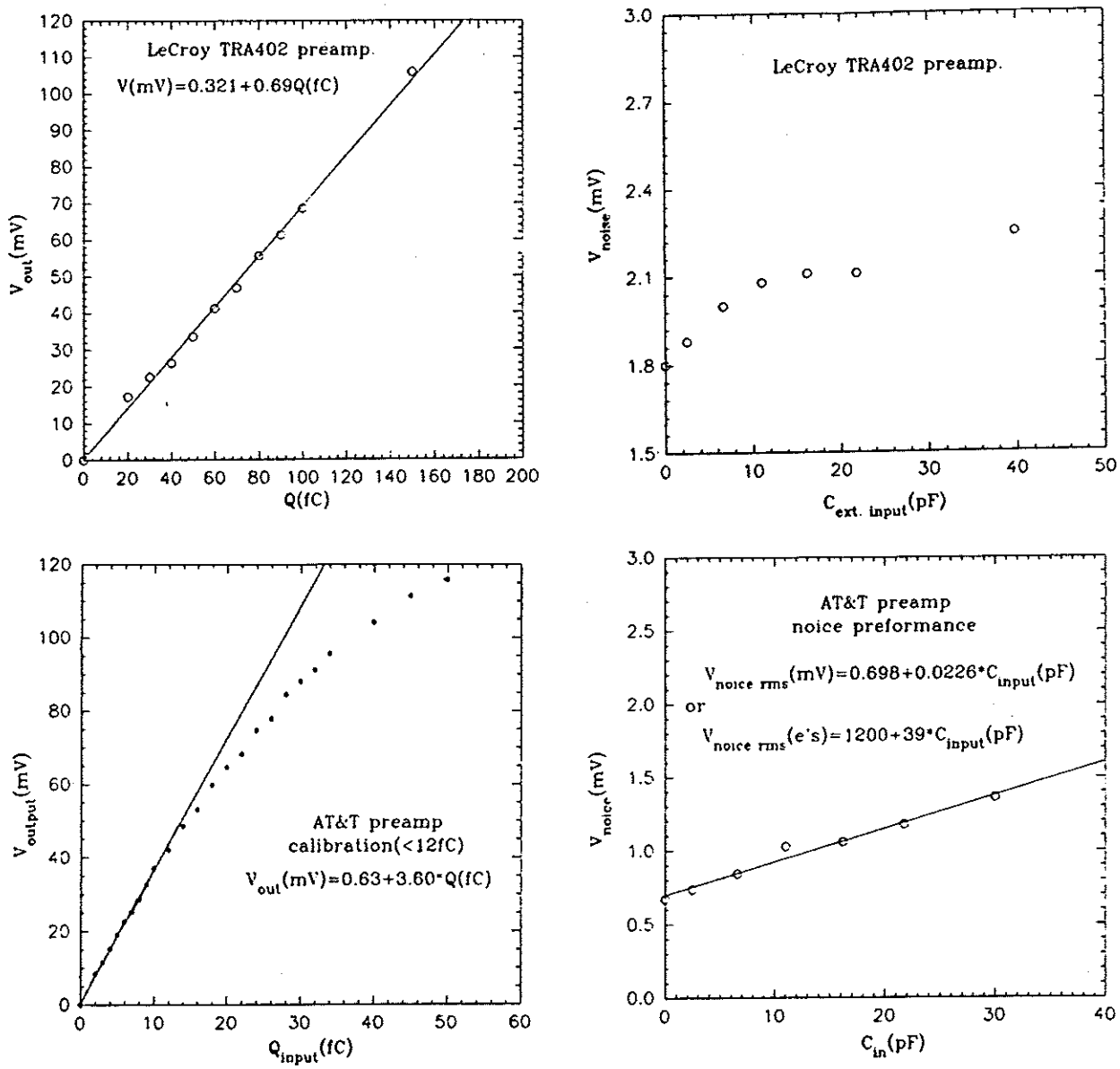

Figure 25: (a). Sensitivity and noise performance of a LeCroy TRA402 preamplifier. (b). Sensitivity and noise performance of the U. Penn/AT&T preamplifier.

Two manual needle valves were added in parallel with mass-flow valve and pressure control valve for speeding up the procedure of setting different gas pressures.

27.3 Time Spectra

Several gas mixtures have been tested with this setup.

Due to the very small quantum efficiency and large number of primary UV photons, the number of photoelectrons in each pulse should vary according to a Poisson distribution. We reduced the aperture of the iris diaphragm until at most 1 in 4 laser pulses yielded any photoelectrons, and hence at least 90% of recorded events were initiated by single photoelectrons.

Some typical multi-photoelectron events are shown in Fig. 27 as recorded by a digital

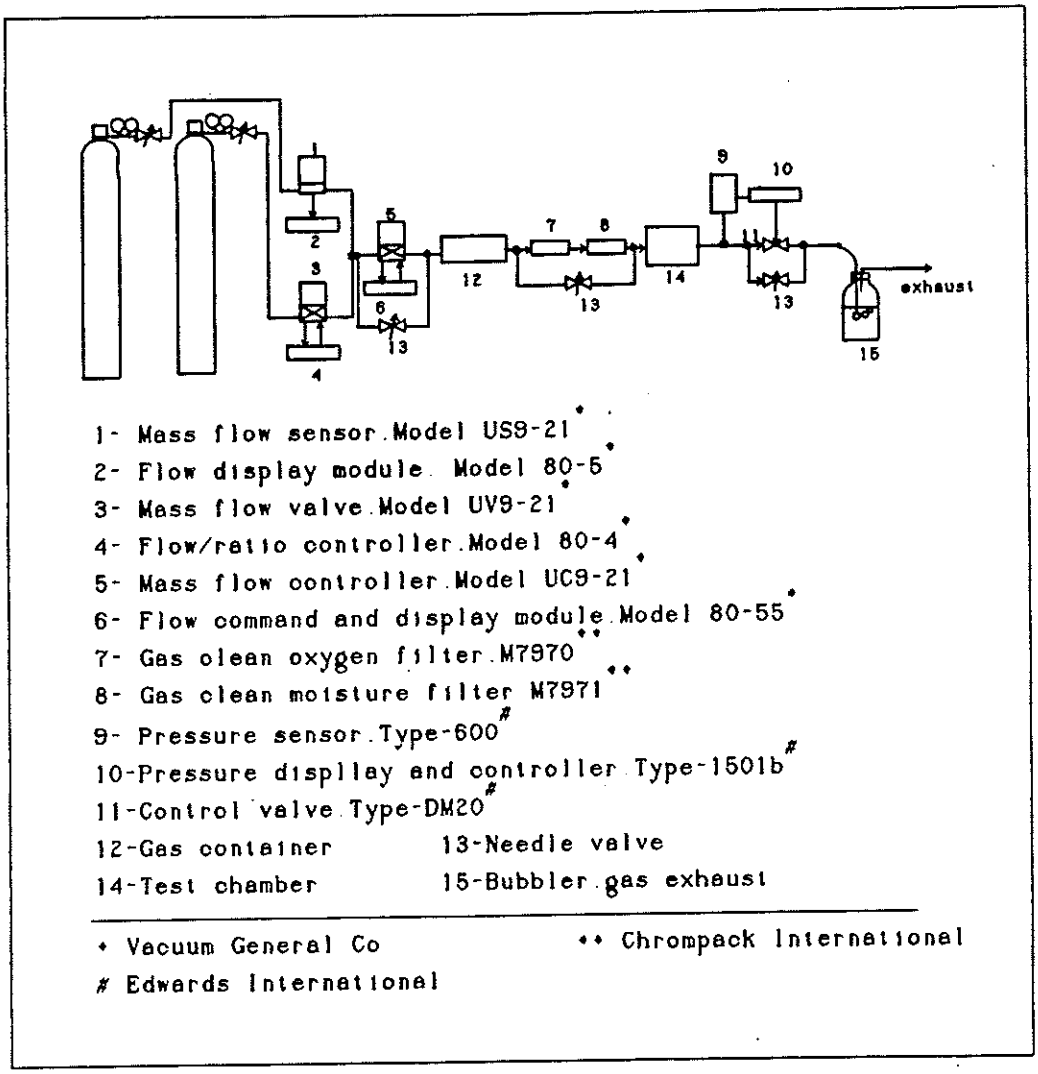

Figure 26: The gas control system.

oscilloscope. The chamber was under constant gas pressure and high voltage for a P-10 gas mixture, but note the different time and voltage scales. The time jitter of the signal's leading edge can be clearly seen. Figure 27(c) also shows the after-pulses which are due to photoelectrons released from tube's wall by the UV photons of the gas avalanche itself. The time difference between original pulses and after-pulse is just equal to the drift time for the entire radius. Figure 28 shows single-photoelectron events, for which fluctuations in the gas avalanche are large.

The measured time spectra along with Gaussian fits are shown in Fig. 29. The fits are very satisfactory.

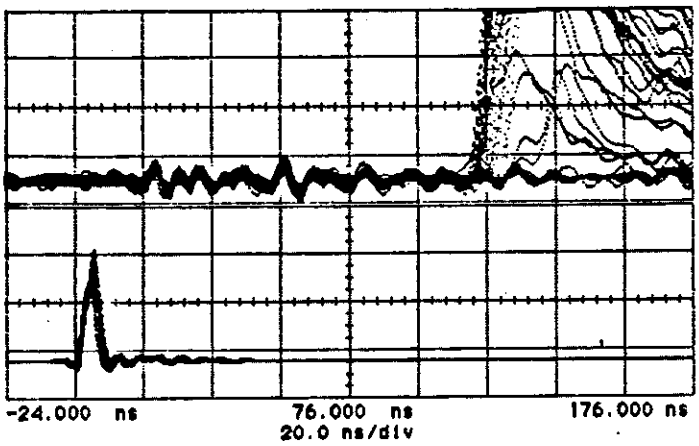

(a)

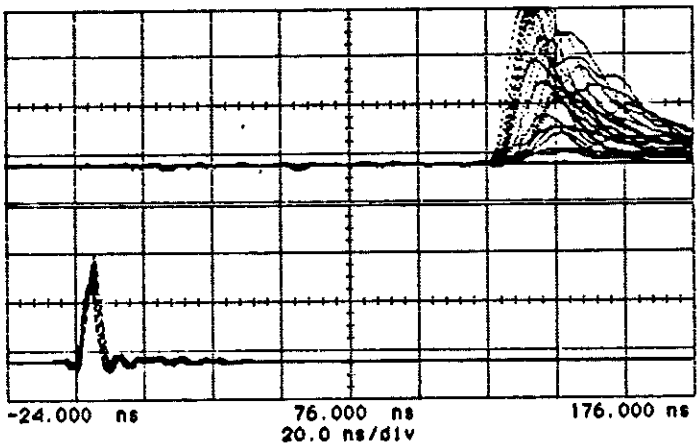

(b)

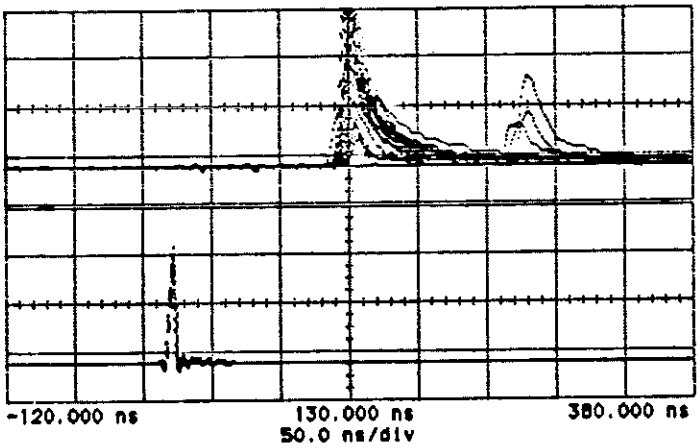

(c)

Figure 27: Photodiode and drift-tube signals for multi-electron events. P-10 mixture, $P = 760$ torr, $V = 1600$ V. The upper trace shows the drift-tube signals, the lower shows the photodiode signals. (a) Vertical scale of upper trace is 40 mV/div; (b), (c) vertical scale of the upper trace is 400 mV/div; notice the different time scales.

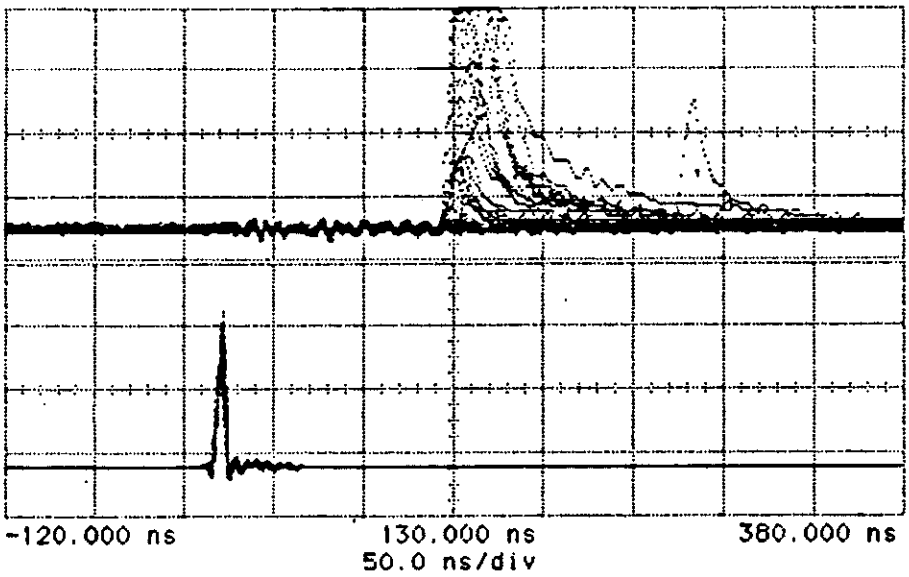

Figure 28: Photodiode and drift-tube signals for single-photoelectron events. P-10 mixture, $P = 760$ torr, $V = 1600$ V. The upper trace shows the drift-tube signals, the lower shows the photodiode signals. The vertical scale of upper trace is 100 mV/div.

27.4 Drift Time

Based on energy conservation, the following equation holds,[27]

$$eEw = \langle \Lambda \epsilon v / \ell_e \rangle \tag{20}$$

where E is the electric field, w is the drift velocity, ϵ is the kinetic energy, $\Lambda(\epsilon)$ is the mean fractional energy loss in a collision, v the random electron velocity, and $\ell_e(v)$ the mean free path for collision of the electron with the gas molecules. The left side represents the energy gained between collisions, and the right side is the energy lost in atomic collisions. Assuming ℓ_e is independent of v and the distribution of electron energy is narrow, and taking into account the following equations,

$$w = \frac{2}{3}\frac{eE}{m}\left\langle \frac{\ell_e(v)}{v} \right\rangle + \frac{1}{3}\frac{eE}{m}\left\langle \frac{d\ell_e(v)}{dv} \right\rangle,$$

$$\epsilon = \frac{1}{2}mv^2,$$

it follows that

$$w \simeq \sqrt{\frac{2}{3}\sqrt{\frac{1}{3}}\Lambda\frac{eE\ell_e}{m}}. \tag{21}$$

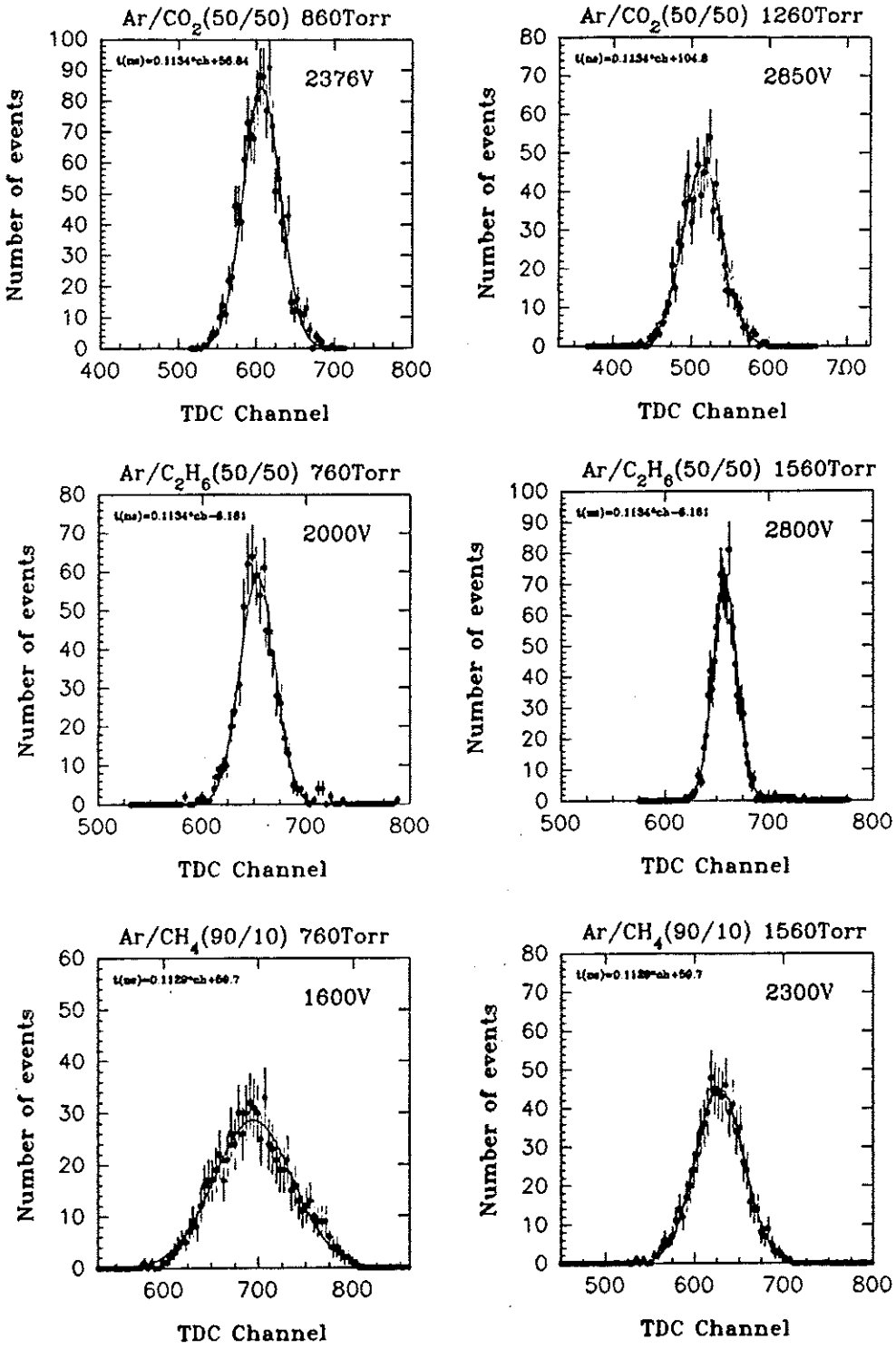

Figure 29: (a) Drift-time spectrum for Ar/CO_2 (50/50). (b) Drift-time spectrum for Ar/C_2H_6 (50/50). (c) Drift-time spectrum for Ar/CH_4 (90/10).

Since ℓ_e is inversely proportional to gas pressure P,

$$\ell_e = \ell_{e0}/P,$$

where ℓ_{e0} is ℓ_e at 1 atm. Therefore

$$w \simeq \sqrt{\frac{2}{3}\sqrt{\frac{1}{3}}\Lambda\frac{e\ell_{eo}}{m}}\sqrt{\frac{E}{P}}. \tag{22}$$

This is the well-known result that the drift velocity should depend only on $\langle E/P \rangle$.

Using simplified formulae to approximate the published curves on the drift velocity *vs.* E/P, we are able to calculate the total drift time. Adjusting the parameters in the formulae to get the best fit of our data, the results are shown in Fig. 30. The agreement is impressive. Because our data are collected under various pressures, and the drift velocity curves used in our fitting were measured or calculated at 1 atm, our results further confirm $w \propto f(E/P)$.

The previously reported drift velocity of Ar/C_2H_6 (50/50) is nearly constant, with a slightly downward slope. It agrees well with our drift-time data, which are nearly constant with only a very small upward slope.

27.5 Spatial Resolution

From the same argument as in previous section, it follows that[27]

$$\epsilon_k = \langle \epsilon \rangle \simeq \frac{3\ell_{eo}}{\sqrt{3\Lambda}}\frac{E}{P}, \tag{23}$$

where ϵ_k denotes the characteristic energy, which is a function of E/P. The spatial resolution σ is then

$$\sigma_x = \sqrt{\frac{2\epsilon_k x}{eE}}, \tag{24}$$

where x is the drift distance. Using (23) instead of ϵ_k in (24) we arrive at

$$\sigma_x = \sqrt{\frac{2\ell_{eo}}{\sqrt{3\Lambda}}}\sqrt{\frac{x}{P}}. \tag{25}$$

While $\Lambda(\epsilon)$ is a function of electron energy ϵ, ϵ remains at a constant value up to rather high E field for a "cool gas" such as CO_2, for which Λ remains effectively constant. In such cases we conclude from (25) that

$$\sigma_x \propto \sqrt{\frac{1}{P}}.$$

We have directly measured the value of σ_t, and converted to σ_x using the x *vs.* t curve near the tube wall. Figure 31 shows our data as well as a fit of the form

$$\sigma_x = \sigma_0 + A/\sqrt{P}$$

for Ar/CO_2. The results for Ar/CH_4 and Ar/C_2H_6 are shown in Fig. 32.

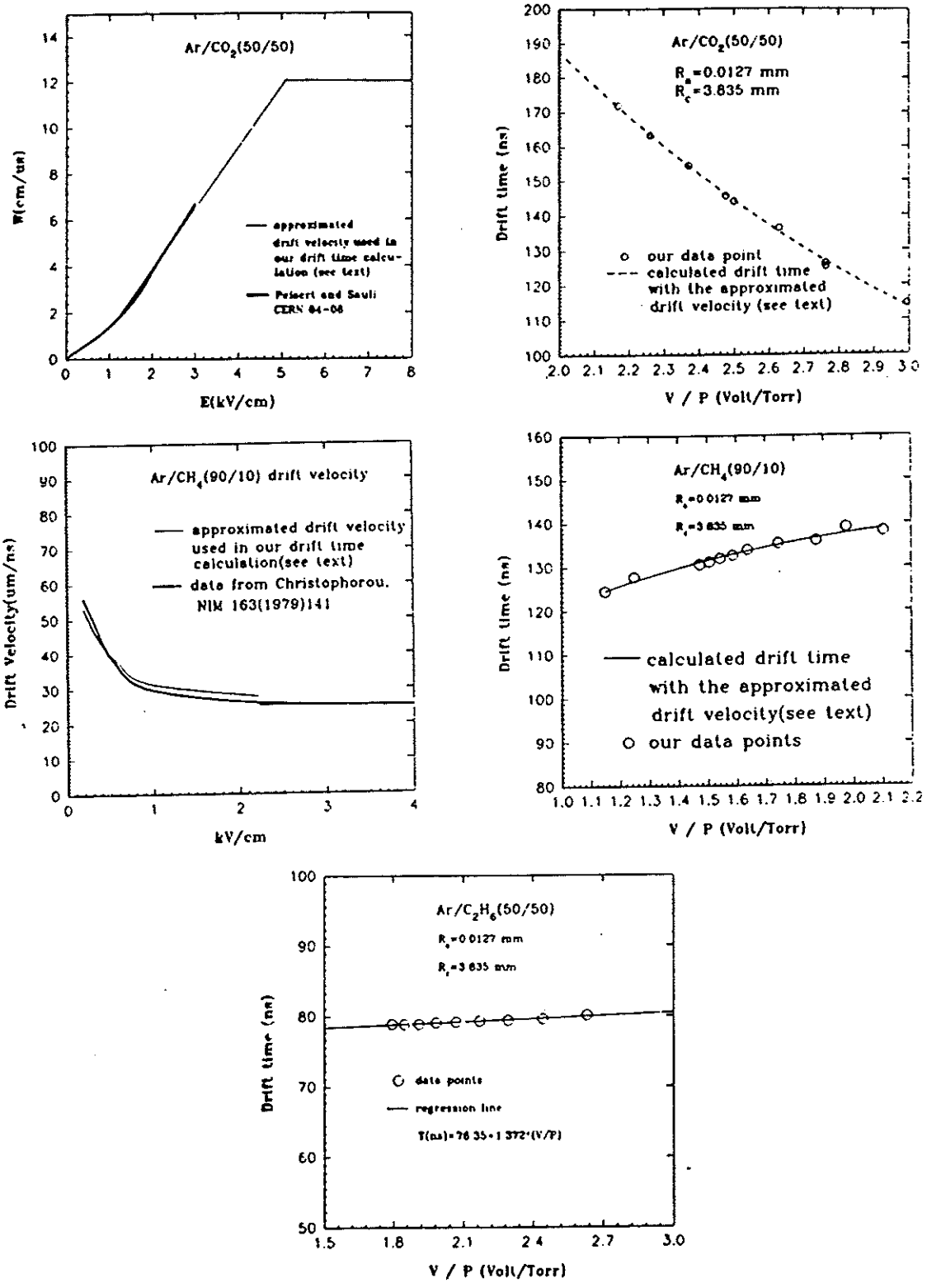

Figure 30: (a) Drift velocity and drift time of Ar/CO_2 (50/50). (b) Drift velocity and drift time of Ar/CH_4 (90/10). (c) Drift time of Ar/C_2H_6 (50/50).

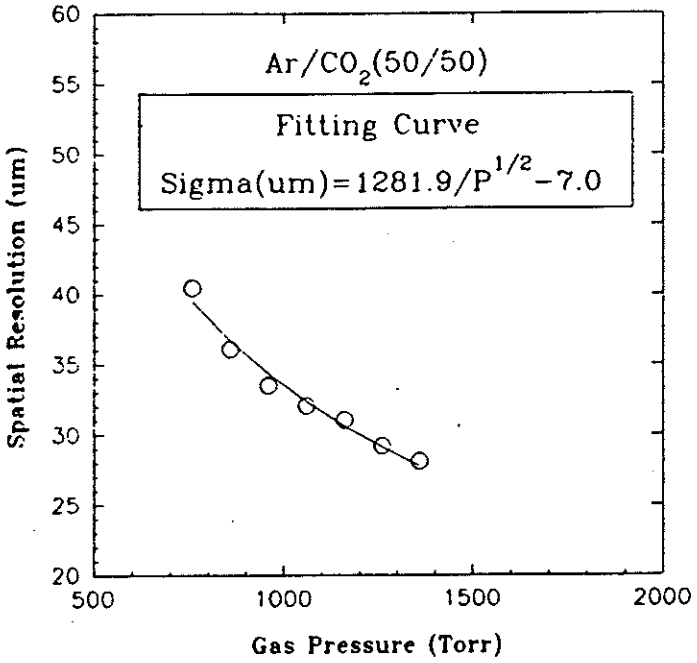

Figure 31: Spatial resolution of Ar/CO_2 (50/50).

27.6 Discussion

The total drift times over the radius of our proportional tube agree well with the published data. Direct comparison with the published data of our results on spatial resolution are difficult due to very limited existing data.

Pius[28] measured the longitudinal diffusion of electrons in $Ar/C_2H_6(50/50)$, with results shown in Fig. 33(a). Figure 33(b) shows the results of Jean-Marie *et al.*[29] We infer that $\sigma_{0l} \simeq 210\ \mu m/\sqrt{cm}$ from Pius and $\sigma_{0l} \simeq 125\ \mu m/\sqrt{cm}$ from Jean-Marie *et al.*Then for a 0.3835-cm drift distance the spatial resolutions should be 130 μm and 77 μm, respectively. Our result for 760 torr is 100 μm, in reasonable agreement.

The spatial resolution with Ar/CO_2 (50/50) is much better than with the other two gases due to its very slow drift velocity near the tube's wall, as well as its being a "cool gas." While the results for Ar/CO_2 appear insensitive to the electronic time resolution, this will not necessarily be so for signals originating close to the anode wire, noting that $x \propto \sqrt{t}$ (x distance from anode wire, t drift time), as shown in Fig. 34.[19]

27.7 Timing Performance of Gas Mixtures Containing CF_4

Being convinced by the good agreement between our measurements and published data for the three gas mixtures mentioned above, we made a further investigation for gas mixtures containing CF_4. This "fast" gas is believed to be one of the most attractive candidates for the SSC environment.[30, 31]

In this investigation the U. Penn preamplifier has been employed. The superior noise performance at high frequency of this amplifier allows us to benefit from the very narrow

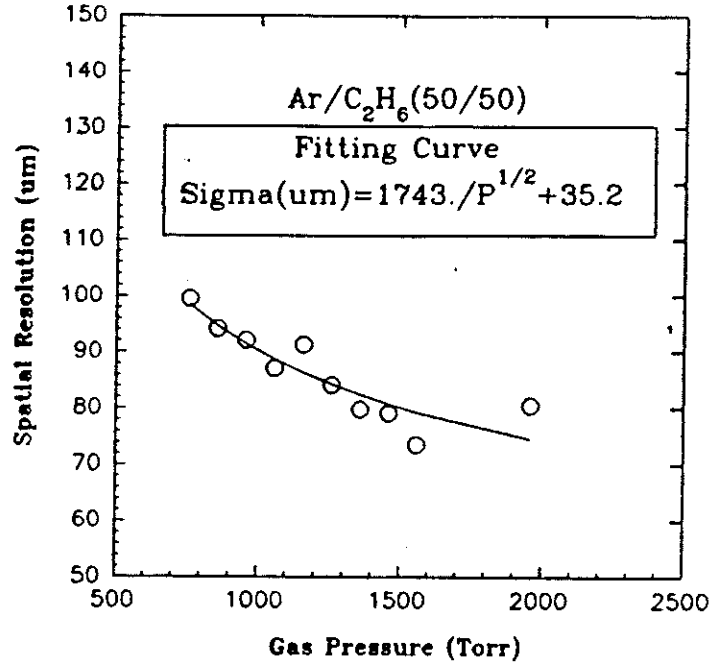

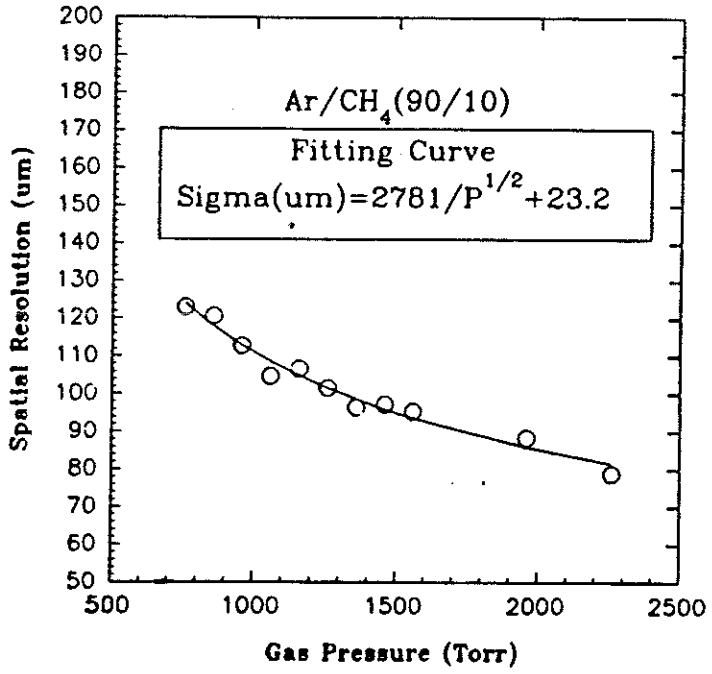

Figure 32: (a) Spatial resolution of Ar/C_2H_6 (50/50). (b) Spatial resolution of Ar/CH_4 (90/10).

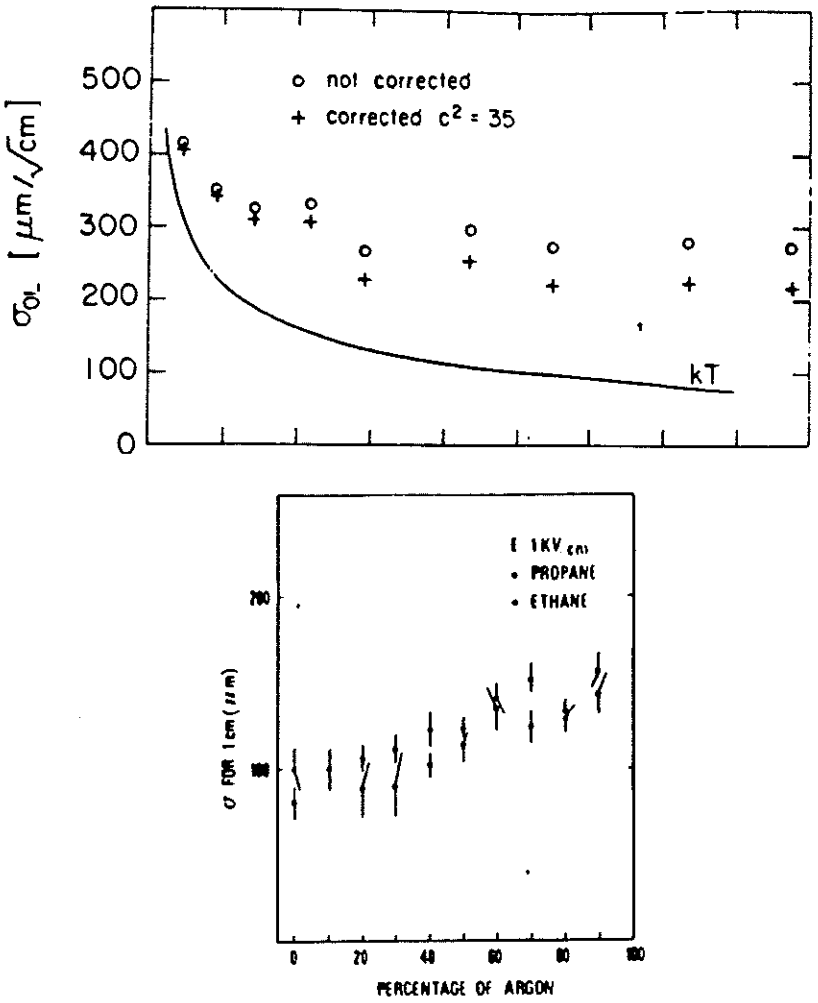

Figure 33: (a) Longitudinal diffusion of an electron in $Ar/C_2H_6(50/50)$ gas mixture, from Pius.[28] (b) Longitudinal diffusion of an electron in $Ar/C_2H_6(50/50)$ gas mixture, from Jean-Marie.[29]

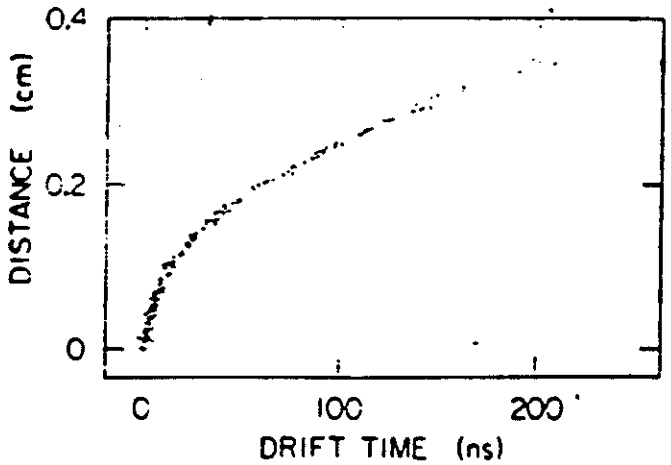

Figure 34: Time-to-distance relationship in $Ar/CO_2/CH_4$ (49.5/49.5/1.0) for a straw-tube drift chamber.[19]

time distribution obtainable using CF_4 gas mixtures.

The observed time spectra from CF_4/Ar and CF_4/isobutane are shown in Fig. 35. We summarize the drift-time results in Fig. 36.

The only available published data on the drift velocity of CF_4/isobutane (to our knowledge) are compiled in Fig. 37.[30, 32] Due to very limited E/P region of these data it is not possible to infer the total drift time from them. The general trend of drift time *vs.* percentage of CF_4 in CF_4/isobutane mixtures and drift time *vs.* V/P looks reasonable. But the peculiar twisting behaviour between Ar/CF_4 (20/80), (0/100) and the other three mixtures may need to be confirmed by further study, because the first two mixtures were measured before oxygen and moisture filters were installed. However, the dependence of the drift time on the percentage of CF_4 and V/P is insensitive for Ar/CF_4.

Figure 38 shows the time resolution with CF_4 gas mixtures. A slight improvement with increasing gas pressure can be seen. The time resolutions are in the 0.55-0.75 ns range for Ar/CF_4 mixtures, and 0.55-1.0 ns for CF_4/isobutane mixtures. Using data from Fig. 225 we can infer the spatial resolution for Ar/isobutane near the tube wall. Except for pure CF_4, all of the resolutions are 25-50 μm, as shown in Fig. 39. The big gap between pure CF_4 and the rest of gas mixtures is attributed to the big gap in the drift-velocity data compiled in Fig. 37, which we have used to convert time resolution into spatial resolution directly. Because there is no existing drift-velocity data for CF_4/isobutane (83/17), (67/33), we have adopted the (80/20), (70/30) data instead; this also tends to increase the gap artificially.

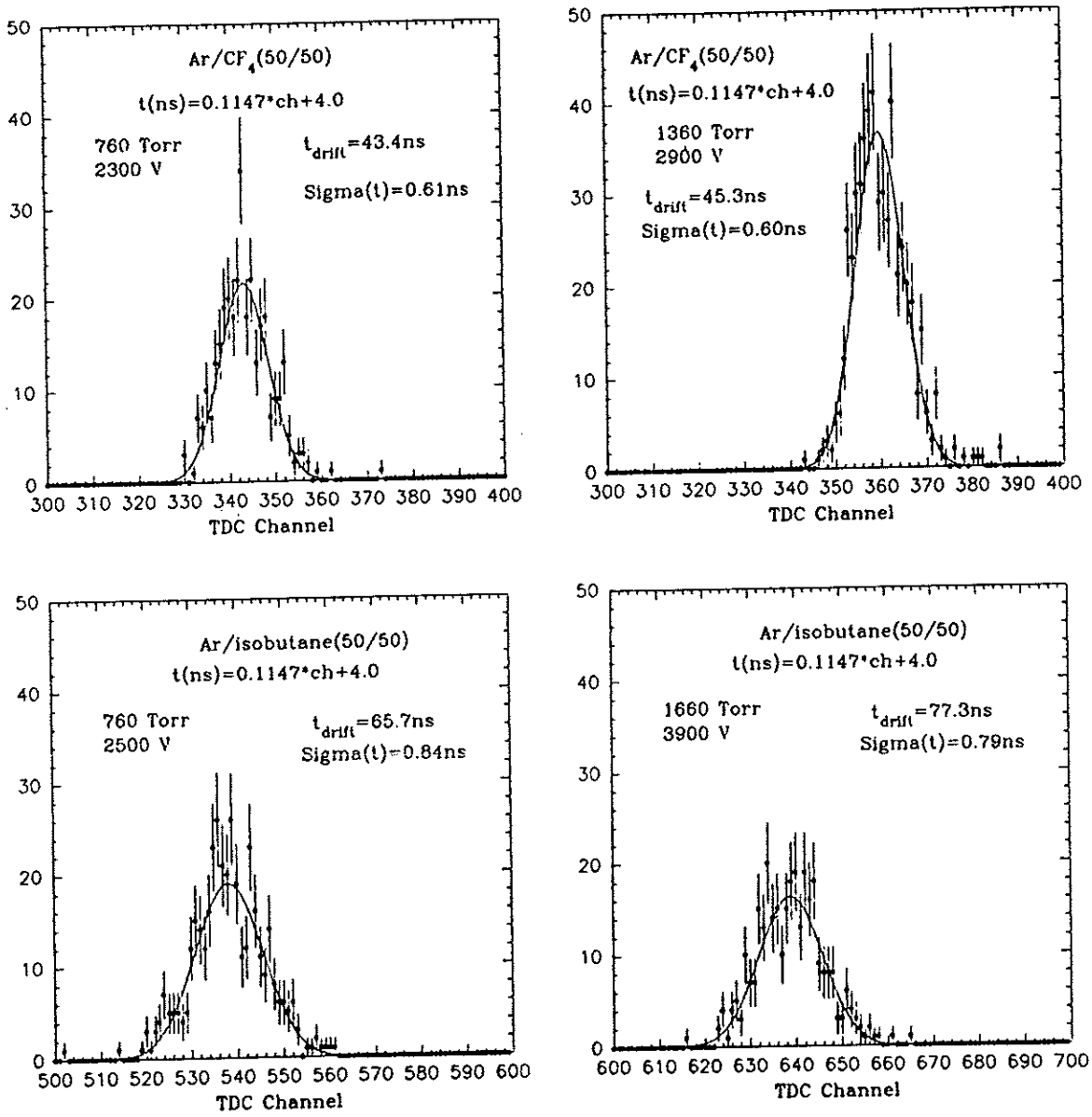

Figure 35: (a) Time distribution of CF_4/Ar (50/50). (b) Time distribution of CF_4/isobutane (50/50).

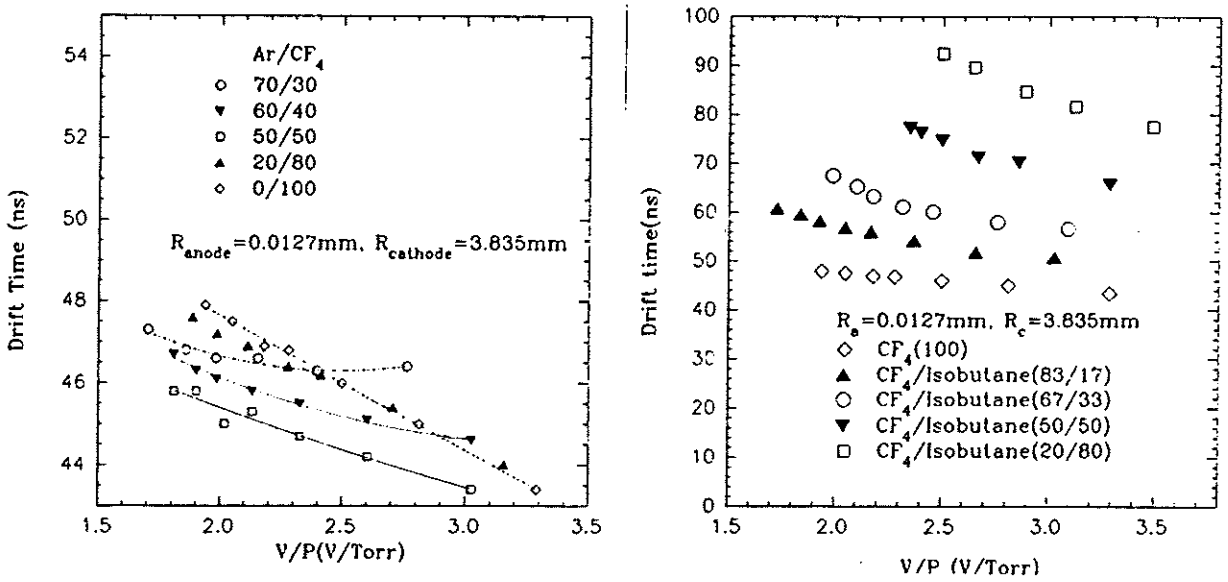

Figure 36: Total drift time of CF_4/Ar and CF_4/isobutane.

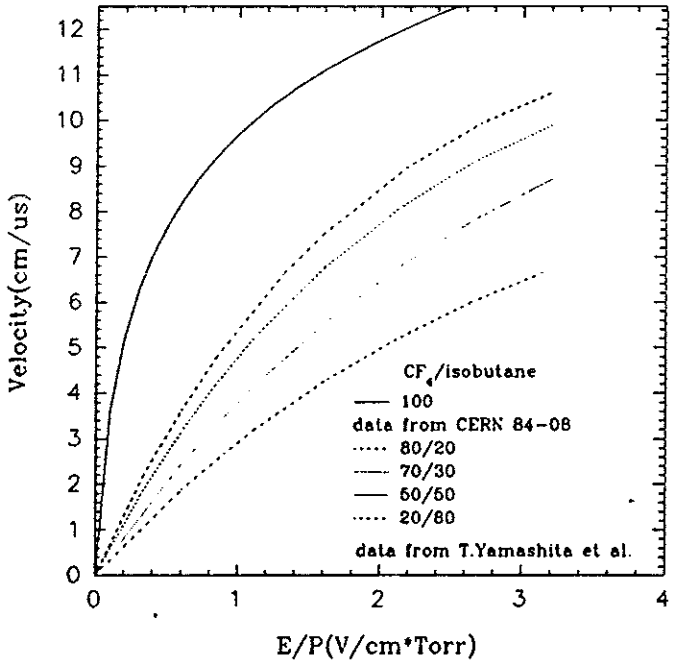

Figure 37: Compilation of drift velocity in CF_4/isobutane.

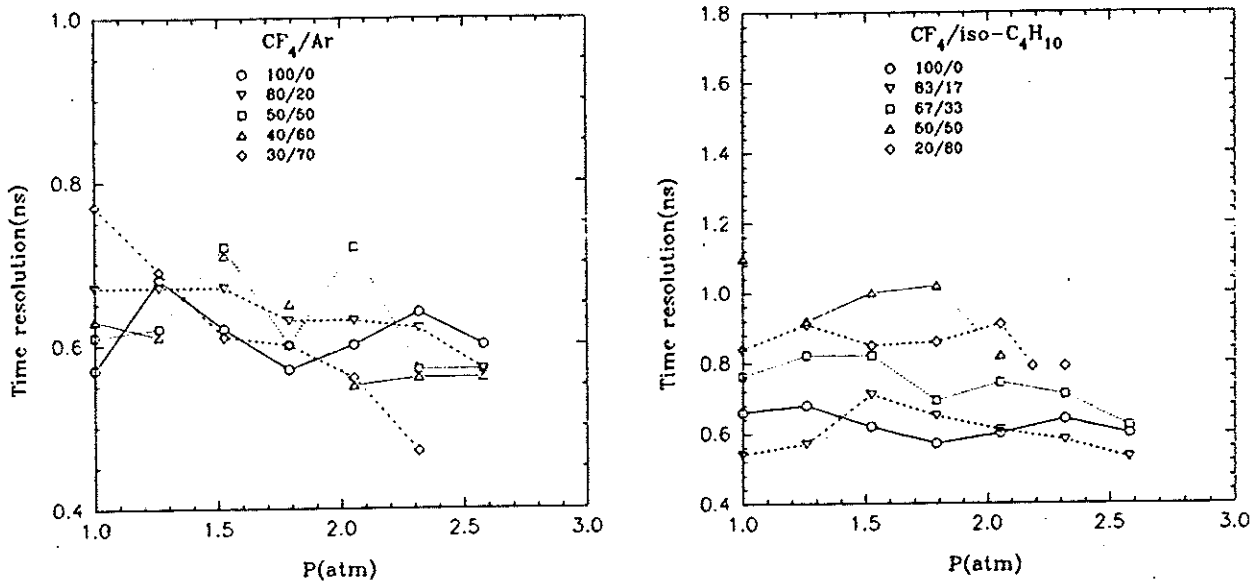

Figure 38: Time resolution of CF_4/Ar and CF_4/isobutane.

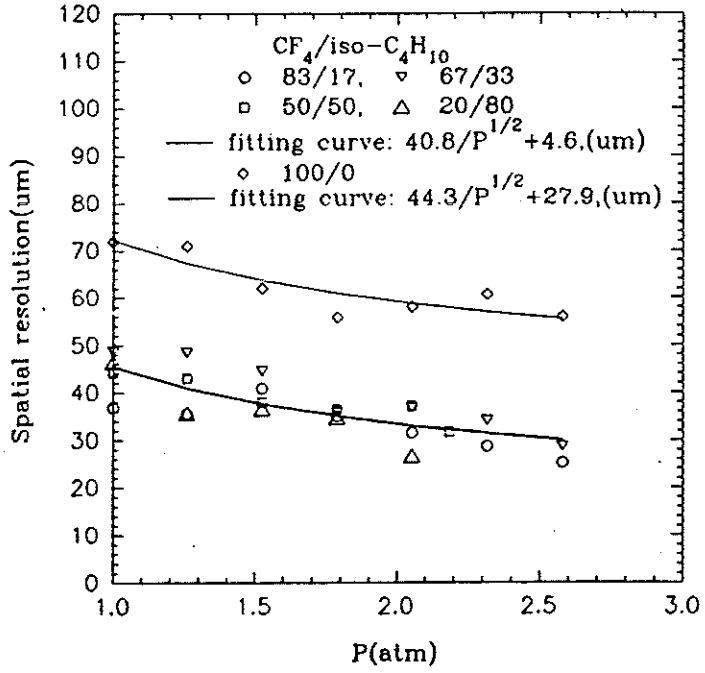

Figure 39: Spatial resolution of CF_4/isobutane.

28 Fluctuations in Single-Electron Avalanches

A detailed Monte Carlo study of timing strategies in drift chambers[33] has concluded that the simplest approach is still the best. The best accuracy obtainable is based on first-electron timing. Therefore fluctuations in the single-electron avalanche play an important role in timing measurements.

We have studied this with the same experimental set-up as in the timing measurements. Here we use an EG&G ORTEC 142PC charge-sensitive preamplifier instead of the transresistance preamplifier used for timing measurements. Figure 40 shows the electronic block diagram.

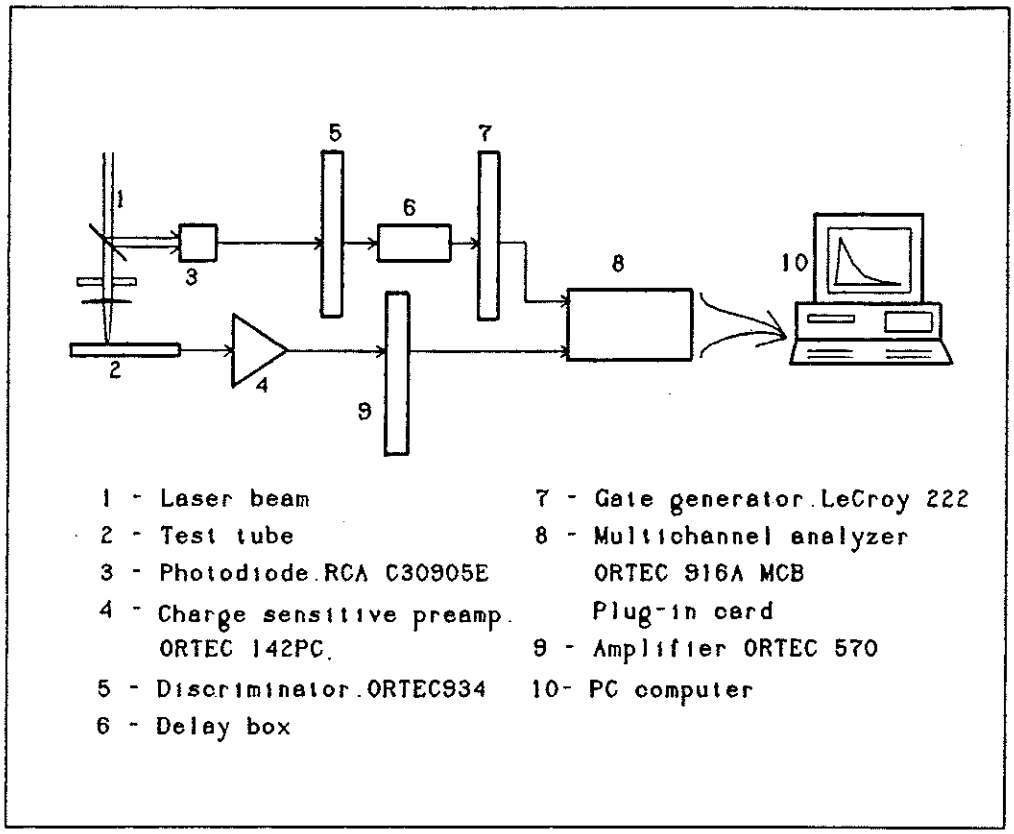

Figure 40: Electronics for single-electron-avalanche measurements.

For each gas mixture we first used the timing-measurement set-up to adjust the diaphragm until only one in 10-20 laser pulses yielded a photoelectron. Then the output of drift tube was plugged into an EG&G ORTEC charge-sensitive amplifier. A wide gate signal generated by the photodiode was used to define with drift tube's signal after amplification. With this there was no evidence for any background pulses, and no background subtrac-

tion has been made in the data analysis. The only limitation in mapping the complete single-electron spectrum was the signal threshold which was set to discriminate against the noise.

28.1 Review of the Single-Electron-Avalanche Distribution

In this section we review some of the arguments that led to the introduction of the Polya distribution to describe the charge spectra of single-electron avalanches.

The statistics of the single-electron avalanche in a gas chamber was first investigated by Snyder,[34] and then by Wijsman.[35] They showed that in the absence of electron attachment and molecular dissociation, the probability function of having n electrons in an avalanche will be the Furry distribution,

$$P(n) = \frac{1}{\bar{n}} e^{-n/\bar{n}},$$

where $\bar{n}$ is the mean avalanche size. In the case of a uniform electric field $\bar{n}$ is given by $\exp(\alpha d)$, where α is the first Townsend ionization coefficient, and d is the distance between cathode and anode plates. In deducing the Furry distribution, one assumes that each electron has the same probability of an ionizing collision in any interval dx, and that this probability is independent of the path travelled from the previous ionizing collision.

This distribution has been confirmed experimentally for low E/P. At high value of E/P, Schlumbohm found[36] that the distribution no longer satisfied by the Furry form, but exhibited a maximum at low value of n. This behavior was attributed to a failure of the condition required for establishing the Furry distribution, namely that $1/\alpha$, the average distance between ionizing collisions, is no longer very much greater than V_i/E, the minimum distance over which an electron can gain the ionization potential V_i. Schlumbohm showed[36, 37] that the value of the quantity $H = E/(\alpha V_i)$ determines the form of the distribution, not only for uniform fields but also for nonuniform fields such as considered by Curran *et al.*[38] Figure 229 shows E/α *vs.* E/P for methane.[39] E/α, and therefore H, decreases with increasing E/P.

The peaked distribution observed at high values of H is found to be in close agreement with the Polya distribution.[39] This distribution can be obtained in a manner similar to that for the Furry distribution by considering that the ionization coefficient α is a decreasing function of the particular avalanche size n (as well as of some measure such as position x of the average environment of the avalanche):

$$\alpha(n, x) = \alpha(x)[1 + (\theta/n)],$$

θ is an empirical constant. A detailed treatment shows that $P(n, x)$ is distributed according to Polya law, which for large value of $n(x)$, takes the form

$$P(n, x) \simeq a[bn/\bar{n}(x)]^{b-1} e^{-bn/\bar{n}(x)},$$

where $b = 1+\theta$. The exact physical significance of the parameter θ is not clear and objections have been raised[40] to one interpretation that has been proposed for it.[39]

The theoretical aspects mentioned above are concerned with multiplication based on ionization by electron impact only; secondary processes taking place at the cathode or elsewhere are ignored. When secondary processes become significant, avalanche breeding may take place and avalanche chains are detected in place of single avalanche.[41]

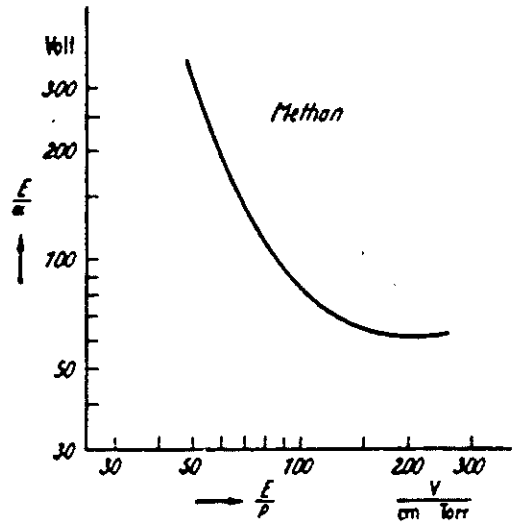

Figure 41: E/α *vs.* E/P for methane.

A theoretical analysis of avalanche-chain formation,[42] taking the distribution of individual avalanches and the distribution of the number of avalanches within the chain into account, led to the asymptotic form

$$P(z) \simeq Bz^{-3/2}e^{Cz}, \qquad z \equiv n/\bar{n}.$$

Byrne *et al.*[43] tested this theory at values of $z \gg 1$ with a P-10 proportional counter. The experimental distribution was in general agreement with the theoretical prediction when the asymptotic negative logarithmic derivative, $-(1/p(z))dp(z)/dz$, was plotted against $1/z$, but there was a spread in the observed asymptotic slopes about the predicted value of 3/2.

28.2 Experimental Results

The single-electron-avalanche spectra from Ar/CF_4 and Ar/isobutane have been measured for several different mixing ratios. The N−2 laser was used for this. The single-electron-avalanche spectra were then fitted with the Polya distribution

$$P(a) \propto (ba/\bar{a})^{b-1}e^{-ba/\bar{a}},$$

where a is the amplitude of an avalanche, $\bar{a}$ is proportional to the mean gas gain, and b is a measure of the fluctuation of gas gain: $(\sigma_a/a)^2 = 1/b$. Typical experimental distributions with their Polya fitting curves are shown in Fig. 42.

We are able to observe the presence of electron attachment in the chamber gas as follows. Charge spectra were also recorded for each gas mixture at several different high voltages using

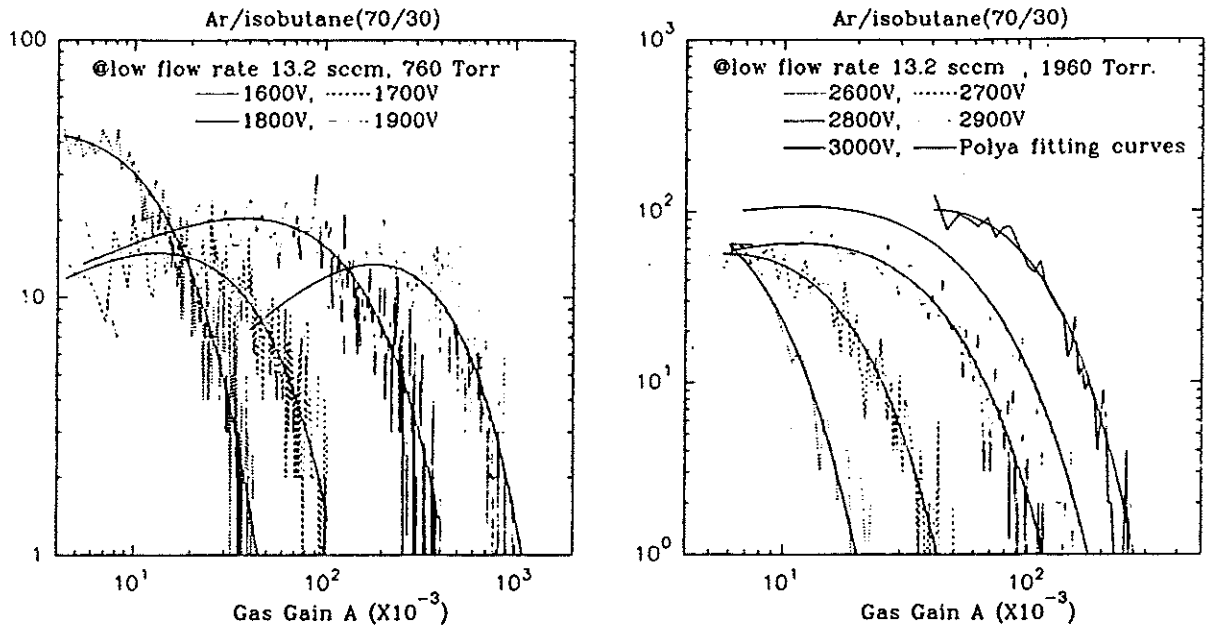

Figure 42: Single-electron-avalanche distributions with their Polya fittings for Ar/isobutane(70/30).

an Fe^{55} source. If the signal size observed with the Fe^{55} source is not ~ 200 times that from a single photoelectron ejected by a laser pulse, then attachment has occurred. Comparisons of avalanches due to single photoelectrons with those from Fe^{55} x-rays are shown in Figs. 43 and 44.

All three of the Ar/isobutane gas mixtures gave rather consistent results, both from single electrons as well as from Fe^{55} x-rays. This convinced us that the gas system had little contamination and the technique for single-electron-avalanche measurement was reliable.

Then when Ar/CF_4 gas mixtures were tested, the large discrepancy between single-electron and Fe^{55} measurements indicates that CF_4 may have serious electron attachment.[30] The gas gain from single electrons was about ten times higher than that from Fe^{55}.

Some processes of electron attachment to CF_4 are summarized in Table 5.[30] Electrons of $\gtrsim 5$ eV can disassociate CF_4 with fair probability. Thus it appears likely that attachment will occur in higher-field regions, such as near the anode wire. The amount of attachment may be reduced somewhat by operating the chamber at lower gas gain – but then sensitivity to single electrons may be lost.

Additional evidence for electron attachment is the poor energy resolution observed with Ar/CF_4 mixtures. Previous work[30] yielded energy resolutions with Ar/CF_4 (95/5) and (90/10) of $\sim 60\%$ and $\sim 75\%$, respectively. We have measured the energy resolution for the mixing ratios (80/20), (70/30), (60/40), and (50/50) under different gas pressures. Typical values are summarized in Table 6, and some spectra are shown in Fig. 45.

Apparently the energy resolution of Ar/CF_4 worsens with increasing gas pressure and

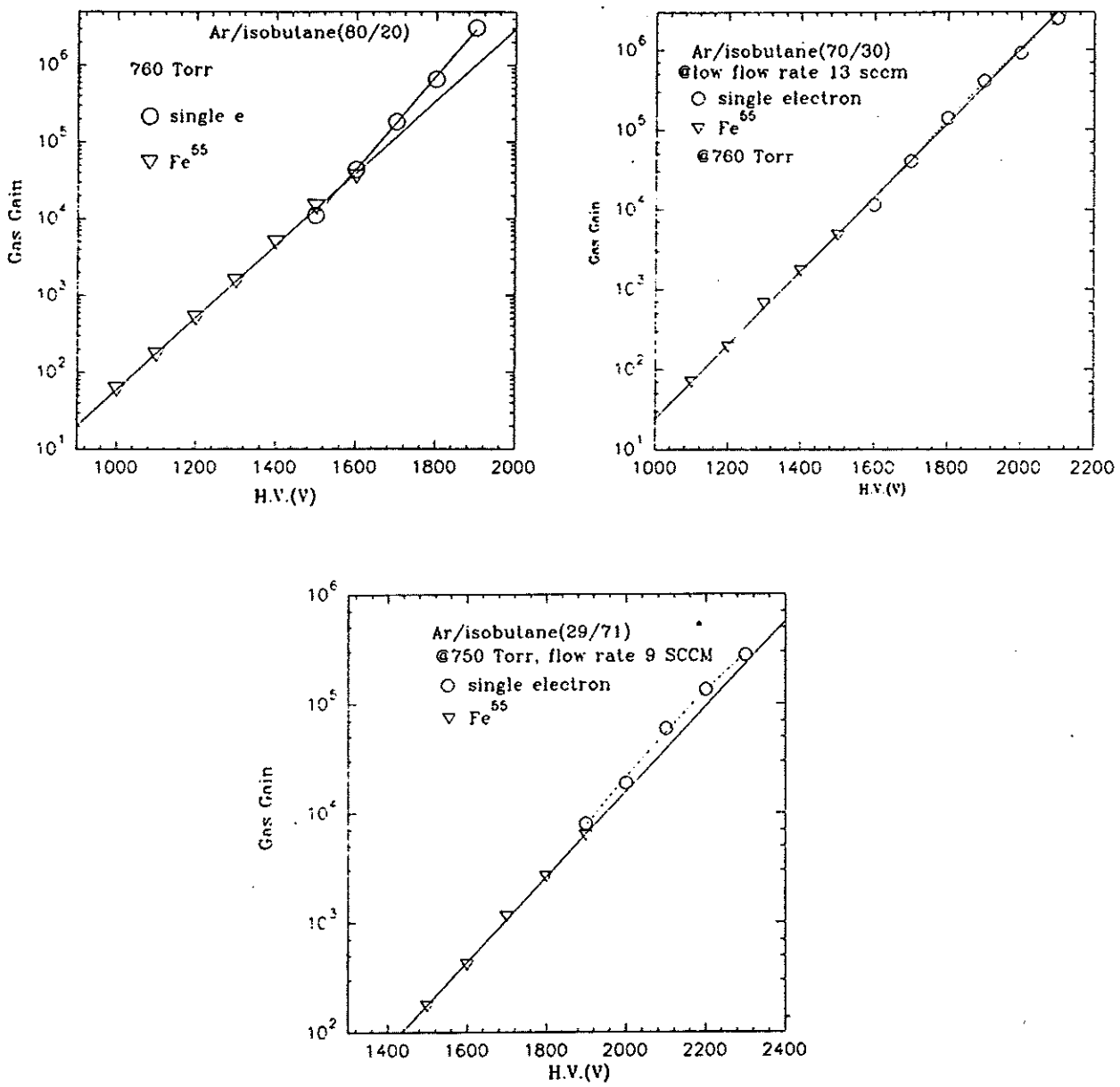

Figure 43: Gas gain from single photoelectrons and from Fe^{55} x-rays in Ar/isobutane.

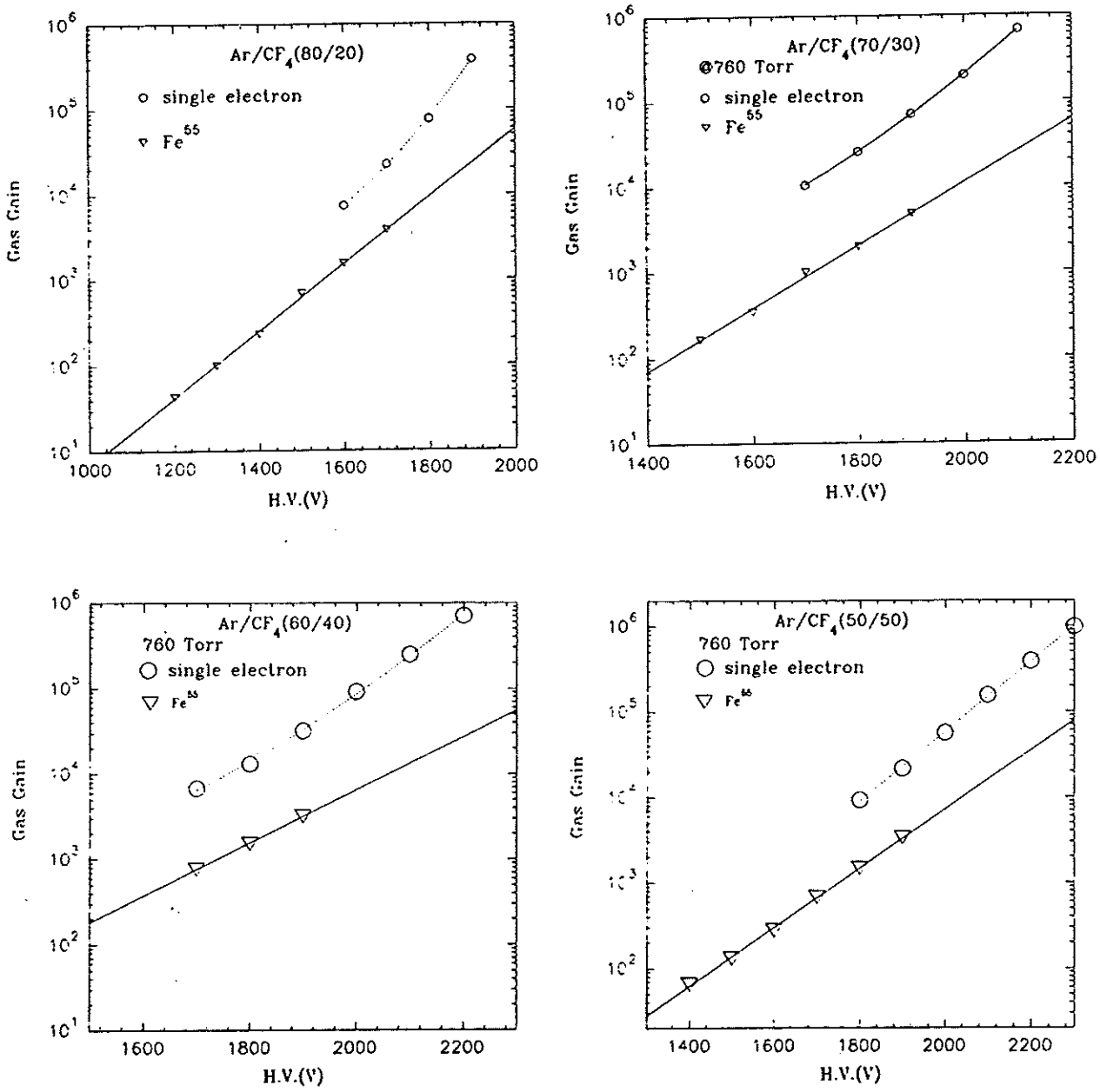

Figure 44: Gas gain from single photoelectrons and from Fe^{55} x-rays in Ar/CF_4.

Table 5: Negative ions formed by electron impact on CF_4.

Process $CF_4 + e \rightarrow$	Threshold (eV)	eV at σ_{max}	Reference
$F^- + CF_3$	4.65 ± 0.1	6.15 ± 1	24
	4.7 ± 0.1		25
	4.5 ± 0.3		26
$F^- + CF_3^*$ or $F^- + F + CF_2$	$6.2 \sim 6.5$	~ 7.5	24
$CF_3^- + F$	5.4 ± 0.1	6.9 ± 0.1	24
	5.4 ± 0.1		25
	4.9 ± 0.3		26

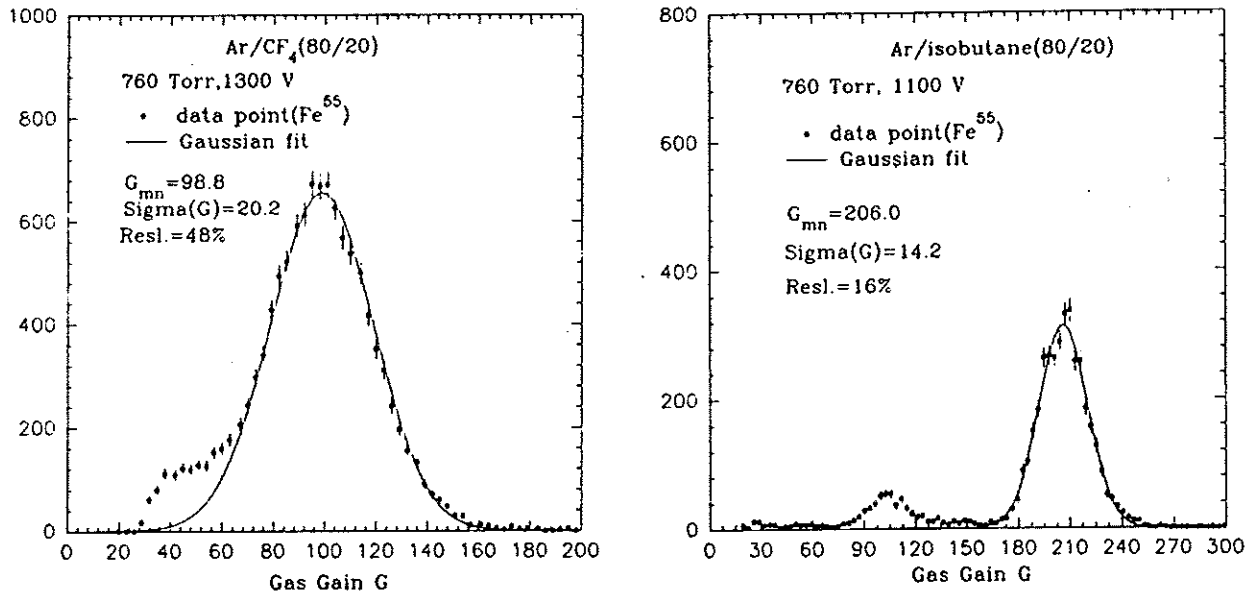

Figure 45: Charge spectra of Fe^{55} in Ar/CF_4 and Ar/isobutane.

with increasing percentage of CF_4. In contrast the dependence of energy resolution on gas pressure for Ar/isobutane is not quite clear.

28.3 Discussion of Energy Resolution

A statistical model of the energy resolution of proportional counters has been well established. There are two basic contributions to gas-gain fluctuations, variations in the number n_0 of

Table 6: Energy resolution of Ar/CF_4 and Ar/isobutane using an Fe^{55} source.

Ar/CF_4	P (Torr)	H.V.	Gas Gain	Resolution (Fe^{55})
80/20	760	1300	98.8	48%
	1160	1600	105.9	61%
	1960	2100	107.2	82%
50/50	760	1500	119.0	53%
	1160	1800	92.2	63%
	1960	2400	89.1	98%
Ar/isobutane				
80/20	760	1100	206.0	16%
	1160	1300	377.1	18.4%
	1960	1700	243.8	17.3%
70/30	760	1200	210.5	16.4%
29/71	760	1800	994.9	16.7%
90/10	760	900	188.5	13.3%
	1160	1200	2564.0	12.5%
	1960	1500	1861.0	15.2%

electron-ion pairs, and variation in size a of a single-electron avalanche. This can be expressed as the follows:[47]

$$\left(\frac{\sigma_A}{A}\right)^2 = \left(\frac{\sigma_{n_0}}{n_0}\right)^2 + \frac{1}{n_0}\left(\frac{\sigma_a}{a}\right)^2,$$

$$\left(\frac{\sigma_{n_0}}{n_0}\right)^2 = \frac{F}{n_0},$$

$$\left(\frac{\sigma_a}{a}\right)^2 = \frac{1}{b},$$

where F is the Fano factor and b is the parameter of Polya distribution. Finally we obtain

$$\left(\frac{\sigma_A}{A}\right)^2 = \frac{1}{n_0}\left(F + \frac{1}{b}\right). \tag{26}$$

Typical values of F and b are 0.05-0.2 and 1-2, respectively. Since n_0 is the number of ion pairs created by the incident radiation,

$$n_0 = E/W,$$

where E is the deposited energy, and W is the average energy loss per ion pair created. For Fe^{55}, $E = 5.9$ keV, and $W \sim 25$-35 eV. For all of the gas mixtures we have tested, $n_0 \sim 200$. The Polya parameters b for these gas mixtures are summarized in Fig. 46. All of them are greater than 1.

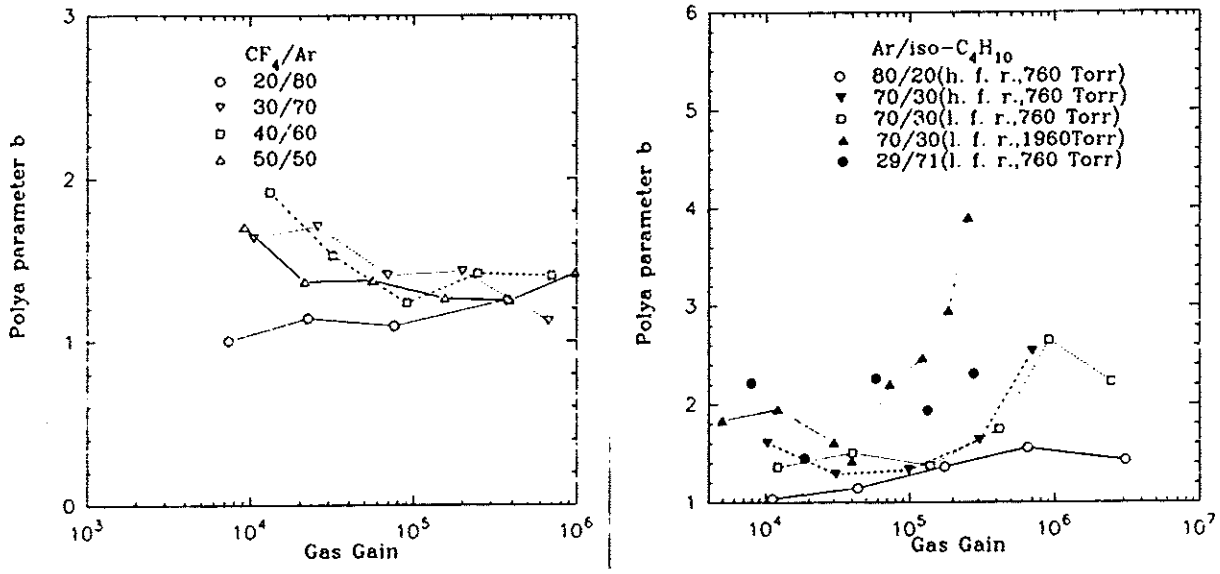

Figure 46: Polya parameters.

A rather surprising fact is that even under the worst case of F and b (but no electron attachment), the energy resolution of 5.9-keV x-rays still should be better than 18%. For Ar/CF_4 the measured energy resolution is worse than this by a factor of 3-5. If n_0 has been reduced by a factor of 9-25 due to electron attachment this behavior would be explained. As noted previously, such a reduction is consistent with the low mean value of the gas gain observed for Ar/CF_4 mixtures with an Fe^{55} source (see Fig. 44).

28.4 Conclusions

- Single-electron avalanches in a proportional counter have been successfully studied with a pulsed N_2 laser set-up. The drift time measurement for three well-understood gas mixtures are in good agreement with published data.
- The drift velocity in CF_4/isobutane is sensitive to the percentage of isobutane. The best time resolution in a 7.67-mm-thick proportional drift tube was $\sim$ 0.6 ns.
- In contrast, the total drift time in CF_4/Ar is not sensitive to the mixing ratio, and is very fast. For five different mixing ratios tested the total drift time varied between 40 to 50 ns, all with time resolution $\sim$ 0.6 ns. This corresponds to a spatial resolution of $\sim$ 50 μm for a 3.83-mm drift.

- The Polya distribution fits the gain spectrum of single-electron avalanches rather well. The Polya parameter b, which indicates the width of the fluctuation, has been determined for various mixing ratios of Ar/CF_4 and Ar/isobutane.
- Comparison of the gas gains obtained from single electrons as well as from Fe^{55} x-rays has revealed the likelihood of serious electron attachment in Ar/CF_4 gas mixtures, which is certainly due to the CF_4.
- Due to the electron attachment, CF_4 mixtures must be operated with higher voltages to compensate for loss of gas gain. The attachment also leads to large gain fluctuations, so these mixtures yield poor resolution of the deposited energy.

29 Gas Analysis

We have seen that one of the most interesting gases for straw-tube systems, CF_4, is apparently subject to electron attachment. But this effect could also be due to contamination in our gas system. As we strive for higher performance of the straw tubes we must be able to maintain a high standard of purity or our gases, and stability of the gas mixtures. An important tool for this is online analysis of the gas composition, both for trace impurities, and for the major componets.

The device of greatest utility in gas analysis that is available at reasonable cost is a gas chromatograph. To gain experience we have borrowed a Gow-Mac 550 Gas Chromatograph (that was built in 1979) from Fermilab. This has a thermal conductivity detector and two columns: one is packed with Molecular Sieve 5A (column "A") and is suitable for separating the "natural gases" like nitrogen, oxygen, carbon dioxide; the other is packed with Chromosorb 102 (column "B") and is suitable for separating the light hydrocarbons. Examples of the output of these columns are shown in Fig. 47a, where the Molecular Sieve 5A is used to separate a sample of air into components of Nitrogen and Oxygen, and in Fig. 47b where the Chromosorb is used to separate a 50/50 mixture of Argon/Ethane.

The device is nonlinear and to obtain a quantitative analysis a careful calibration must first be carried out with several different concentrations of sample gas. This has not yet been done because at the moment the only output available from the GC is in chartrecorder format as shown in the Fig. 47. Performing the required integration under the peaks is a tedious process. This task is made easier by computerized data-acquisition devices that have become available for PC-clone computers.

When calibrated this device should be capable of analysing mixtures to an accuracy of 1% or better. This is acceptable for a knowledge of the major constituents of the gas mixture but is not good enough for an analysis of the trace pollutants.

It is clear that we must invest in a high-quality chromatograph to attain the accuracy and ease of use that can favorably impact our knowledge and control of our gas system. We propose to make this investment in the next year. It appears that it may be best to purchase specialized monitors for oxygen and water vapor, as well as a research-grade gas chromatograph, since the latter has difficulty is separating oxygen from argon unless rather expensive detector options are used.

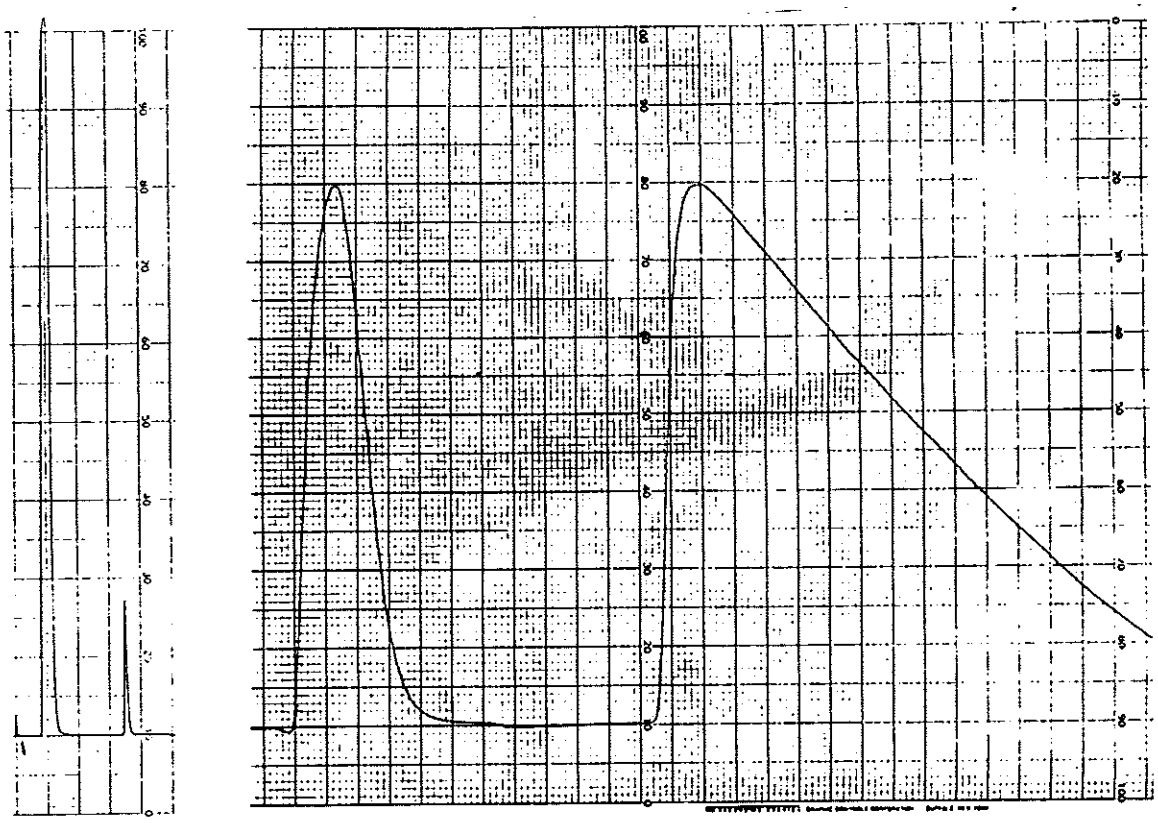

Figure 47: (a) Separation of a sample of air into two peaks for nitrogen and oxygen using column "A" of the Gow-MAC gas chromatograph. (b) Separation of a 50/50 mixture of Argon/Ethane using column "B". *N.b.*, the vertical scale changes between the two peaks.

30 Model of Straw-Tube Detector Performance

[The work in this section was performed by M.C. Lundin of Fermilab in association with the Princeton straw-tube effort, but not funded by the SSC.]

We have parameterized the physics of the straw tubes and their timing electronics via a simple Monte Carlo model,[48] based on a similar model for drift chambers from SLAC.[50]

The model is as follows:

1. Along the track path within the gas, distributed via a Poisson distribution, are n ionization events/cm, n being different for each gas chosen. (The mean value of n is 25.5 for 1 atmosphere argon-ethane, for example.)

2. The electrons drift radially (excluding Lorentz angle effects) toward the wire in an electric field sufficiently high to saturate the drift velocity. They also diffuse radially according to a gaussian with a σ that is a constant times the square root of the initial radial distance from the wire. This diffusion constant is not in general accurately known for all gases.

3. At the wire, each electron is independently amplified by a factor A_i which is distributed according to the Polya distribution

$$P(x) = (3x/2)e^{-3x/2} \qquad \text{where} \qquad x = A_i/\langle A \rangle.$$

4. The tube acts as a transmission line driven by a current source giving a voltage pulse which is, to within a constant:

$$V(T) = A_i/(T_0 + T) \qquad \text{where} \qquad T_0 = 1 \text{ nsec.}$$

5. The amplified signal is characterized by a rise time T_r. This is approximated by assuming the amplifier response to a step-function input is a ramp of duration T_r followed by a plateau.

6. The final signal that is fed to a discriminator is just the sum of the individual pulses delayed relative to each other by the electron arrival times at the anode. The dispersion in discriminator firing times (and thus the spatial resolution) can then be studied as a function of initial impact parameter, radial diffusion for a given gas, amplifier rise time and discriminator threshold.

Figure 48 compares the model calculation with the experimental results shown previously in Fig. 32. The agreement is encouraging. The model can then be used to predict the spatial resolution for minimum-ionizing tracks as a function of their impact parameter with the straw-tube anode wire, as shown in Fig. 49. If a fast-rise-time preamplifier is used, the lowest curve should be attainable in practice.

31 Simulation of Momentum Resolution in a Straw-Tube System

In this and the follwoing section we consider the possible performance of a straw-tube system in an SSC experiment such as the Bottom Collider Detector. This has a dipole magnetic field of 1 Tesla oriented transverse to the bemas. The Central tracking system occupies a volume 180×180 cm^2 in cross section and 6 m along the beams, as shown in Fig. 50. This volume includes the silicon vertex detector also, which occupies a cylinder of 10-cm radius about the beams. The Central tracking system is long enough to perform tracking for the Intermediate detector, which has no separate tracking system. In the Forward detector an additional tracking system is needed, which consists of three stations of tracking chambers surrounding the Forward analysis magnet.

A possible layout for the Central tracking system is shown in Fig. 51. The chambers close the interaction point are on circular arcs, which avoids the edge effects if the circles are complete. A drawback is that the tilted tubes lie on hyperboloids of revolution, which cannot be made out of cylindrical tubes without cracks between adjacent tubes (or tube-modules) that grow larger away from the midplane. In the more forward part of the Central detector the available volume flares outwards. Here the tilted planes can extend into the flare, permitting full coverage of the 180×180 cm^2 cross section of the tracking volume. An

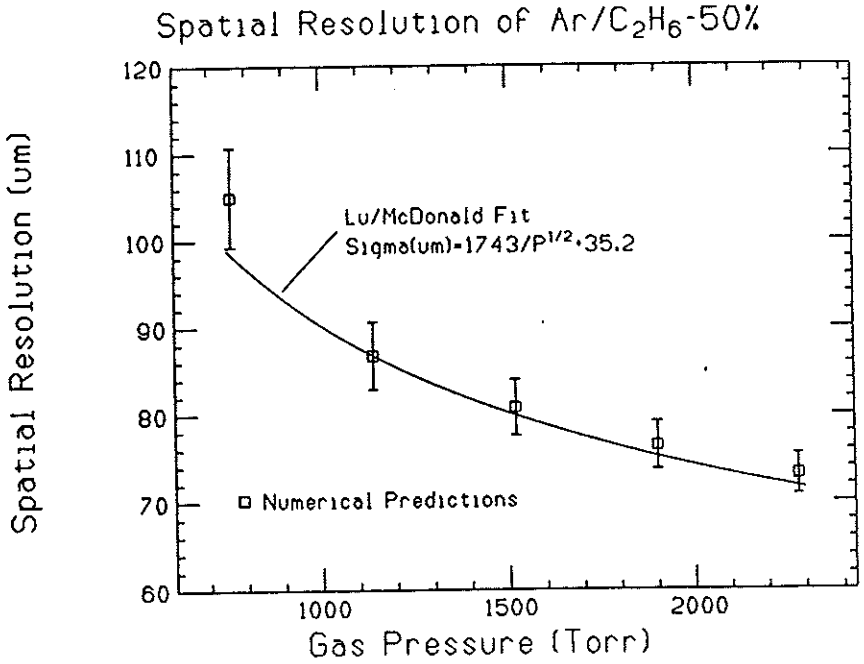

Figure 48: Numerical simulation of the spatial resolution reported in Fig. 32.

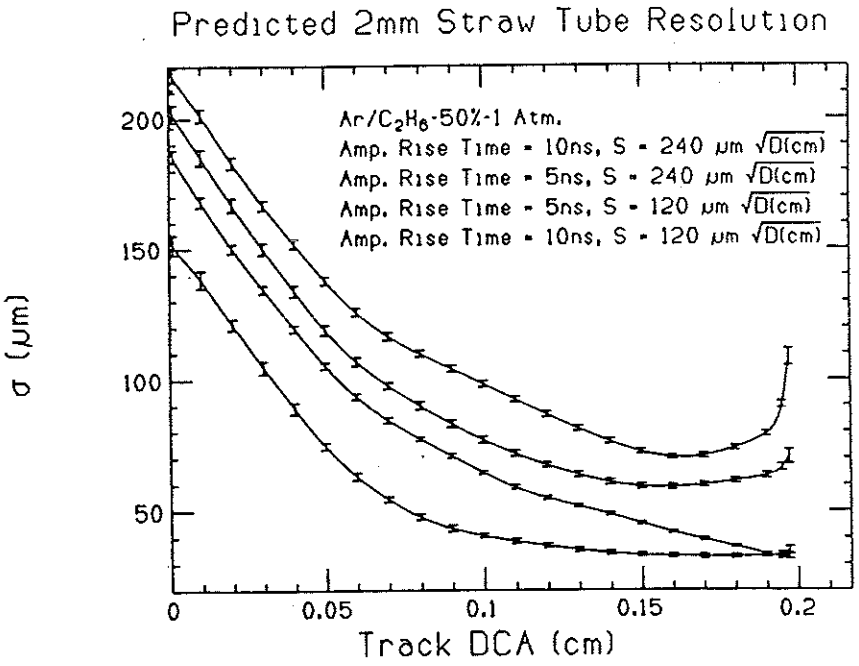

Figure 49: Numerical simulation of the spatial resolution of a straw-tube chamber as a function of the distance of closest approach (DCA) of a minimum-ionizing track to the anode wire.

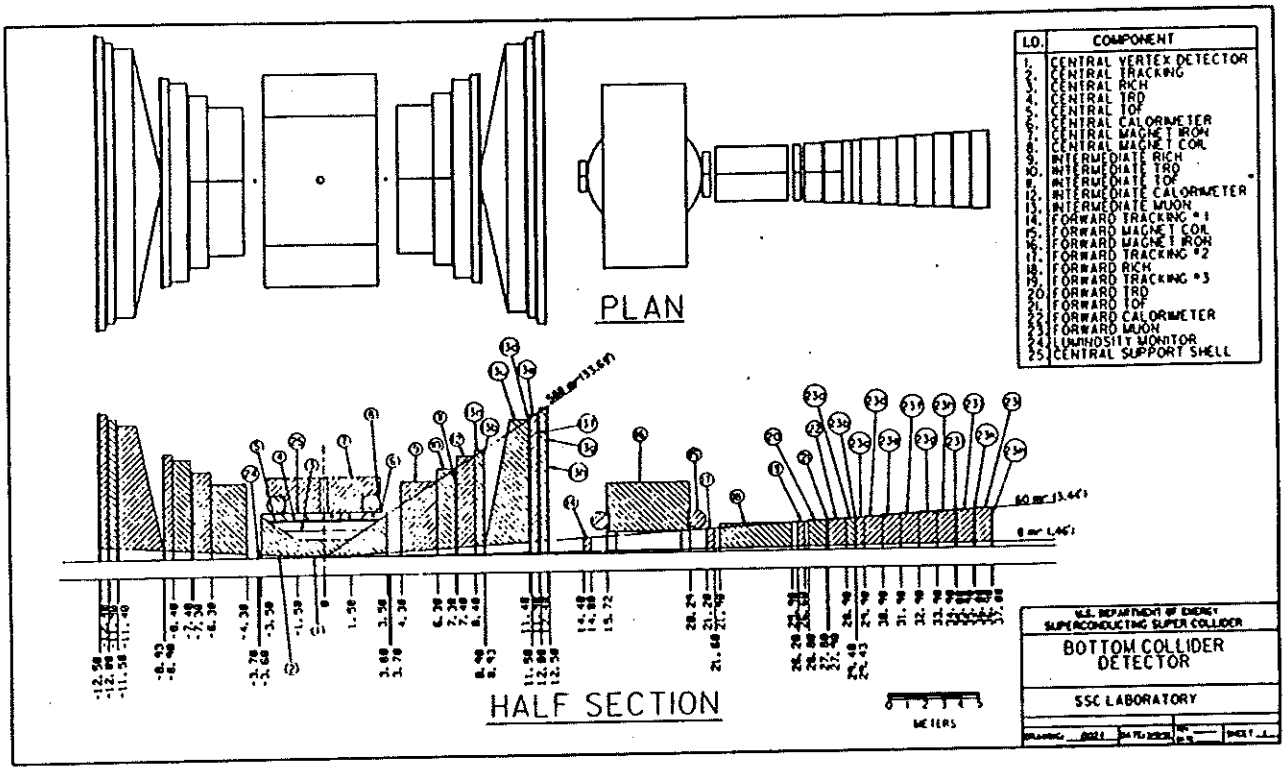

Figure 50: Plan and section views of the Bottom Collider Detector.Central Detector: **1**: silicon vertex detector, **2**: straw-tube tracking system, **3**: RICH counter, **4**: transition radiation detector, **5**: time-of-flight system, **6**: electromagnetic calorimeter, **7**: magnet yoke, **8**: superconducting coil. Intermediate Detector: **9**: RICH counter, **10**: TRD, **11**: time-of-flight, **12** E-M calorimeter, **13**: Muon system. Forward Detector: **14, 17, 19**: tracking, **15**: superconducting coil, **16**: magnet yoke, **18**: RICH counter, **20**: TRD, **21**: time-of-flight, **22**: E-M calorimeter, **23** muon system, **24**: luminosity monitor, **25**: central support shell.

alternative scheme based entirely on rectangular arrangements of the straw-tubes is shown in Fig. 53.

The 'superlayers' of detector elements shown in Fig. 51 will be built out of modules 8 straws thick and 8-64 straws wide.

We estimate the momentum resolution that will be obtained in the tracking system with the following expression;[49]

$$\left(\frac{\sigma_{P_\perp}}{P_\perp}\right)^2 = \frac{720}{n+5}\left(\frac{\sigma_{x_\perp} P_\perp}{3\times 10^{-4} BL^2}\right)^2 + 1.43\left(\frac{0.015}{3\times 10^{-4}\beta BL}\right)^2 \sum_{i=1}^{n} t_i(1+(1/9)\log_{10} t_i),$$

where $P_\perp$ is the momentum component perpendicular to the magnetic field (not the beam), $\sigma_{x_\perp}$ is the measurement error in cm, B is the magnetic field strength in kG, L is the path length in cm over which the measurement is made, n is the number of measurements, and t_i is the thickness in radiation lengths of the material associated with measurement i. This

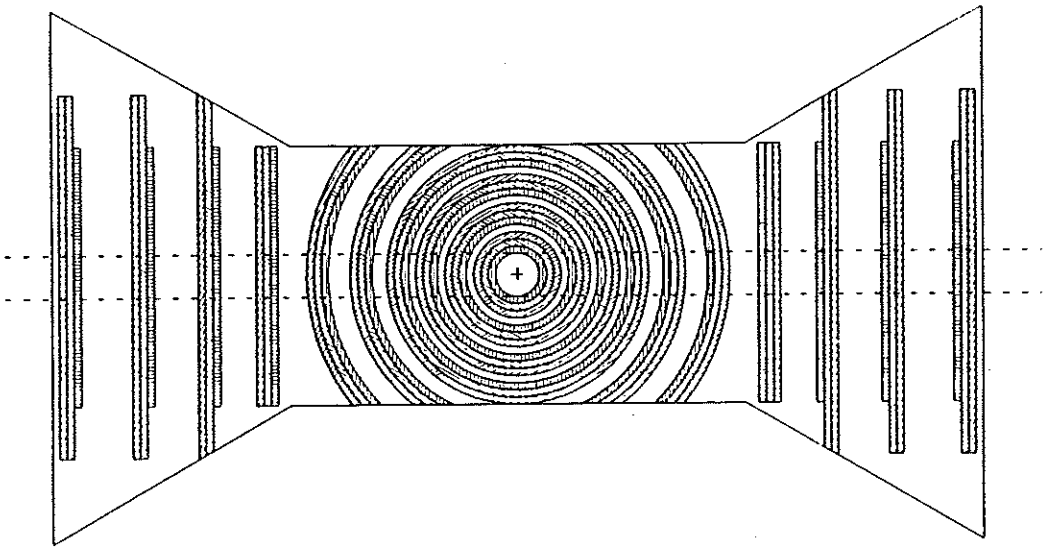

Figure 51: A possible layout of the Central straw-tube tracker, shown in plan view. The available volume is 6-m long and 180 × 180 cm^2 in cross section, with flares at 33° to the beams. The cylindrical arrangement of the chambers in the center avoids edge effects in the small-angle stereo layers. In the forward region the tilted planes will extend into the flare to maintain full coverage over the 180-cm width. The silicon vertex detector occupies a cylinder of radius 15 cm about the beams inside the tracking volume.

expression is strictly valid for the case of uniform sampling along L, which is entirely within field B. The dependence of the momentum resolution on spatial resolution and momentum has the familiar form

$$\left(\frac{\sigma_{P_\perp}}{P_\perp}\right)^2 = (A\sigma_{x_\perp}P_\perp)^2 + B^2.$$

We have modelled the detector performance supposing $n = 64$ in the Central tracker, and $n = 96$ in the Forward tracker. Field B is 10 kG in the Central tracker over its 6-m length, while we use an effective field of 4.6 kG in the Forward tracker where the field occupies only part of its 13-m length. Each straw contributes $t_i = 0.0004$ radiation length. Fig. 52 shows the expected resolution for particles with transverse momentum (to the beams) of 2.5 GeV/c and momentum vector perpendicular to the magnetic field. The spatial resolution in a single straw was taken to be $\sigma_{x_\perp} = 50$ μm.

Also shown is the momentum resolution obtained in the silicon vertex detector alone, for particles with $2.75 < \eta < 4.25$. In this interval the momentum measurement in the silicon detector is superior to that from the straw tracking system. The silicon detector is taken to have $\sigma_{x_\perp} = 5$ μm, and to extend 6 m along the beams (*i.e.*, the full length of the Central tracker).

We see that at P_t and with $\sigma_{x_\perp} = 50$ μm for the straws, the resolution is dominated by multiple scattering in all parts of the detector. However, if the spatial resolution deteriorates

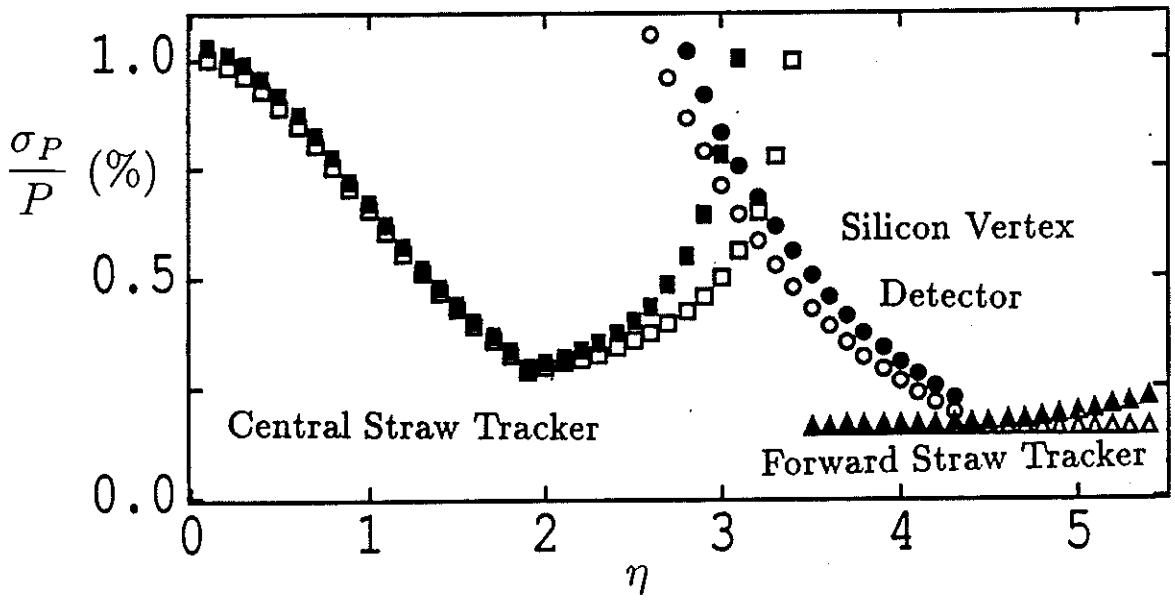

Figure 52: The momentum resolution *vs.* pseudorapidity η of the tracking system for particles with transverse momentum (to the beams) of 2.5 GeV/c and momentum vector perpendicular to the magnetic field. The spatial resolution of the straw-tube chambers is taken to be 50 μm, and that of the silicon vertex detector is 5 μm. The contribution of multiple scattering to the resolution is also shown, and is seen to be dominant for the given conditions.

to 100 μm, or if we consider $P_\perp = 5$ GeV/c, the measurement error adds about 25% to $\sigma_{P_\perp}/P_\perp$. The momentum resolution is better than 1% at all transverse momentum less than 2.5 GeV/c, which will yield $\sim 0.5\%$ mass resolution in the reconstruction of B decays.

32 Simulation of Pattern Recognition in a Straw-Tube System

[This work was performed by L. Stutte of Fermilab in association with the Princeton straw-tube effort, but was not funded by the SSC.]

32.1 Scope

The appropriate momentum scale for detecting B events, produced primarily through gluon-gluon fusion, is quite low—on the order of the B mass. The subsequent decay of the B's will result in tracks with average P_t of approximately 1 GeV/c. Thus, the tracking has to be quite good, even to very low P_t. Studies have shown that significant loss of events occurs if the lower momentum cutoff for reconstructing B decay products is much above 300 MeV/c. This is certainly a challenge in a collider environment. In addition, the dipole field and spatially distributed vertices (in the beam direction) make this a more difficult problem

than that commonly encountered in collider detectors using a solenoidal field, in which the tracks in the azimuthal view are circles coming from a single, well-defined beam-interaction point. Because of these challenges, the BCD has chosen to carry out its simulation to a level much more detailed than previous experiments at the proposal stage. Good tracking plays an integral part in one's ability to verticize B-decay candidates. So far, for these studies, the initial fit roads have been taken from the given generated momentum, smeared by the expected resolution of the straw tracking system. Straw pattern recognition and tracking will soon be combined with pattern recognition in the silicon to get a more realistic estimate of B-vertexing efficiency, in that actual found tracks will be used as the starting point.

32.2 Overview of the Straw-Tube-Simulation Strategy

The straw tracking planes are formed as superlayers of 8 individual planes of straws, all straws in a given superlayer having the same spatial orientation (x, y, u, or v). Superlayers of each type can then be grouped together to aid in pattern recognition. Figure 53 shows the current geometry modelled for the straw tracking system, as viewed in the direction of the magnetic field. The beams enter from left and right. All planes in the beam direction have an u-x-v-y multiplet. Some of the transverse planes have only an x-superlayer. Further optimization of this geometry is one of the goals of the straw simulation study.

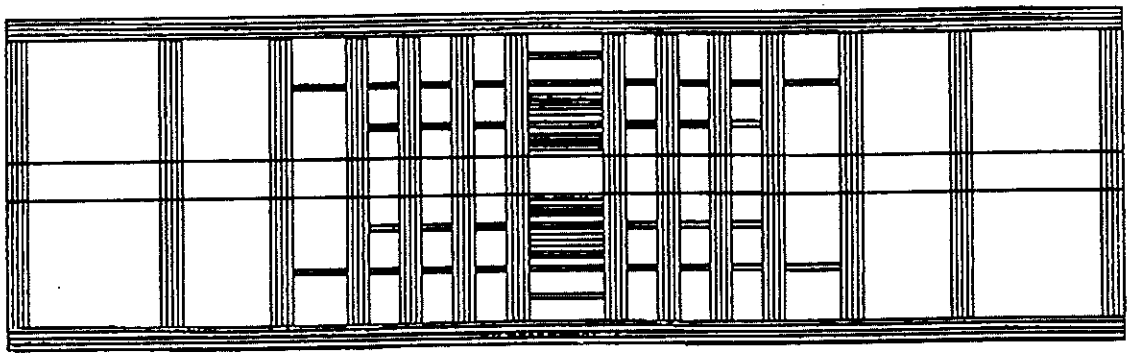

Figure 53: A view of the straw tracking system used in the computer simulation, looking along the direction of the magnetic field. This configuration is an alternative to that shown in Fig. 51.

Because of the complexity and time required to track through individual straw cells, we have chosen to separate the problem into two parts, as described in more detail below. Briefly, part one is a detailed, cell-level simulation that is intended to measure the pattern-recognition capability within a superlayer, combining hit straws (cells) into track segments called 'minivectors'. Part two is a full detector simulation which links these minivectors together, smeared by the appropriate resolution found in part one, to form tracks. We report here on part two only.

32.3 Full Detector Simulation

The goal for this part of the simulation is to find all minivectors associated with a given track, determine the track's momentum and finally to use these determined track parameters in the vertex-determining algorithms. Pairs of hits, representing found minivectors, are recorded at the entrance and exit of each superlayer, smeared by an assumed spatial resolution of 50 μm. At this stage of the study, no confusion from incorrectly identified minivectors is assumed. Minivectors in the outer layer of straw planes are then combined with an assumed primary-vertex position to give a starting search road. The primary-vertex position used is the true position smeared by 0.1 cm in the beam direction, a resolution that can be achieved from a simple fit to the silicon-plane data.

For simplicity, an almost completely hermetic outer layer of straw planes has been assumed. Forward and backward planes have a square beam hole of 10.6-cm half-size. Top, bottom and side chambers cover the full extent of the detector. Since less than 10% of the tracks exit via top or bottom planes, in reality these planes will probably not be built, but are included here for simplicity. In actuality, one would proceed to find tracks associated with the most outer layer of straw planes, eliminate minivectors from these tracks on more inner planes, and iterate inward toward the center of the detector. Again, for simplicity, a constant magnetic field has been assumed.

To start a fit, all pairs of u-v minivectors in an outer-layer plane are searched for a match to a minivector in an x-layer plane. These triplets are matched to a y-layer minivector. Losses at this stage of pattern recognition are small. For those tracks which are within the rapidity coverage of the straw tracking system, approximately 12% have momenta too low to arrive at an outer layer; typically these tracks have momenta well below 300 MeV/c, and are not of interest. For those tracks that do reach the outer straw layers, 95% are found and correctly matched. For the outer straw layers, the u-v planes have been configured as small-angle (15°) stereo planes with tubes running approximately perpendicular to the magnetic-field direction. This gives a match to the y coordinate (the magnetic-field direction) that is largely momentum independent, important in the outer planes that are used to determine the initial search road. For the inner straw layers, the small-angle u-v stereo planes have been configured with tubes running approximately parallel to the magnetic field direction, for increased resolution.

A simple unweighted circle fitter is then used to predict an initial bend-plane momentum. The nonbend-plane momentum is calculated from the dip angle. For the assumed minivector spatial resolution (50 μm) and primary-vertex z-position resolution (0.1 cm), the error on momentum for this initial fit is approximately 7%. Inner-layer planes are then searched with momentum-dependent roads for minivectors associated with each track. For planes in which more than one minivector is found within the search road, the mini- vector closest to the fit is retained. If a set of x-u-v-y minivectors have been found, all minivectors must be within the roads for any of them to be accepted. After all planes have been searched, if additional minivectors have been found, the momentum fits are updated using the x-plane minivectors only, and the search procedure is iterated. The momentum error for these updated fits has been reduced to 4% for momenta greater than 300 MeV/c. An improved fitting routine that uses minivectors from all plane types is now being written which will substantially improve this error.

Figures 54-55 show a typical event in the straw tracking system. This event was generated by ISAJET, using the $b\bar{b}$ two-jet process. Crosses on the figures represent the entrance and exit hits at the straw planes. Figure 54 displays all of the minivectors in the event, while Fig. 55 shows the found minivectors. For all tracks above 300 MeV/c that have outer-layer matches, 87% of the minivectors are found. For those tracks originating from the primary vertex, 91% of the minivectors are found. About 3% of the minivectors found for all tracks are unassociated with the track. At this stage in the simulation, these numbers are encouraging.

Figure 54: A typical SSC event from the $b\bar{b}$ two-jet process, showing all minivectors in the straw tracking system.

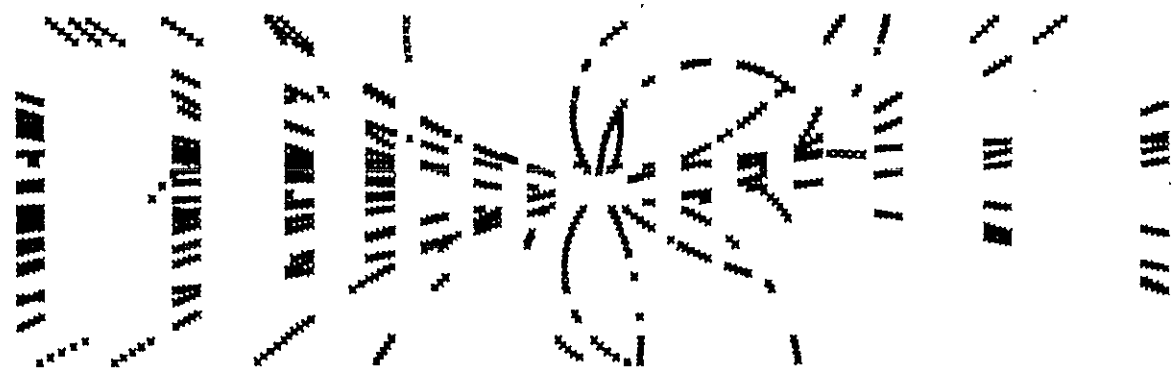

Figure 55: The same event, showing the found minivectors.

As the final step in our simulation we reconstructed the invariant mass of the B from tracks due to the decay $B_d^0 \rightarrow \pi^+\pi^-$. The mass resolution is about 30 MeV/c^2, as shown in Fig. 56, which indicates that the reconstruction program is working about as well as can be expected given the multiple scattering in the chambers.

32.4 Further Development

Several improvements are being implemented in the tracking pattern-recognition study:

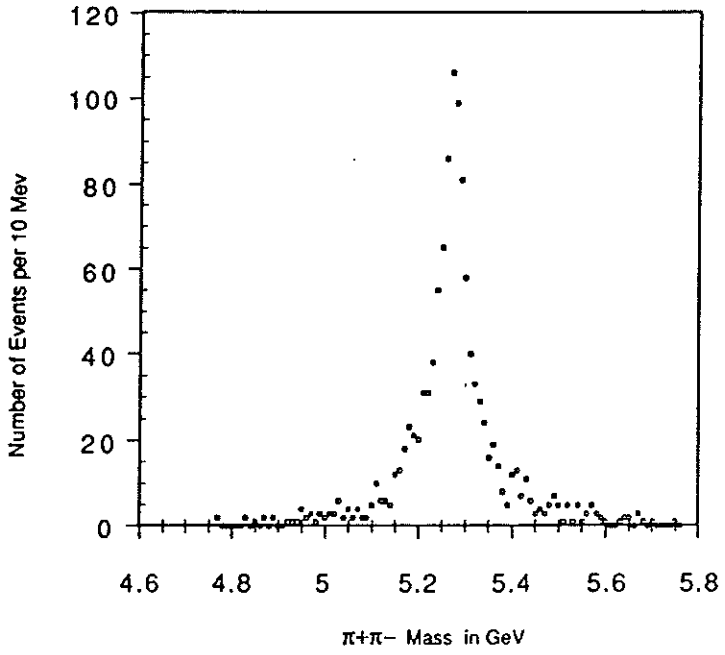

Figure 56: Simulated invariant-mass reconstruction of the decay $B^0 \to \pi^+\pi^-$. Multiple scattering and chamber resolution are simulated, and pattern-finding algorithms assemble the straw hits into tracks. The mass resolution achieved here is about 30 MeV/c^2.

1. Pattern recognition at the minivector level.
2. A more sophisticated fitting program.
3. Hit contention at the track level.
4. After the initial search, two fits can be attempted: one including the primary vertex, and one without it. The best fit of these two could then provide a new search road. This may improve hit finding on tracks which originate close to, but not at the primary vertex.
5. Found minivectors can be eliminated, and the remaining minivectors examined for tracks that do not originate close to the primary vertex.

33 References

[1] C. Lu *et al.*, *Prototype Study of the Straw Tube Proportional Chamber*, Princeton U. preprint DOE/ER/3072-56 (Feb. 15, 1990).

[2] C. Lu and K.T. McDonald, *A Straw-Tube Tracking System for the SSC*, to appear in the Proceedings of the IISSC (Miami, Mar. 14-16, 1990).

[3] C. Lu and K.T. McDonald, *Drift-Chamber Timing Studies with a N_2 Laser*, Princeton U. preprint DOE/ER/3072-60 (June 10, 1990).

[4] M. Frautschi *et al.*, *The AMY Inner Tracking Chamber*, Ohio State U. preprint (Oct. 1989), submitted to Nucl. Instr. and Meth.

[5] Y. Asano *et al.*, *Tension Measurement of 7.6 m Drift Tubes of the Venus Muon Detector*, Nucl. Instr. and Meth. **A254**, 35 (1987).

[6] T. Regan, *A Sensitive Instrument for Measuring Wire Tensions in Multiwire Proportional and Drift Chambers*, Nucl. Instr. and Meth. **219**, 100 (1984).

[7] M.E. Rose and S.A. Korff, *An Investigation of the Properties of Proportional Counters*, Phys. Rev. **59**, 850 (1941).

[8] W. Diethorn, US Atomic Energy Commission Report, NYO-6628 (1956).

[9] A. Williams and R.I. Sara, Int. J. Appl. Radia. Isotopes **13**, 229 (1962).

[10] A. Zastawny, *Gas Amplification in a Proportional Counter with Carbon Dioxide*, J. Sci. Instr. **43**, 179 (1966).

[11] M.W. Charles, *Gas Gain Measurements in Proportional Counters*, J. Phys. **E5**, 95 (1972).

[12] T. Aoyama, *Generalized Gas Gain Formula for Proportional Counters*, Nucl. Instr. and Meth. **A234**, 125 (1985).

[13] T.Z. Kowalski, *Generalized parametrization of the Gas Gain in Proportional Counters*, Nucl. Instr. and Meth. **A243**, 501 (1986).

[14] L.G. Christophorou, *Atomic and Molecular Radiation Physics*, (Wiley-Interscience, 1971).

[15] C. Lu *et al.*, *Proposal to the SSC Laboratory for Research and Development of a Straw-Tube Tracking Subsystem*, Princeton U., DOE/ER/3072-56 (Sept. 39, 1989).

[16] J. Carr and H. Kagan, *Wire Stability Studies for an SSC Central Drift Tracker*, Proceedings of the 1986 Summer Study on the Physics of the SSC (June 1986), p. 396.

[17] W. Smythe, *Static and Dynamic Electricity* (McGraw-Hill, 1950).

[18] D. Blockus *et al.*, *SSC Detector Subsystem Proposal, Central and Forward Tracking with Wire Chambers* (Oct. 1989), Fig. 2.9.

[19] W.W. Ash *et al.*, *Design, Construction, Prototype Tests and Performance of a Vertex Chamber for the MAC Detector*, Nucl. Instr. and Meth. **A261**, 399 (1987).

[20] S.K. Kim, private communication.

[21] J.L. Pack and A.V. Phelps, *Drift Velocities of Slow Electrons in Helium, Neon, Argon, Hydrogen and Nitrogen*, Phys. Rev. **121**, 798 (1961).

[22] G.S. Hurst and J.E. Parks, *Time-of-Flight Determinations of Electron Diffusion Coefficients and Electron Drift Velocities in Ethylene, Water Vapor, and in Hydrogen*, J. Chem. Phys. **45**, 282 (1966).

[23] J. Va'vra, *The Use of a Nitrogen Laser for Observation of Space Charge Effects in Drift Chambers and Development of High Precision Vertex Chambers*, Nucl. Instr. and Meth. **225**, 13 (1984).

[24] K.W.D. Ledingham *et al.*, *Laser Induced Ionization in Proportional Counters Seeded with Low Ionization Potential Vapours*, Nucl. Instr. and Meth. **225**, 319 (1984).

[25] UA1 Collaboration, *A Laser Calibration Scheme for the UA1 Central Detector at High Luminosity (ACOL)*, Nucl. Instr. and Meth. **A263**, 26 (1988).

[26] J. Bourotte and B. Sadoulet, *Ionization of Multiwire Proportional Chamber Gas by Double Photon Absorption*, Nucl. Instr. and Meth. **173**, 463 (1980).

[27] V. Palladino and B. Sadoulet, *Application of Classical Theory of Electrons in Gases to Drift Proportional Chambers*, Nucl. Instr. and Meth. **128**, 323 (1975).

[28] F. Pius, *Measurement of the Longitudinal Diffusion of a Single Electron in Gas Mixtures Used in Proportional Counters*, Nucl. Instr. and Meth. **205**, 425 (1983).

[29] B. Jean-Marie *et al.*, *Systematic Measurement of Electron Drift Velocity and Study of Some Properties of Four Gas Mixtures: A-CH_4, A-C_2H_4, A-C_2H_6, A-C_3H_8*, Nucl. Instr. and Meth. **159**, 213 (1979).

[30] L.G. Christophrou *et al.*, *Fast Gas Mixtures for Gas-Filled Particle Detectors*, Nucl. Instr. and Meth. **163**, 141 (1979).

[31] J. Fischer *et al.*, *Proportional Chambers for Very High Counting Rates Based on Gas Mixtures of CF_4 with Hydrocarbons*, Nucl. Instr. and Meth. A238, 249 (1985).

[32] T. Yamashita *et al.*, *Measurements of the Electron Drift Velocity and Positive Ion Mobility for the Gases Containing CF_4*, Preprint.

[33] J. Va'vra, *Search for the Best Timing Strategy in High Precision Drift Chambers*, Nucl. Instr. and Meth. **225**, 445 (1985).

[34] H.S. Snyder, Phys. Rev. **72**, 181 (1947).

[35] R.A. Wijsman, *Breakdown Probability of a Low Pressure Gas Discharge*, Phys. Rev. **75**, 833 (1949).

[36] H. Schlumbohm, *Zur Statistik der Elektronenlawinen im ebenen Feld. III*, Z. Phys. **151**, 563 (1958).

[37] H. Schlumbohm, *Zur Statistik der Electronenlawinen im Proportionalzählrohr. IV*, Z. Phys. **152**, 49 (1958).

[38] S.C. Curran *et al.*, Phil. Mag. **40**, 929 (1949).

[39] J. Byrne, *Statistics of the Electron Multiplication Process in Proportional Counters*, Proc. Roy. Soc. Edin. **66A**, 33 (1962).

[40] A.H. Cookson and T.J. Lewis, *Variations in the Townsend First Ionization Coefficient for Gases*, Brit. J. Appl. Phys. **17**, 1473 (1966).

[41] H. Genz, *Single Electron Detection in Proportional Gas Counters*, Nucl. Instr. and Meth. **112**, 83 (1973).

[42] J.H. Carver and P. Mitchell, Nucl. Instr. and Meth. **52**, 130 (1967).

[43] J. Byrne *et al.*, *Avalanche Chain Development in an Argon-Methane Proportional Counter*, Nucl. Instr. and Meth. **79**, 286 (1979).

[44] P.W. Harland and J.C.J. Thyrne, Int. J. Mass Spectr. Ion Phys. **9**, 253 (1972).

[45] K.A.G. Macneil and J.C.J. Thyrne, Int. J. Mass Spectr. Ion Phys. **3**, 455 (1970).

[46] R.M. Reese *et al.*, J. Res. Natl. Bur. Stand. **57**, 367 (1956).

[47] G.F. Knoll, *Radiation Detection and Measurement*, 2nd ed., (John Wiley & Sons, New York, 1989)

[48] M.C. Lundin, *Study of Drift Tube Resolution Using Numerical Simulations*, Fermilab-Pub-xxxx (Sept. 1991).

[49] R.L. Gluckstern, *Uncertainties in Track Momentum and Direction Due to Multiple Scattering and Measurement Errors*, Nucl. Instr. and Meth. **24**, 381 (1963).

[50] Proceedings of the SLC Workshop on Experimental Use of the SLAC Linear Collider, SLAC-247 (March, 1982), p. 158.